Reactions of trapped ions with state- and conformer-selected neutral molecules

Inauguraldissertation

zur
Erlangung der Würde eines Doktors der Philosophie
vorgelegt der
Philosophisch-Naturwissenschaftlichen Fakultät
der Universität Basel

von

Ardita Kilaj
aus Zürich

Basel, 2020

Genehmigt von der Philosophisch-Naturwissenschaftlichen Fakultät
auf Antrag von
Prof. Dr. Stefan Willitsch
Prof. Dr. Roland Wester

Basel, den 23. Juni 2020

Prof. Dr. Martin Spiess
Dekan

Abstract

Understanding gas-phase ion-molecule reactions is of profound importance to gain knowledge about chemical processes taking place in the atmosphere and in space. Moreover, gas-phase studies can help to elucidate the mechanisms of bond activation in catalysis. Due to their high selectivity, reactions involving different conformational isomers of organic molecules are particularly intriguing.

Recent progress in manipulating polar molecules using electrostatic fields has made it possible to select and spatially separate different conformers and rotational states of molecules in supersonic molecular beams. Combining this technology with a stationary reaction target of trapped and Coulomb-crystallized ions allowed the study of conformer-selected molecule-ion reaction dynamics and it was observed that reaction-rate constants can strongly depend on molecular conformation.

Here, this concept was first applied to the proton-transfer reaction of the spatially separated rotational ground states of *para*- and *ortho*-water with cold diazenylium ions. A 23(9)% higher reactivity for the *para* nuclear-spin isomer was observed and attributed to the smaller degree of rotational averaging of the ion-dipole long-range interaction compared to the *ortho*-species.

To investigate the role of molecular conformation in more complex organic ion-molecule reactions in the gas-phase, 1,3-dibromobutadiene (DBB) was identified as a promising model system. Its *gauche*- and *s-trans*-conformers were successfully separated in a molecular beam, verifying theoretical predictions. Subsequently, the reaction kinetics of conformer-selectd *gauche* and *s-trans* DBB with Coulomb crystals of laser-cooled Ca^+ ions in an ion trap were investigated. It was found that the reaction rate constant strongly depends on both the conformation of DBB as well as the electronic state of Ca^+. In the excited states of Ca^+ ($^2P_{1/2}$ and $^2D_{3/2}$), the rate constants are capture-limited and enhanced for the *gauche* conformer due to its permanent dipole moment. With Ca^+ in the ground state ($^2S_{1/2}$), the rate for *s-trans* DBB stays unchanged, while that for *gauche* DBB is strongly suppressed, pointing to a strong conformational effect at the level of the short-range ion-molecule potential energy surface.

Finally, as a prototypical $[4 + 1^+]$ polar cycloaddition, the reaction of DBB with trapped and sympathetically cooled propene ions was explored. Both conformers of DBB were found to exhibit capture-limited rate constants towards propene ions, which implies the contribution of a stepwise and barrierless reaction pathway in parallel to the canonical concerted mechanism. With these results, the present work marks the first step towards a rigorous systematic investigation of conformational effects in polar cycloadditions.

Contents

Abstract i

1 Introduction 1
- 1.1 Controlled ion-molecule reactions in the gas phase . . . 1
  - 1.1.1 Specific reactivity of *para*- and *ortho*-water . . . 2
  - 1.1.2 Conformer-specific reactions . . . 3
- 1.2 Trapped ions . . . 6
  - 1.2.1 Ion trap principle . . . 6
  - 1.2.2 Laser cooling and Coulomb crystallization . . . 8
- 1.3 Controlled molecular beams . . . 11
  - 1.3.1 Supersonic expansion . . . 11
  - 1.3.2 Electrostatic deflection . . . 12
- 1.4 Kinetics of ion-molecule reactions . . . 14
  - 1.4.1 Rate equations . . . 14
  - 1.4.2 Ion-molecule collisions . . . 15
  - 1.4.3 Adiabatic capture theory . . . 17
- 1.5 Thesis outline . . . 20

2 Experimental Methods 21
- 2.1 Overview of the experimental setup . . . 21
- 2.2 Laser system . . . 23
- 2.3 Ion trap with integrated time-of-flight mass spectrometer . . . 24
  - 2.3.1 Trap setup . . . 24
  - 2.3.2 Coulomb crystal loading procedure . . . 24
  - 2.3.3 Ion micromotion . . . 25
  - 2.3.4 Time-of-flight mass-spectrometer . . . 26
  - 2.3.5 Molecular dynamics simulations of Coulomb crystal TOF-MS . . . 27
  - 2.3.6 Calibration of the TOF-MS sensitivity . . . 27
- 2.4 Controlled molecular beam apparatus . . . 30
  - 2.4.1 Experimental setup . . . 30
  - 2.4.2 Monte-Carlo trajectory simulations for electrostatic deflection of water . . . 31
  - 2.4.3 Molecular beam of water . . . 34
    - 2.4.3.1 Beam velocity . . . 34
    - 2.4.3.2 REMPI spectroscopy of water . . . 35

2.4.3.3 Composition of the molecular beam . . . 36
2.4.3.4 Beam density . . . 39
2.4.4 Molecular beam of DBB . . . 40
2.4.4.1 Beam velocity . . . 40
2.4.4.2 Beam density . . . 40

3 Different reactivities of *para*- and *ortho*-water towards diazenylium ions 43
3.1 Introduction . . . 43
3.2 Results . . . 45
3.2.1 Experimental approach . . . 45
3.2.2 Isomer populations in the deflected water beam . . . 45
3.2.3 Reaction-rate measurements . . . 48
3.3 Discussion . . . 51
3.4 Conclusion . . . 54

4 Generation of vacuum-ultraviolet radiation 55
4.1 Introduction . . . 55
4.2 Theoretical background . . . 56
4.3 Experimental setup . . . 58
4.4 Characterization . . . 61
4.4.1 Phase-matching . . . 61
4.4.2 Efficiency . . . 61
4.4.3 Stability . . . 63
4.4.4 VUV-induced ionization . . . 64
4.5 Conclusion . . . 66

5 Separation of the conformers of 2,3-dibromobuta-1,3-diene 67
5.1 Introduction . . . 67
5.2 Theoretical and experimental methods . . . 69
5.2.1 Theoretical screening . . . 69
5.2.2 Stark-energy and trajectory simulations . . . 70
5.2.3 Synthesis of DBB . . . 71
5.2.4 Experimental setup for conformer separation . . . 73
5.3 Results . . . 74
5.3.1 Torsional profiles of the 2,3-dihalobutadienes . . . 74
5.3.2 Simulations of the electrostatic deflection of DBB . . . 76
5.3.3 Experimental deflection profiles . . . 77
5.4 Conclusion . . . 80

6 Reaction of *gauche*- and *s-trans*-DBB with laser cooled Ca^+ ions 81
6.1 Introduction . . . 81
6.2 Results . . . 82
6.2.1 Experimental setup . . . 82
6.2.2 Reaction products . . . 83
6.2.3 Conformer-specific rate constants . . . 87
6.2.4 Adiabatic capture rate calculation . . . 89
6.2.5 Determination of Ca^+ electronic state populations . . . 91

6.2.6 Calcium-state-specific rate constants . . . 94
6.3 Conclusion . . . 95

7 Loading propene into the ion trap **97**
7.1 Introduction . . . 97
7.2 VUV ionization of propene . . . 98
7.3 Charge transfer between Ca^{2+} and propene . . . 100
7.4 Discussion and Conclusion . . . 104

8 Conformer-specific polar cycloaddition of *gauche*- and *s-trans*-DBB with trapped propene ions **107**
8.1 Introduction . . . 107
8.2 Results . . . 109
8.2.1 Experimental setup . . . 109
8.2.2 Conformer separation of DBB . . . 109
8.2.3 Reaction rate measurements . . . 111
8.2.4 Conformer-specific rate constants . . . 112
8.2.5 Reaction products . . . 112
8.3 Discussion . . . 116
8.4 Conclusion . . . 118

9 Conclusion and Outlook **119**

A Appendices **123**
A.1 Water . . . 123
A.2 VUV ionization . . . 125
A.3 NMR spectra of DBB . . . 126

Bibliography **127**

Acknowledgements **139**

1

Introduction

1.1 Controlled ion-molecule reactions in the gas phase

Chemical reactions are complex processes which involve the cooperation of many different rotational and vibrational degrees of freedom of the reactants. Whether stable bonds can be formed also depends on the way different functional groups of a molecule are oriented relative to each other. Polyatomic molecules often exhibit different conformational isomers (conformers) which can be transformed into each other by rotation about covalent bonds. Since these conformers are separated only by shallow energy barriers, they typically interconvert easily by thermal motion, making it impossible to separate and characterize them individually under standard conditions. However, in order to understand reaction mechanisms and design new synthetic methods, it is required to conceive experiments which disentangle the contributions of individual conformations of a molecule on its chemical reactivity [1].

A bottom-up approach towards such a detailed understanding of chemical reactions requires the preparation of the reactants in selected rovibrational states or conformations and to initiate the reaction in a controlled environment [1, 2, 3, 4]. Some recent successes of this approach have relied on two experimental advances: the control of neutral molecules in molecular beams [5, 6, 7] and the trapping and sympathetic cooling of molecular ions in Coulomb crystals [8, 9].

Molecular beams created by supersonic expansion allow efficient cooling of molecular rotation and vibration such that only a few quantum states remain populated. In addition, external electric or magnetic fields can then be employed to further decelerate the beam or select individual quantum states [10, 11]. In particular, the use of inhomogeneous electrostatic fields has enabled the spatial separation and selection of different molecular conformations or rotational states owing to their different electric dipole moments [12, 10, 13, 14, 15].

Trapping and laser cooling of atomic ions to mK temperatures has made it possible to create large, crystallized ion structures, called Coulomb crystals [16]. Remarkably, other molecular ions, which themselves cannot be laser-cooled, can be sympathetically cooled by trapping them together with an atomic Coulomb crystal. Cold samples of molecular ions prepared in this way can then be reacted with neutral molecules from a molecular beam source [17, 8, 9]. From this perspective, Coulomb crystals can be considered as

controlled reaction vessels in which reactant and product molecular ions are co-trapped and sympathetically cooled.

In a first pioneering experiment, a conformer-selected molecular beam of 3-aminophenol was reacted with trapped Ca^+ ions [13]. It was demonstrated that the reaction rate of the *cis* conformer of 3-aminophenol was enhanced by a factor of two compared to the *trans* conformer. This difference results from the larger dipole moment of the *cis* conformer that enables a larger scattering cross-section with the ionic reaction partner. These results gave a first glimpse of the potential of controlled reaction experiments with conformer-selected molecular beams. In this thesis, the concept of state- and conformer-selected ion-molecule reactions was developed further and applied to different systems which will be introduced briefly in the two subsequent sections.

1.1.1 Specific reactivity of *para*- and *ortho*-water

The water molecule H_2O is of fundamental importance in nature and for life on earth. Water contains two equivalent hydrogen atoms which can be exchanged by rotation about its C_2 symmetry axis. Each hydrogen carries a nuclear spin of 1/2 such that the total nuclear spin of water takes values of $I = 0$ and $I = 1$, giving rise to the two nuclear spin isomers *para*- and *ortho*-water, respectively (see Fig. 1.1). Since nuclear spin is conserved in collisions and chemical reactions, these two isomers can largely be regarded as independent chemical species [18, 19, 20].

An important consequence of the hydrogen nuclei being indistinguishable fermions is that the symmetry of the water molecule must obey the generalized Pauli principle [18]. This means that the total molecular wave function Ψ must be antisymmetric with respect to exchange of the two hydrogens. Electronic (el), vibrational (vib), rotational (rot) and nuclear spin (ns) parts of Ψ are decoupled due to their different energy scales such that Ψ can be written as the product

$$\Psi = \Psi_{\mathrm{el}}\Psi_{\mathrm{vib}}\Psi_{\mathrm{rot}}\Psi_{\mathrm{ns}}. \tag{1.1}$$

In the electronic and vibrational ground state of water, Ψ_{el} and Ψ_{vib} are symmetric [15]. To obey the Pauli principle, the symmetries of Ψ_{rot} and Ψ_{ns} must be coupled: If Ψ_{ns} is symmetric (s), then Ψ_{rot} must be antisymmetric (a), and vice versa. For *para*-water with $I = 0$, Ψ_{ns} is the antisymmetric singlet state, imposing that Ψ_{rot} must be symmetric. On the other hand, *ortho*-water is in a symmetric triplet spin configuration, such that Ψ_{rot} must be antisymmetric.

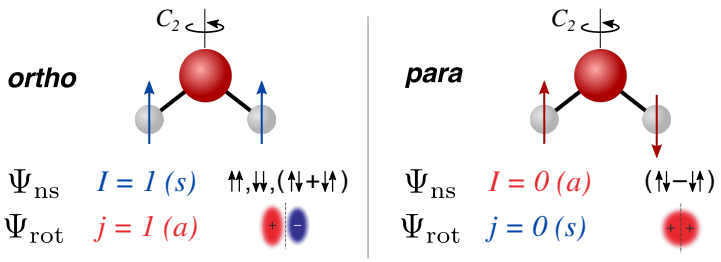

Figure 1.1: Nuclear spin and rotational symmetry of the ground states of *ortho*-water (left) and *para*-water (right).

The rotational states of water can be labelled as $|j_{K_aK_c}M\rangle$, where j is the angular momentum quantum number, K_a and K_c are pseudo quantum numbers denoting the projections onto the a and c principal axes of inertia, and M is the projection onto a space-fixed axis. Since M is not important for the symmetry considerations, it is dropped in the following discussion. To identify the symmetry of $|j_{K_aK_c}\rangle$ under exchange of the hydrogens, one determines how these states transform under a 180° rotation about the C_2-axis. The C_2 rotation can be expressed as consecutive 180° rotations about the a and c inertial axes of water [15]. Consequently, the state $|j_{K_aK_c}\rangle$ acquires the sign $(-1)^{K_a+K_c}$ under action of C_2. Hence, $|j_{K_aK_c}\rangle$ is symmetric (antisymmetric) if $K_a + K_c$ is even (odd). The generalized Pauli principle then demands that *para*-water only has rotational states with even values of $K_a + K_c$ and *ortho*-water only has rotational states with odd $K_a + K_c$. In particular, the ground state of *para*-water is the absolute ground state $|0_{00}\rangle$ with $j = 0$ and the ground state of *ortho*-water is the first excited rotational state $|1_{01}\rangle$ [15] (Fig. 1.1).

This interplay between nuclear spin and rotational angular momentum leads to different physical properties of the *para* and *ortho* isomers of water, which were exploited by Horke et al. [15] to spatially separate them in a molecular beam. In this experiment, it was achieved to create nearly pure samples of either isomer. In chapter 3 of this thesis, a similar nuclear-spin-selected molecular beam of *para*- and *ortho*-water was employed for reaction experiments with trapped diazenylium ions (N_2H^+) [21]. The rotational excitation of *ortho*-water was found to suppress its reaction rate constant with N_2H^+ compared to the non-rotating *para*-water.

1.1.2 Conformer-specific reactions

An exciting opportunity for experiments with conformer-selected reactants is organic synthesis. Due to their high stereo- and regioselectivity, cycloadditions are of exceptional importance for organic synthesis [22, 23]. A prominent cycloaddition is the Diels Alder (DA) reaction [24, 25, 26] in which a diene reacts with a dieneophile to form a cyclohexene derivative (see Fig. 1.2). Here, 4 π-electrons of the diene interact with 2 π-electrons of the dieneophile, which is usually expressed using the notation [4+2]. During the DA reaction, two new σ bonds and one π bond are formed via a synchronous concerted transition state (TS), in which bond breaking and bond formation occur simultaneously. The DA reaction thus allows the formation of large and stereochemically intricate molecules in only a single step.

To explain the pericyclic reaction mechanism of the DA reaction, Woodward-Hoffmann rules are usually invoked [27]. These impose that the mirror symmetry about the center of the reactants must be conserved throughout the reaction. Only molecular orbitals (MOs) of the same symmetry can thus form chemical bonds. This principle is sketched in the correlation diagram shown in Fig. 1.2, where bond formation between the highest occupied molecular orbital (HOMO) of the diene and the lowest unoccupied molecular orbital (LUMO) is indicated. To enhance reactivity, the energy levels of the bonding MOs must be matched. A common way to achieve this is by modifying the electron density in the π-electron systems with electron-donating and electron-withdrawing substituents on the diene and dienophile, respectively [23].

Fig. 1.3a shows possible reaction pathways for the neutral $[4 + 2]$ cycloaddition. The

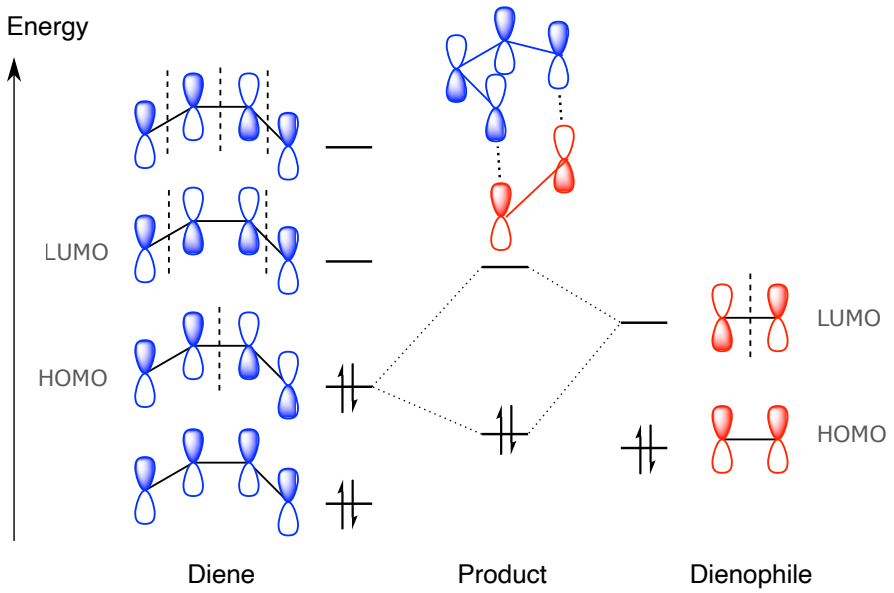

Figure 1.2: MO correlation diagram for the neutral [4 + 2] cycloaddition. Nodal planes of the reactant MOs are indicated by dashed lines. The central MO shows the concerted transition state which has the same mirror symmetry as the reactant MOs.

reaction via the concerted transition state TS_c (purple arrow) has a low energy barrier along the reaction coordinate because the TS is stabilized by Hückel aromaticity [26]. Alternative two-step pathways with zwitter-ion or diradical intermediates (I) have higher energy barriers and are thus less favorable. Preference for the highly symmetric concerted pathway explains why the DA reaction generally affords high stereo- and regioselectivity of the cycloadduct. Another important consequence of this is that the reaction proceeds exclusively from the *s-cis* conformer of the diene and not from the *s-trans* conformer, which is unable to form the concerted TS. However, this simple model tends to break down in cases where the reactants possess complex functional groups and the overall symmetry is reduced. In these cases, an asynchronous or stepwise mechanism becomes also possible and also allows the *s-trans* conformer to contribute to product formation [28].

These considerations apply to neutral reaction partners. In case one of the reactants is charged, however, the situation changes dramatically. Removal of one electron from the dienophile leads to a $[4 + 1^+]$ polar cycloaddition [29], which is a highly activated radical cation reaction (Fig. 1.3b). The lack of one electron prevents formation of an aromatic transition state, thereby raising the energy barrier of the concerted pathway considerably ($TS_c^{\cdot+}$). In turn, the ionic character of the dienophile makes the two-step pathway energetically more favourable [30, 31, 32]. This would allow the *trans*-conformer of the diene to participate in the formation of the cycloadduct at a comparable rate.

Based on this reasoning, crucial insight about the reaction mechanism of the polar cycloaddition can be obtained by studying the individual chemical reactivities of the *cis* and *trans* conformers of the diene. In order to be compatible with the conditions for

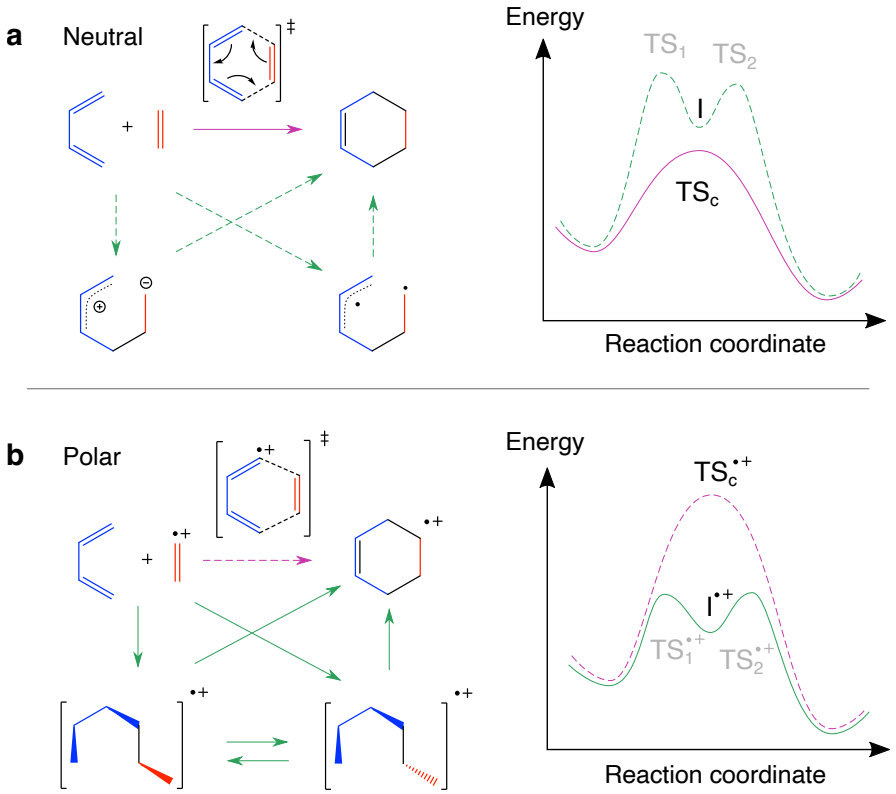

Figure 1.3: Comparison of proposed reaction mechanisms for the neutral (**a**) and polar DA cycloaddition (**b**) of butadiene and ethene. The reaction mechanisms are displayed in the left half while the right half shows corresponding schematic energy curves along the reaction coordinate.

conformer separation in a molecular beam, a suitable diene was identified using high-level quantum chemical screening[1]. The successful candidate, 2,3-dibromobutadiene (DBB), exists in an apolar *s-trans* and a strongly polar *gauche* conformation which facilitates their electrostatic separation (see chapter 5 and ref. [33]).

With DBB, the conformer-selective investigation of a complex organic cycloaddition reaction in the gas phase became possible. After separating the *gauche*- and *s-trans*-conformers of DBB in a molecular beam, they were reacted with trapped propene ions to undergo a $[4+1^+]$ polar cycloaddition (see chapter 8). Probing the conformer-specific reaction rate constants revealed that both the *gauche* as well as the *s-trans* conformer exhibit capture-limited reaction rate constants of comparable magnitude towards propene ions. This observation implies the absence of potential energy barriers induced by transition states. Moreover, as supported by ab-initio calculations, it shows that an efficient stepwise reaction pathways exists for the *s-trans* conformer that is competitive with a possibly concerted pathway for the *gauche* conformer.

[1]The screening was performed by the group of Prof. O. A. von Lilienfeld.

1.2 Trapped ions

1.2.1 Ion trap principle

Ion traps were first developed in mass spectrometry for mass selection and storage [34]. Today, they have also become a versatile tool for spectroscopy as well as quantum computation [35, 36]. Recently, the trapping of large Coulomb crystals of laser-cooled atomic ions has enabled sympathetic cooling and trapping of molecular ions, paving the way for the investigation of cold chemical reactions between sympathetically cooled molecular ions and neutral molecules [16, 17, 8].

Since a purely static electric potential cannot exhibit a local minimum to confine a charged particle in all three dimensions, time-varying electric fields in the radio-frequency (RF) domain have to be used for ion trapping. The most popular trap design for modern experiments with trapped atomic ions are linear quadrupole ion traps (LQT) [35, 17]. The schematic of the LQT used in this thesis is shown in Fig. 1.4a. It consists of four parallel rods, each carrying three electrode segments. To create a harmonic potential along the z symmetry axis, a static DC (direct current) voltage V_{DC} is applied to the outer electrode segments, the end-caps. In addition, sinusoidal RF voltages $V_{\mathrm{RF}}(t) = V_0 \cos(\Omega_{\mathrm{RF}} t)$, with amplitude V_0 and frequency Ω_{RF}, are applied to all three segments of each rod. The RF voltages have the same polarity on opposite rods ($+V_{\mathrm{RF}}$) and inverted polarity on adjacent rods ($-V_{\mathrm{RF}}$). At the trap center, this generates the total electrostatic potential

$$\Phi(x,y,z) = \kappa \frac{V_{\mathrm{DC}}}{2z_0^2}\left(2z^2 - x^2 - y^2\right) + \frac{V_0}{r_0^2}\left(x^2 - y^2\right)\cos(\Omega_{\mathrm{RF}} t), \tag{1.2}$$

where $2z_0$ is the distance between the end caps, $2r_0$ is the diagonal distance between rods and κ is a geometrical factor. The RF potential has the shape of a rotating saddle inducing confinement along one axis and de-confinement along the other orthogonal axis. If the rotation of the potential at frequency Ω_{RF} is much faster than the response time of an ion, it experiences a time-averaged restoring force which leads to stable trapping.

The equations of motion for an ion with charge q and mass m can be written in the form of Matthieu equations ($u \in \{x, y, z\}$)

$$\ddot{u}(t) + \frac{\Omega_{\mathrm{RF}}^2}{4}(a_u + 2q_u \cos(\Omega_{\mathrm{RF}} t))u(t) = 0, \tag{1.3}$$

with Mathieu parameters

$$a_x = a_y = -\frac{a_z}{2} = -\kappa \frac{4qV_{\mathrm{DC}}}{m z_0^2 \Omega_{\mathrm{RF}}^2}, \tag{1.4}$$

$$q_x = -q_y = \frac{4qV_0}{m r_0^2 \Omega_{\mathrm{RF}}^2}, \quad q_z = 0. \tag{1.5}$$

Along the z-axis, the ion oscillates in a harmonic potential with axial trap frequency $\omega_z = \sqrt{a_z}\Omega_{\mathrm{RF}}/2$. Due to the oscillating trap voltages, the ion's motion along the radial x and y directions evolves on two timescales: there is a slow secular motion of the ion's average position and a fast micromotion, oscillating at the RF frequency Ω_{RF}. The radial secular trap frequency is

$$\omega_r = \frac{\Omega_{\mathrm{RF}}}{2}\sqrt{a_x + \frac{q_x^2}{2}}. \tag{1.6}$$

To achieve stable trajectories along x and y, the parameters a_x, q_x have to be adjusted by means of the voltages V_{DC}, V_0 and the Ω_{RF}. Qualitatively, stable trapping is achieved if ω_r is much smaller than Ω_{RF}, i.e. $\omega_r \ll \Omega_{\mathrm{RF}}$. This condition reinstates the separation of timescales between the slow secular motion and the fast micromotion. Stability diagrams are usually invoked to find precise constraints on a_u and q_u for ion trapping. The effective

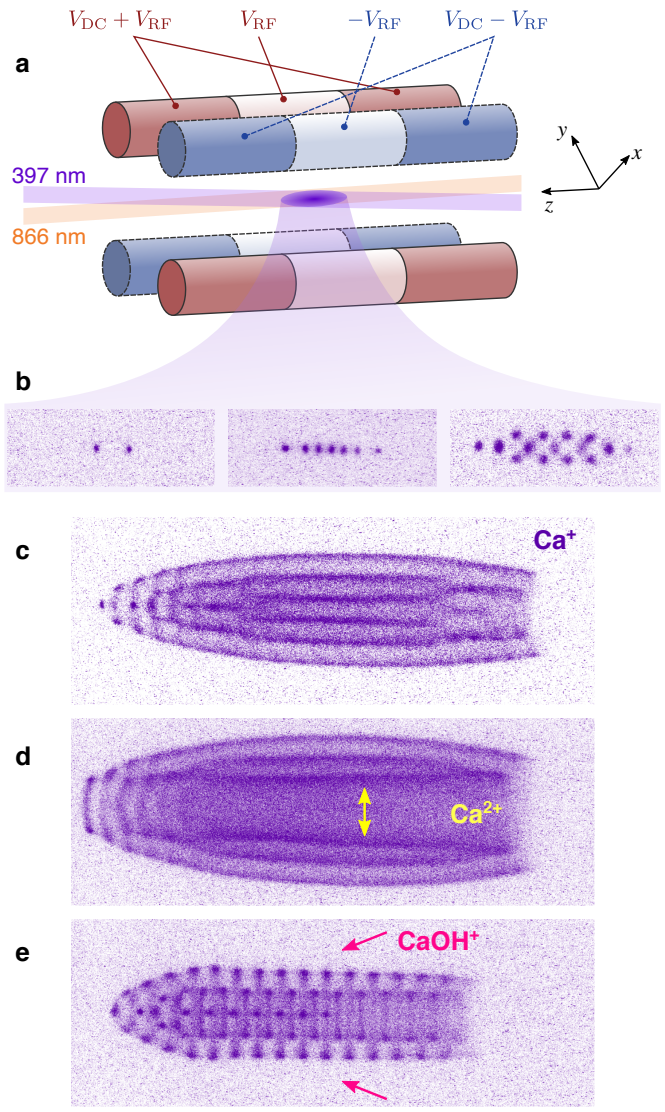

Figure 1.4: Ion trap overview. **a**, schematic of a LQT with four segmented electrode rods. Ca^+ ions are trapped at the center and cooled by laser beams at 397 nm and 866 nm. **b**, fluorescence images of small Ca^+ Coulomb crystals where individual ions are discernible. **c**, Large Ca^+ crystal with approximately 500 ions. The indent on the right is due to radiation pressure of the cooling laser. **d** and **e** show Ca^+ Coulomb crystals with sympathetically cooled Ca^{2+} and $CaOH^+$ ions, respectively. The Ca^{2+} ions with smaller mass/charge ratio accumulate at the trap center, while the heavier $CaOH^+$ ions form a shell around the Ca^+ core.

trapping potential for radial secular motion can be written as

$$\Phi_{\text{eff}}(x, y) = \frac{m\omega_r^2}{2}(x^2 + y^2) \tag{1.7}$$

Interestingly, Φ_{eff} directly corresponds to the average kinetic energy of the micromotion. Consequently, the further an ion is located away from the cylinder axis $x = y = 0$ of the trap, where the RF component of the electrode potential Φ vanishes, the stronger becomes its micromotion.

1.2.2 Laser cooling and Coulomb crystallization

When ions are loaded into the LQT by ionization of a thermal vapour of neutral atoms, this produces hot ions in the trap with a short trap lifetime. To obtain control over the ions and confine them more strongly to the center of the trap, laser cooling is employed. Laser cooling has allowed the preparation of trapped ions in their motional quantum ground states [37, 35] as well as the production of ultracold atomic clouds and quantum gases of neutral atoms [38, 39].

The principle of laser cooling [38] is based on the momentum recoil an atom experiences when it scatters a photon from a laser beam, i.e. radiation pressure. To slow down an atom using a laser beam, one exploits the Doppler shift of the laser frequency seen by a moving atom. Near an atomic transition, the scattering rate is greatly enhanced and strongly depends on the detuning of the laser frequency relative to the atomic transition frequency. When the laser frequency is tuned slightly to the red of the atomic transition, the Doppler shift of an atom moving towards the laser reduces the detuning and increases the scattering rate. If instead the atom is at rest or moves in the same direction as the laser beam, the scattering rate stays small or decreases. This selectively decelerates an atom when it moves towards the laser. To cool an atom in free-space, one thus needs two counter-propagating laser beams to cool in forward and backward direction. In an ion trap, however, the ion oscillates back and forth at the secular trap frequency ω_u. Thus, ions are forced to periodically move towards an incident laser beam that is aligned with the trap axis. Consequently, ions are cooled in every half-cycle of the trap oscillation [40], such that a single laser beam is sufficient for cooling. For simultaneous cooling along all three trap axes, the laser beam needs to be aligned such that it has some overlap with all of them. In addition, Coulomb repulsion between multiple ions in a trap perturbs their harmonic motion and redistributes translational energy between the different axes, thus facilitating the cooling.

Experiments in this thesis were conducted with Calcium (Ca) ions. A diagram of the lowest electronic levels of Ca^+ is shown in Fig. 1.5. Ca^+ has one $^2S_{1/2}$ electronic ground state which is coupled to two $^2P_{1/2}$ and $^2P_{3/2}$ excited states via optical dipole transitions in the ultraviolet (UV). These P states have further near-infrared (IR) optical dipole transitions to lower lying $^2D_{5/2}$ and $^2D_{3/2}$ states [41]. For laser cooling of Ca^+, a closed system consisting of the optical transitions $^2S_{1/2} \rightarrow {}^2P_{1/2}$ at 397 nm and $^2D_{3/2} \rightarrow {}^2P_{1/2}$ at 866 nm was employed. The $^2S_{1/2} \rightarrow {}^2P_{1/2}$ transition has a large spontaneous emission rate of $\Gamma_{397} = 2\pi \times 21$ MHz and was used as the primary cooling transition. To repump ions from the $^2D_{3/2}$ back to the $^2S_{1/2}$ state and into the cooling cycle, the weaker $^2D_{3/2} \rightarrow {}^2P_{1/2}$ transition with $\Gamma_{866} = 2\pi \times 1.7$ MHz had to be driven, too.

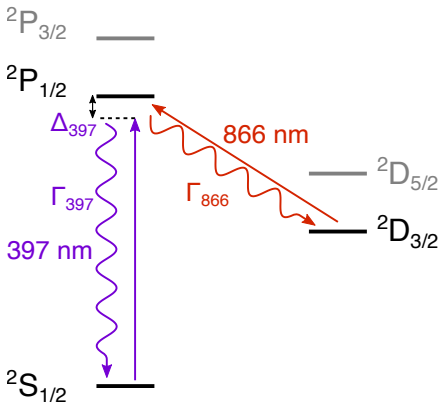

Figure 1.5: Level diagram of Ca^+ with cooling transition at 397 nm and repumping transition at 866 nm.

Doppler laser cooling on the $^2S_{1/2} \rightarrow {}^2P_{1/2}$ transition allows a minimum temperature of $T_D = \hbar\Gamma_{397}/(2k_B) \approx 0.5$ mK to be reached at a red detuning of $\Delta_{397} = -\Gamma_{397}/2$ of the cooling laser [38]. Here, $\hbar$ is the reduced Planck constant and k_B is the Boltzmann constant. When a large number of trapped ions is cooled to such mK-temperatures they start to arrange in spatially ordered structures, called "Coulomb crystals" due to their quasi-crystalline appearance [16]. In a Coulomb crystal, the thermal kinetic energy of the ions is much smaller than the Coulomb repulsion between them and the external trapping potential. This leads to a localization of the ions, which can be expressed quantitatively by the plasma coupling parameter [17, 8]

$$\Gamma = \frac{q^2}{4\pi\epsilon_0 a_{\mathrm{WS}} k_B T} \tag{1.8}$$

which is the ratio of potential energy over kinetic energy. Here, the Wigner-Seitz radius is $a_{\mathrm{WS}} = (3/(4\pi\rho))^{1/3}$ for an ion density ρ, ϵ_0 is the dielectric permittivity, k_B is the Boltzmann constant and T is the temperature. Theoretical simulations have shown that Coulomb crystallisation occurs for $\Gamma \sim 150$ [42, 43, 44]. Fig. 1.4b shows experimental images of Ca^+ Coulomb crystals of varying size. They are obtained by imaging the fluorescence of the Ca^+ ions due to the 397 nm cooling laser onto a charge-coupled-device (CCD) camera. Clearly, individual ions can be resolved. In Fig. 1.4c, a large Coulomb crystal consisting of approximately 500 ions is shown, which is the typical size used for reaction experiments.

Coulomb crystals are an important tool for precision spectroscopy as well as the investigation of cold chemical reactions between trapped ions and neutral molecules [17, 8, 9]. The low ion temperatures achieved in Coulomb crystals allow good control over the collision energy with other reactants, such as molecular beams. Moreover, Coulomb crystals enable very long storage times in the ion trap, which is essential for the study of chemical reactions taking place at the second or minute timescale. Another important aspect is that Coulomb crystals of atomic ions can serve as a refrigerator for other molecular ion species, which cannot be laser-cooled. When molecular ions are loaded into the ion trap, collisions transfer their kinetic energy to the laser-cooled ions. This results in their sympathetic cooling [45].

Figs. 1.4d and e show images of mixed species Coulomb crystals, which contain next to Ca^+ also non-fluorescing Ca^{2+} and $CaOH^+$, respectively. Due to the dependence $\omega_r \propto q/m$ of the radial secular trap frequency on the mass and charge of the ion, lighter ions are more strongly confined than heavier ions. In an ion trap with mixed ion species, Coulomb repulsion between the ions then enforces a spatial ordering of ions according to their mass-to-charge ratio m/q. Lighter, or doubly charged ions experience a tighter trap (large ω_r) and thus accumulate at the center. Heavy ions, on the other hand, feel a relaxed trap and are repelled to larger distances from the trap center.

This spatial ordering of ions according to their m/q ratio has consequences for micromotion heating and sympathetic cooling efficiency. Sympathetic cooling necessitates collisions with the laser-cooled species. Hence, it is the most efficient if the laser-cooled species and the sympathetically cooled species have equal mass [45]. If the laser-cooled species has larger m/q, it will surround the other species such that cooling is improved (Fig. 1.4d). By contrast, if the laser-cooled species has lower m/q, like in Fig. 1.4e, the sympathetically cooled ions surround the laser-cooled ions and their displacement from the trap axis increases. The reduced contact with the laser-cooled ions leads to less efficient sympathetic cooling. Moreover, micromotion heating increases with radial displacement and results in excess heating. Consequently, good sympathetic cooling efficiency, which is a prerequisite for control of the molecular ion, is best achieved using heavy laser-cooled ions.

1.3 Controlled molecular beams

Polyatomic molecules possess a wealth of rotational, vibrational and electronic degrees of freedom. This makes it much harder to control them than atoms, and in general prevents direct laser cooling. Nevertheless, experimental techniques to cool and control neutral molecules have been developed using molecular beams obtained by supersonic expansion into vacuum [5, 46, 11, 6]. These methods enable the versatile preparation of neutral molecules in low-temperature states where only a few or even single quantum states are populated. Inside the molecular beam, the low translational temperature inhibits collisions between the molecules such that rovibrational states and molecular conformations are preserved. By application of external electric or magnetic fields, molecular beams can be further manipulated for deceleration or state selection [11, 6].

1.3.1 Supersonic expansion

The principle of supersonic expansion [47, 48] relies on the adiabatic expansion of a gas, as it passes from a high-pressure reservoir through a nozzle into a high-vacuum chamber. During this fast and adiabatic process, the gas molecules undergo rapid collisions which efficiently convert their thermal internal energy into kinetic energy. The resulting molecular beam then propagates at supersonic velocities and is composed of molecules whose internal vibration and rotation are cooled so low that only a few quantum states are populated.

The fast adiabatic expansion of the gas conserves the enthalpy, i.e.

$$H = U + pV + \frac{1}{2}Mv^2 \tag{1.9}$$

where U is the internal energy, composed of contributions from molecular translation, vibration, rotation and electronic motion, p is the pressure, V is the volume, M is the total mass and v is the mean velocity of the gas. Equating the enthalpy in the reservoir (res) with that in the molecular beam, one finds that the kinetic energy of the beam is [47]

$$\frac{1}{2}Mv_{\text{beam}}^2 \approx (U_{\text{res}} - U_{\text{beam}}) + p_{\text{res}}V_{\text{res}}, \tag{1.10}$$

Consequently, the enthalpy of the reservoir is converted into kinetic energy of the expanding beam. If all enthalpy is efficiently converted into kinetic energy, then $U_{\text{beam}} \ll U_{\text{res}}$ and the molecules in the expansion are internally cooled. To improve the cooling efficiency, the gas molecules must transfer their translational, vibrational and rotational energy into kinetic energy by inelastic collisions within the nozzle. This is facilitated using a high gas pressure in the reservoir.

For perfect cooling efficiency, the maximum terminal velocity of the supersonic jet can be calculated as [48]

$$v_{\text{beam}} \approx \sqrt{\frac{2k_BT_{\text{res}}}{m}\frac{\gamma}{\gamma-1}} \tag{1.11}$$

where k_B is the Boltzmann constant, T_{res} is the reservoir temperature, m is the molecular mass and $\gamma = 1 + 2/f$ is the adiabatic coefficient of the gas with f degrees of freedom

(translation + vibration + rotation). This velocity exceeds the speed of sound in the medium.

In a supersonic expansion of a gas mixture, where a small fraction of one species is seeded into a carrier gas of another (percent level), the seed gas reaches the same velocity as the carrier gas and is efficiently cooled by the carrier gas. Relative translational motion is typically very efficiently cooled to ~ 1 K. For rotation and vibration, the final temperature depends on the rovibrational energy level spacing [47, 48]. The smaller energy spacing of rotational compared to vibrational levels allows rotation to be cooled more efficiently.

After the supersonic jet has exited the nozzle, skimmers placed in the beam path help to select only the central part of the beam, which has the lowest translational temperature. Subsequently, external fields are applied to further control the molecular quantum states.

1.3.2 Electrostatic deflection

A molecule with electric dipole moment $\boldsymbol{\mu}_e$ in an external electric field $\boldsymbol{\mathcal{E}}$ is subject to the Stark effect [49]

$$H_{\text{Stark}} = -\boldsymbol{\mu}_e \cdot \boldsymbol{\mathcal{E}}, \tag{1.12}$$

which is the projection of the dipole moment onto the electric field vector. The strength of the associated Stark energy shift depends on both the orientation of the molecule relative to the electric field and the orientation of the dipole moment relative to the molecule's symmetry axes, i.e. the principal axes of inertia. Consequently, H_{Stark} couples different molecular rotational states. For a polyatomic molecule, the rotational Hamiltonian reads

$$H_{\text{rot}} = h\left(Aj_a^2 + Bj_b^2 + Cj_c^2\right) \tag{1.13}$$

where $A = h/(8\pi^2 I_a)$, $B = h/(8\pi^2 I_b)$ and $C = h/(8\pi^2 I_c)$ are rotational constants with I_a, I_b and I_c being the moments of inertia of the molecule along the principal axes a, b and c, respectively. The operators j_k $(k = a, b, c)$ are the components of the molecular rotational angular momentum $\boldsymbol{j}$ along the principal axes. The geometry and principal axes of DBB are depicted in Fig. 1.6.

For a symmetric top molecule with $A = B \neq C$, H_{rot} is diagonal in the rotational state basis $|jKM\rangle$ where $j \in \mathbb{N}_0$ is the rotational angular momentum quantum number and K and M are the quantum numbers of the angular momentum projections onto the molecule-fixed c-axis and the lab-fixed field-axis, respectively $(K, M \in \{-j, -j+1, ..., j\})$. The field-free rotational energy is then $E_{JKM} = h\left[Bj(j+1) + (C-B)K^2\right]$. A special case is a linear molecule for which $C \to \infty$ and thus $K = 0$. For asymmetric top molecules with $A > B > C$ $(I_a < I_b < I_c)$, H_{rot} is not diagonal in the $|jKM\rangle$ basis. Instead, it must be diagonalized numerically. To classify the eigenvalues of H_{rot}, the rotational states are labelled $|j_{\text{K}_a\text{K}_c}M\rangle$. Here, K_a and K_c are pseudo quantum numbers giving the projections of $\boldsymbol{j}$ onto the molecular a and c axes, respectively [10, 50]. They take values $j \leq K_a + K_c \leq j+1$.

The full Hamiltonian $H_{\text{tot}} = H_{\text{rot}} + H_{\text{Stark}}$ must be diagonalized numerically for any given field strength $\mathcal{E}$, which was done using the software package CMISTARK [49]. This yields the eigenvalues $E_{j_{K_a K_c} M}(\mathcal{E})$, which are called the Stark energies. If a molecule moves through an inhomogeneous electric field with slowly varying field strength

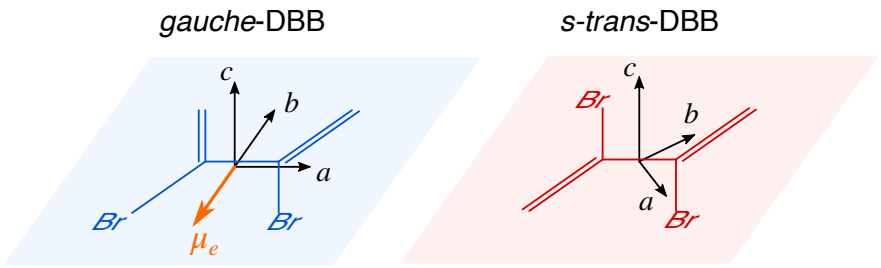

Figure 1.6: Sketch of the geometries of *gauche*-DBB (left) and *s-trans*-DBB (right) with inertial coordinate system and dipole moment. Note that in reality, gauche-DBB is not exactly planar as drawn here. *S-trans*-DBB is inversion-symmetric and therefore has no permanent dipole moment.

$\mathcal{E}(\boldsymbol{r})$ (position vector $\boldsymbol{r}$), it adiabatically remains in an eigenstate $|j_{K_a K_c} M\rangle$ of H_{tot} [6] such that its energy is given by the Stark energy $E_{j_{K_a K_c} M}(\mathcal{E})$. The spatial variation of $E_{j_{K_a K_c} M}$ then results in the force

$$m\ddot{\boldsymbol{r}} = \boldsymbol{F}_{\text{Stark}} = -\nabla E_{j_{K_a K_c} M}(\mathcal{E}(\mathbf{r})) = \mu_{\text{eff}}(\mathcal{E}) \nabla \mathcal{E}(\mathbf{r}) \tag{1.14}$$

with effective dipole moment

$$\mu_{\text{eff}}(\mathcal{E}) = -\frac{d}{d\mathcal{E}} E_{j_{K_a K_c} M}(\mathcal{E}) \tag{1.15}$$

If the field gradient is entirely along the y-axis, this results in an acceleration

$$\ddot{y} = \frac{\mu_{\text{eff}}(\mathcal{E})}{m} \frac{\partial \mathcal{E}}{\partial y} \tag{1.16}$$

that deflects the molecules along the y-axis with a strength proportional to the ratio of effective dipole moment over mass. Since the acceleration depends on both the electric dipole moment μ_e and the rotational state $j_{K_a K_c}$, this allows the spatial separation of molecules according to their dipole moment or their rotational state [10].

Rotational states can be grouped into two categories according to the sign of their Stark energy shift or effective dipole moment. States for which the energy decreases with applied electric field ($\mu_{\text{eff}} > 0$) are called high-field seekers (HFS) and states whose energy increases with applied field ($\mu_{\text{eff}} < 0$) are low-field seekers (LFS). In an electric field gradient, HFS experience a force $\boldsymbol{F}_{\text{Stark}}$ towards spatial regions of strong field while LFS are attracted to field minima. Consequently, HFS and LFS are deflected into different directions. It is noted that at sufficiently strong field, where H_{Stark} overwhelms the energy spacing between rotational eigenstates of H_{rot}, all states eventually become high-field seeking [6].

1.4 Kinetics of ion-molecule reactions

1.4.1 Rate equations

Consider the general bimolecular reaction

$$\mathrm{A} + \mathrm{B} \rightarrow \mathrm{C} + \mathrm{D} \tag{1.17}$$

from reactants A, B to products C, D. The kinetics of this reaction [51] with rate constant k can be expressed in the form of differential equations for the densities n_X of each species $\mathrm{X} \in \{\mathrm{A}, \mathrm{B}, \mathrm{C}, \mathrm{D}\}$,

$$\dot{n}_\mathrm{A} = \dot{n}_\mathrm{B} = -k\, n_\mathrm{A} n_\mathrm{B} \tag{1.18}$$

$$\dot{n}_\mathrm{C} = \dot{n}_\mathrm{D} = +k\, n_\mathrm{A} n_\mathrm{B} \tag{1.19}$$

The rate equations of such a bimolecular reaction cannot be integrated analytically. However, the experimental conditions are typically such that the density of one reactant is much larger than the other, i.e. $n_\mathrm{B} \gg n_\mathrm{A}$. For example, in the reaction of trapped ions A with neutral molecules B from a molecular beam, the density of B is continuously replenished such that n_B remains constant over time. One can then define a pseudo-first-order rate constant $\tilde{k} = k n_\mathrm{B}$ which simplifies equation (1.18) to the unimolecular rate law

$$\dot{n}_\mathrm{A} = -\tilde{k}\, n_\mathrm{A} \tag{1.20}$$

which has the simple solution

$$n_\mathrm{A}(t) = n_\mathrm{A}(0) e^{-\tilde{k}t} \tag{1.21}$$

of an exponential decay at rate $\tilde{k}$. Inserting this into (1.19) then yields the time-dependent product density

$$n_\mathrm{C}(t) = n_\mathrm{C}(0) + \tilde{k} \int_0^t n_\mathrm{A}(t')dt' = n_\mathrm{C}(0) + n_\mathrm{A}(0) \left(1 - e^{-\tilde{k}t}\right) \tag{1.22}$$

Usually, the initial product density is zero, i.e. $n_\mathrm{C}(0) = 0$. Product formation hence follows an exponentially saturating curve with same rate constant $\tilde{k}$ as for the reactant decay, reflecting that the total number of reactants and products is conserved. Experimentally, measuring the depletion of reactant A and fitting it with the pseudo-first-order model (1.21) determines the value of $\tilde{k}$. In addition, knowing the density of species B then allows one to compute the bimolecular rate constant $k = \tilde{k}/n_B$.

A slight variation of reaction (1.17) is obtained for multiple product channels, i.e.

$$\mathrm{A} + \mathrm{B} \rightarrow \mathrm{C}_1 + \mathrm{D}_1 + \ldots \tag{1.23}$$

$$\rightarrow \mathrm{C}_2 + \mathrm{D}_2 + \ldots \tag{1.24}$$

$$\ldots$$

with products $\mathrm{C_i}, \mathrm{D_i}, \ldots$ in each channel $i = 1, 2, \ldots, m$, with m being the total number of channels. Each channel has an associated rate k_i. Then, the total reaction rate constant

is $k_{\mathrm{tot}} = k_1 + \ldots + k_m$. Assuming again pseudo-first-order kinetics with rates $\tilde{k}_{\mathrm{tot}} = k_{\mathrm{tot}} n_{\mathrm{B}}$ and $\tilde{k}_i = k_i n_{\mathrm{B}}$, one finds

$$n_{\mathrm{A}}(t) = n_{\mathrm{A}}(0) e^{-\tilde{k}_{\mathrm{tot}} t} \tag{1.25}$$

$$n_{\mathrm{C_i}}(t) = n_{\mathrm{A}}(0) \frac{k_i}{k_{\mathrm{tot}}} \left(1 - e^{-\tilde{k}_{\mathrm{tot}} t}\right) \tag{1.26}$$

This shows that in the limit of long reaction time, the fractional yield of each product,

$$\frac{n_{\mathrm{C_i}}(t)}{n_{\mathrm{A}}(0)} \to \frac{k_i}{k_{\mathrm{tot}}} \quad \text{for } t \to \infty \tag{1.27}$$

converges to the branching ratio k_i / k_{tot}.

1.4.2 Ion-molecule collisions

Gas-phase reactions between neutral molecules often involve an energy barrier separating the reactants from the products. Such an energy barrier E_0 gives rise to an Arrhenius law [51], i.e. an exponential dependence $k \propto e^{-E_0/(k_B T)}$ of the rate constant k on temperature T. In case of an Arrhenius law, the reaction needs to be activated by thermal energy, leading to a decrease of the rate constant with a reduction in temperature. For reactions between ions and neutral molecules, on the contrary, a different relationship between temperature and reaction rate constant has often been observed [52]. Due to the absence of an energy barrier, ion-molecule reaction rate constants either show no pronounced temperature dependence or even an inverse temperature dependence, where the rate constant increases with a lowering of the temperature. Explaining these effects was crucial for the understanding of chemical processes in the interstellar medium, in particular the formation of polyatomic molecules under such harsh conditions [53, 54, 55].

To theoretically describe rate constants for ion-molecule reactions without energy barriers, capture models have successfully been employed [56, 57, 52]. Due to the absence of a barrier, it is assumed that the reaction rate is entirely determined by the long-range interaction potential between the charge of the ion and the dipole moment of the neutral molecule. This long-range potential has the form [52]

$$V_{\mathrm{int}}(R, \beta) = -\frac{q^2 \alpha}{4\pi\epsilon_0} \frac{1}{2R^4} - \frac{q \mu_e}{4\pi\epsilon_0} \frac{\cos\beta}{R^2}, \tag{1.28}$$

where q is the ion charge, α is the isotropic polarizability volume of the neutral, μ_e the permanent electric dipole moment of the neutral and $\mu = m_1 m_2/(m_1 + m_2)$ is the reduced mass of the collision partners with individual masses m_1, m_2. The ion-molecule distance is denoted R and the orientation angle of the molecular dipole relative to the ion-molecule axis is denoted β. The two terms in equation (1.28) are the charge–induced-dipole and the charge–permanent-dipole interactions, respectively. While the former interaction is isotropic, the latter depends on the orientation of the molecule's permanent electric dipole moment relative to the Coulomb electric field of the ionic charge. This orientation dependence makes a quantum mechanical treatment of molecular rotation necessary for an accurate description of reactions with polar molecules [52].

A sketch of the scattering geometry is displayed in Fig. 1.7a. The molecule approaches the ion with relative collision velocity v_c. Initially, the molecular trajectory is offset from

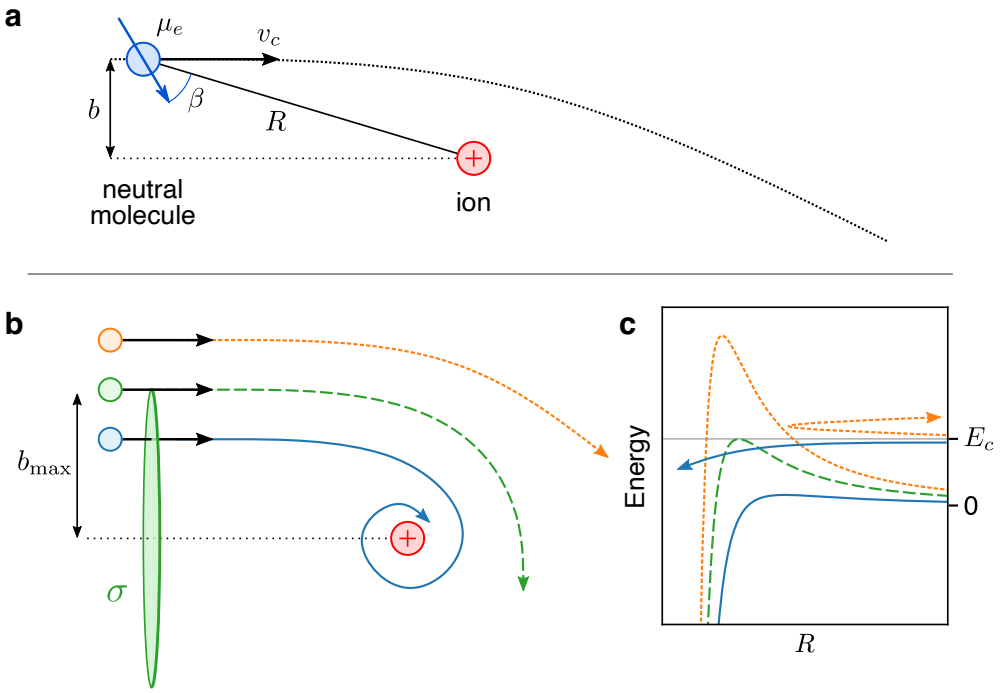

Figure 1.7: Illustration of reactive scattering between a neutral molecule and an ion. **a**, sketch of the scattering geometry. **b**, three different classical scattering trajectories with different impact parameters: $b < b_{max}$ (blue, solid line), $b = b_{max}$ (green, dashed line), $b > b_{max}$ (orange, dotted line). The collision leads to a reaction only for $b < b_{max}$. **c**, sketch of the effective potential energy $V_{eff}(R)$ for the three cases of **b**. A centrifugal barrier builds up with increasing value of b. Only reactions where the collision energy exceeds the centrifugal barrier lead to a reaction.

a head-on collision trajectory by the impact parameter b and then bends due to the interaction with the ion. The impact parameter and collision velocity define the classical angular momentum $L = \mu v_c b$ of the collision partners. This angular momentum gives rise to an effective potential

$$V_{eff}(R, \beta) = \frac{L^2}{2\mu R^2} + V_{int}(R, \beta), \tag{1.29}$$

where the first term represents the build-up of a centrifugal energy barrier with increasing value of L. The principal assumption of capture models is that any collision for which the collision energy $E_c = \mu v_c^2/2$ exceeds the centrifugal barrier leads to a reaction with unit probability. Collisions with E_c below the centrifugal barrier are non-reactive (see Fig. 1.7b and c). This results in a maximum impact parameter b_{max}, or equivalently a maximum angular momentum $L_{max}(E_c)$, defined by the condition $V_{eff}(R) \leq E_c$ for any R. The capture cross-section is then given by

$$\sigma = \pi b_{max}^2 = \frac{\pi L_{max}^2}{2\mu E_c} \tag{1.30}$$

and the reaction rate constant is $k = \sigma v_c$. For apolar molecules ($\mu_e = 0$), this leads to

the Langevin rate constant [52]

$$k_L = 2\pi\sqrt{\frac{\alpha q^2}{4\pi\epsilon_0\mu}} \tag{1.31}$$

which is independent of the collision energy. For polar molecules ($\mu_e \neq 0$), the charge–permanent-dipole interaction in general requires a quantum mechanical treatment of the molecular rotation. However, in the high-temperature limit, an approximate correction to k_L has been derived [52, 58] ("infinite order sudden approximation"), which reads

$$k'_L = k_L + \frac{\mu_e q}{4\pi\epsilon_0}\sqrt{\frac{\pi}{2\mu k_B T}}. \tag{1.32}$$

Here, the rate contribution from the permanent dipole moment decreases with increasing temperature T.

1.4.3 Adiabatic capture theory

To extend the capture model to a quantum mechanical description of molecular rotation, Clary and co-workers developed a rotationally-adiabatic capture (AC) model [56, 58]. In this model, the couplings between different rotational states induced by the charge–permanent-dipole interaction are treated quantum mechanically, similar to the calculation of the Stark energy shift in section 1.3.2. The relative translational motion between the collision partners is however still computed classically.

The Hamiltonian of the collision problem reads [58]

$$H = \frac{p_R^2}{2\mu} + H_{\text{rot}} + V_{\text{int}}(R,\beta) + \frac{\hbar^2\left(\boldsymbol{J}-\boldsymbol{j}\right)^2}{2\mu R^2} = \frac{p_R^2}{2\mu} + V_{\text{eff}} \tag{1.33}$$

The four terms are: the radial kinetic energy with radial momentum p_R, the field-free rotational Hamiltonian of the neutral molecule (equation (1.13)), the ion-molecule interaction potential (equation (1.28)), and the centrifugal correction with total angular momentum $\boldsymbol{J}$ of the collision partners and rotational angular momentum $\boldsymbol{j}$ of the neutral molecule. The asymptotic (initial) states of the scattering problem at $R \to \infty$ are denoted $|E_c, J, j_{K_aK_c}\Omega\rangle$ and correspond to a given collision energy $E_c = p_R^2/(2\mu)$, a total angular momentum J, and a field-free rotational state $|j_{K_aK_c}\Omega\rangle$ of the neutral molecule. Here, Ω denotes the projection of $\boldsymbol{j}$ onto the ion-molecule axis. The internal state of the ion is neglected in this treatment.

Within AC theory, the effective ion-molecule interaction V_{eff} is diagonalized in the $|J, j_{K_aK_c}\Omega\rangle$ basis for any fixed value of R. This yields rotationally-adiabatic and centrifugally corrected potential energy curves $V_{J,j_{K_aK_c}\Omega}(R)$, i.e. the eigenvalues of V_{eff} with asymptotic field-free rotational energy subtracted. The states $|J, j_{K_aK_c}\Omega\rangle$ asymptotically correspond to the field-free rotational quantum states.

Given these potential energy curves, AC theory assigns unit reaction probability to any collision with $J < J_{\max}$, for which the centrifugal energy barrier lies below the collision energy E_c. For each rotational state $|j_{K_aK_c}\Omega\rangle$, the corresponding value

$J_{\max}(E_c, j_{K_aK_c}, \Omega)$ is determined numerically. This gives a state-specific reaction cross-section [58]

$$\sigma(E_c, j_{K_aK_c}) = \frac{\pi\hbar^2}{2\mu E_c}\frac{1}{2j+1}\sum_{\Omega=-j}^{j}\left[J_{\max}(E_c, j_{K_aK_c}, \Omega)+1\right]^2. \tag{1.34}$$

which is averaged over all orientations of the molecule relative to the ion's electric field. The state-specific rate constant is then

$$\begin{aligned} k(E_c, j_{K_aK_c}) &= v_c\sigma(E_c, j_{K_aK_c}) \\ &= \frac{\pi\hbar^2}{\sqrt{2E_c\mu^3}}\frac{1}{2j+1}\sum_{\Omega=-j}^{j}\left[J_{\max}(E_c, j_{K_aK_c}, \Omega)+1\right]^2. \end{aligned} \tag{1.35}$$

When the molecule exhibits a thermal distribution of rotational states, averaged rate constants can be calculated using

$$k(E_c, T_{\rm rot}) = \sum_{j,K_a,K_c} p(T_{\rm rot}, j_{K_aK_c})\; k(E_c, j_{K_aK_c}). \tag{1.36}$$

Here, $p(T_{\rm rot}, j_{K_aK_c})$ is the thermal population of the asymptotic rotational state $|j_{K_aK_c}\rangle$ at the rotational temperature $T_{\rm rot}$, i.e.

$$p(T_{\rm rot}, j_{K_aK_c}) = Q^{-1}(2j+1)g_{\rm ns}e^{-E_{j_{K_aK_c}}/(k_BT_{\rm rot})}, \tag{1.37}$$

with nuclear-spin symmetry factor $g_{\rm ns}$, field-free rotational energies $E_{j_{K_aK_c}}$ (eigenvalues of $H_{\rm rot}$) and rotational partition function

$$Q = \sum_{j,K_a,K_c}(2j+1)g_{\rm ns}e^{-E_{j_{K_aK_c}}/(k_BT_{\rm rot})}. \tag{1.38}$$

The nuclear spin symmetry factor is important for molecules with equivalent indistinguishable nuclei. For water, with two equivalent hydrogen atoms giving rise to *para* and *ortho* nuclear spin isomers, the nuclear spin degeneracy factor is

$$g_{\rm ns,H_2O} = \begin{cases} 1, & K_a+K_c \text{ even (para)} \\ 3, & K_a+K_c \text{ odd (ortho)} \end{cases} \tag{1.39}$$

For DBB, the situation is more complicated. It has four hydrogen atoms and two bromine atoms that carry nuclear spin. Bromine exists in the form of two stable isotopes, ^{79}Br and ^{81}Br, with a natural abundance ratio of about 1:1, each having a nuclear spin of 3/2 [59]. Both *gauche* and *s-trans* conformers exhibit a C_2 symmetry axis only if the two bromine atoms are identical isotopes, otherwise all nuclei are distinguishable and $g_{\rm ns} = 1$. If the Br-atoms are identical, there are three pairs of identical indistinguishable nuclei: two pairs of H-atoms and the two Br-atoms. A pair of identical spins with nuclear spin i leads to $(2i+1)(i+1)$ symmetric states and $(2i+1)i$ antisymmetric states [18]. The numbers of symmetric and antisymmetric states for each group of equivalent nuclei ($H^{(1)}$, $H^{(2)}$ and Br) in DBB are shown in table 1.1. To evaluate the number of symmetric and antisymmetric states for the total nuclear spin wavefunction $\Psi_{\rm ns} = \Psi_{H^{(1)}}\Psi_{H^{(2)}}\Psi_{\rm Br}$,

one needs to form all possible combinations of the subgroups $H^{(1)}$, $H^{(2)}$ and Br. One thus arrives at a total of 136 symmetric and 120 antisymmetric nuclear spin states of DBB, which are given in the last line of table 1.1. These numbers are similar in magnitude due to the relatively large number of nuclei. To obey the Pauli principle, nuclear spin states must be paired with rotational states of opposite symmetry such that the overall molecular symmetry is antisymmetric.

For *s-trans*-DBB, the C_2 axis corresponds to the c inertial axis (see Fig. 1.6). Under a C_2 transformation, the state $j_{K_a K_c}$ changes its sign by $(-1)^{K_c}$ such that

$$g_{\mathrm{ns,s-trans-DBB}} = \begin{cases} 256 + 120, & K_c \text{ even} \\ 256 + 136, & K_c \text{ odd} \end{cases} \tag{1.40}$$

For *gauche*-DBB the C_2 axis is the b inertial axis (see Fig. 1.6) such that the state $j_{K_a K_c}$ transforms under C_2 with sign $(-1)^{K_a+K_c}$, like in water. Consequently,

$$g_{\mathrm{ns,gauche-DBB}} = \begin{cases} 256 + 120, & K_a + K_c \text{ even} \\ 256 + 136, & K_a + K_c \text{ odd} \end{cases} \tag{1.41}$$

In equations (1.40) and (1.41), a value 256 was added to account for the asymmetric form of DBB with two distinguishable Br isotopes, which occurs 50% of the time. The values of g_{ns} above only apply to the symmetric vibrational ground state of DBB. In an antisymmetric excited vibrational state, nuclear spin and rotational states of the same symmetry would have to be paired instead. Since the values of g_{ns} for symmetric/antisymmetric rotational states only differ by a few percent, $g_{\mathrm{ns}} \approx 1$ was approximated in all calculations for DBB. This reflects the fact that nuclear spin statistics only have a pronounced effect at low values of total nuclear spin, like for H_2O.

Table 1.1: Nuclear spin statistics of DBB.

atom	i	sym. states	anti-sym. states	total
$H^{(1)}$	$\frac{1}{2}$	3	1	4
$H^{(2)}$	$\frac{1}{2}$	3	1	4
Br	$\frac{3}{2}$	10	6	16
DBB		136	120	256

1.5 Thesis outline

In this chapter, the basic theoretical concepts needed for the understanding of this thesis were summarized. The remainder of this thesis is structured as follows:

Chapter 2 gives an overview of the experimental setup, including the ion trap and the molecular beam apparatus, as well as their characterization.

Chapter 3 reports measurements of the chemical kinetics between rotational-state-selected water molecules and trapped diazenylium ions. The measurements show that rotationally excited *ortho*-water has a lower rate constant than *para*-water in the absolute rotational ground state.

Chapter 4 presents a new experimental setup to generate coherent vacuum ultraviolet radiation at 118 nm. This light source was later used for soft single-photon ionization of organic molecules, in particular DBB and propene.

Chapter 5 demonstrates the spatial separation of the two *gauche* and *s-trans* conformers of DBB in a molecular beam.

Chapter 6 reports measurements of the reaction kinetics between conformer-selected DBB and trapped Ca^+ ions. It is found that the reaction rates are capture-limited for Ca^+ in its excited states. In the electronic ground state of Ca^+, however, an inhibition of the reaction with *gauche*-DBB is observed.

Chapter 7 describes the loading and sympathetic cooling of propene ions into a Ca^+ Coulomb crystal. Two methods are compared: VUV photoionization and charge transfer reaction with Ca^{2+} ions.

Chapter 8 reports measurements of the reaction kinetics of conformer-selected DBB with propene ions. In this $[4 + 1^+]$ polar cycloaddition, both conformers are found to exhibit capture-limited rate constants, which indicates efficient step-wise and concerted reaction mechanisms.

Chapter 9 gives an outlook on potential future work with the experimental setup and concludes this thesis.

2

Experimental Methods

This chapter gives an overview of the experimental setup used for reaction rate measurements of a conformer- or rotational-state-selected molecular beam with trapped ions.[1] Details on important experimental techniques and procedures are described, including loading of the ion trap, operation of the time-of-flight mass spectrometer (TOF-MS) and the molecular beam apparatus including electrostatic deflector. Selected characterisation and calibration measurements are presented.

2.1 Overview of the experimental setup

A schematic of the experimental setup [60] is shown in Fig. 2.1a. The setup combines a molecular beam apparatus [10] with a linear quadrupole ion trap (LQT) [17]. The LQT is radially coupled to a time-of-flight mass spectrometer (TOF-MS) [61] for quantitative analysis of ions extracted from the molecular beam after ionization or from the ion trap. In particular this enables a measurement of all reactant or product ions during an ion-molecule reaction [62, 63, 64, 65].

In the molecular beam apparatus, a dense and internally cold molecular beam is generated by pulsed supersonic expansion from a high-pressure reservoir through a cantilever piezo valve (MassSpecpecD ACPV2, 150 μm nozzle diameter) [66] into the source vacuum chamber. The molecular beam then passes through a series of skimmers to collimate the beam and select only its central part which is translationally cold. Afterwards, the beam passes through an electrostatic deflector[2] with a strong vertical electric field gradient to spatially deflect the molecules according to their effective dipole moments. After another skimmer, the molecular beam traverses a differential pumping tube and enters the main ultra-high vacuum (UHV) trap chamber of the experiment. This chamber hosts the LQT as well as the TOF-MS. The molecular beam is directed at the center of the LQT, located at a distance of about 90 cm from the valve. By vertically tilting the entire molecular beam apparatus relative to the main experiment chamber using an external tilt stage, the vertical deflection coordinate y at which the molecular beam passes through the ion

[1] The experimental apparatus was designed and built by D. Rösch as part of his Ph.D. thesis [60] with assistance of H. Gao.

[2] The molecular beam apparatus including electrostatic deflector was designed and built in the group of Prof. Dr. J. Küpper at the University of Hamburg.

trap can be adjusted. This allows different regions of the spatially dispersed molecular beam to be overlapped with the ion trap center, to perform reaction experiments with selected rotational states or conformers of the molecular beam and the trapped ions.

The LQT is operated using DC and RF electric fields as described in section 2.3. To load Calcium ions (Ca^+) into the LQT, an atomic beam of neutral Ca from a resistively heated Ca oven (Alvatec) is ionized using pulses from a focused femtosecond (fs) laser. For laser cooling of the trapped Ca^+ ions, two frequency-stabilised diode lasers at the $^2S_{1/2} \rightarrow {}^2P_{1/2}$ cooling transition (397 nm) and the $^2D_{3/2} \rightarrow {}^2P_{1/2}$ repumping transition (866 nm) of Ca^+ are directed at the trap. They are aligned along the symmetry axis of the LQT. The fluorescence of the resulting Ca^+ Coulomb crystals at 397 nm is imaged onto an electron-multiplier charge-coupled device (EMCCD) camera (Andor Luca), using a microscope with magnification of about 13. A leak valve (VACGEN LVM series) is installed on the trap chamber which allows one to introduce gas into the trap chamber in a controlled way. This was used to initiate chemical reactions with trapped ions or to generate molecular ions in the trap by photoionization.

To analyze the ions in the LQT or ions directly generated from the molecular beam using photoionization, they can be ejected into a TOF-MS that is radially coupled to the LQT in the direction of gravity. The TOF-MS consists of five electrodes as shown in Fig. 2.1b. A micro-channel plate (MCP) detector (Photonis APD 2 APTOF) operating

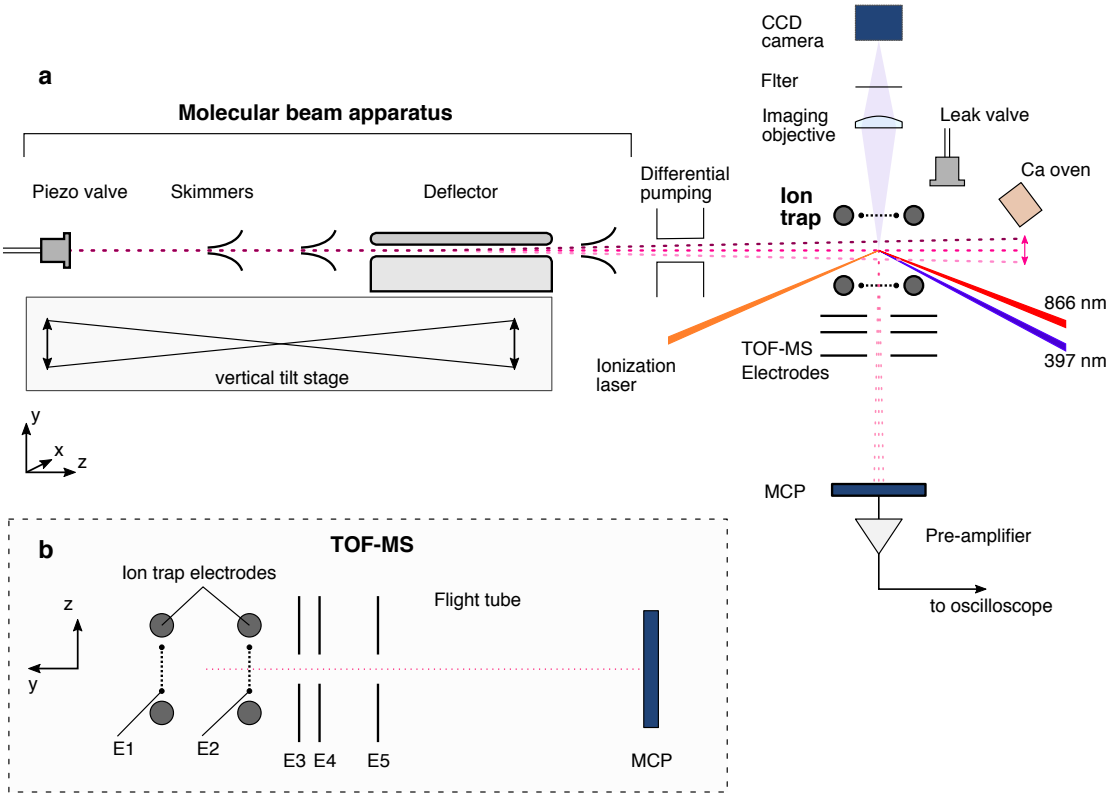

Figure 2.1: **Overview of the experimental setup. a**, schematic setup including molecular beam apparatus, LQT and TOF-MS. **b**, details of the TOF-MS.

at a typical voltage of 2.1 to 2.3 kV was placed at the end of the flight tube. The TOF-MS LQT can be operated in different modes [61]. In low-resolution mode, a single high-voltage pulse is applied to the repeller electrode E1 and all other electrodes are grounded. This enables the measurement of TOF mass spectra over a wide mass range. Alternatively, a second high-voltage pulse can be applied to the extractor electrodes E3 and E4 after a short (< 1 μs) delay relative to the first pulse. This enables high mass resolution ($m/\Delta m \approx 700$) in a narrow selected mass range [61]. The distance from LQT center to the MCP is 64.8 cm and the length of the flight tube is about 60 cm. The MCP signals were amplified using a pre-amplifier (home-built or FEMTO HPCA amplifiers) and acquired on an oscilloscope (LeCroy Wavesurfer 64 MXs).

A pulse generator (Quantum Composer 9520 series) was used to synchronise the photoionization laser pulses, the high-voltage pulses applied to the TOF-MS, the molecular beam pulses and the data acquisition.

To achieve high vacuum, the source chamber is evacuated using two turbomolecular pumps to maintain a pressure of $\sim 10^{-6}$ mbar with continuous operation of the piezo valve. In the trap chamber, several turbomolecular pumps as well as non-evaporative getters (NEG) and a titanium sublimation pump are used to reach a base pressure of $\sim 2 \times 10^{-10}$ mbar. During operation of the molecular beam, the pressure increases to $\sim 5 \times 10^{-9}$ mbar.

2.2 Laser system

The experiment relies on a number of laser sources for laser-cooling of Ca^+ and various photoionization schemes.

Diode lasers For laser cooling and repumping of Ca^+, two continuous-wave grating-stabilized diode lasers at 397 nm (Toptica) and 866 nm (home-built), respectively, are used. They are frequency-stabilized using a wavemeter (High Finesse WSU 30) and a computer controlled feedback loop. The wavemeter is calibrated automatically using an external HeNe laser. In locked mode, the residual frequency fluctuations amount to about 5 MHz for the 397 nm laser and 10 MHz for the 866 nm laser. The two laser output beams are coupled into single-mode optical fibers and delivered to the optical breadboard of the main experiment. There, both laser beams are collimated and combined on a dichroic mirror before they are sent through the symmetry axis of the LQT, focused to $1/e^2$ beam waists of 0.4 mm for the 397 nm beam and 0.2 mm for the 866 nm beam. The optical powers are adjusted using variable neutral density filters to 1 mW at 397 nm and 0.5 mW at 866 nm.

Pulsed Nd:YAG laser A pulsed and frequency-tripled Nd:YAG laser (Quantel Brilliant) at 355 nm was employed for multi-photon ionisation of Ca and and generation of vacuum-ultraviolet radiation at 118 nm by non-resonant third-harmonic generation in a Xe:Ar mixture (see chapter 4). The laser has a pulse duration of 5 ns at a repetition rate of 10 Hz and a maximum pulse energy of 30 mJ.

Pulsed dye laser For resonance-enhanced multi-photon ionization (REMPI) of water, a pulsed and tunable dye laser (Radiant Dyes, Coumarin-307) was used. The dye laser was pumped by a frequency-tripled Nd:YAG laser (INNOLAS Spitlight, 355 nm, repetition rate 10 Hz, pulse length 10 ns). After a frequency doubling stage, tunable laser light at 248 nm was obtained. The laser pulses with a pulse energy of 1.5 mJ were focused into the molecular beam using a lens with focal length of 300 mm.

Femtosecond laser A mode-locked Ti:Sapphire femtosecond (fs) laser (CPA 2110, Clark-MXR, Inc.) at a wavelength of 775 nm provided laser pulses with duration of 150 fs at and pulse energy of up to 1 mJ. The repetition rate was varied between 20 Hz and 100 Hz depending on the application. The fs laser was used for ionization of Ca and the molecular beam, e.g. to measure molecular beam density profiles. When focused to a beam diameter of 30–50 μm at the sample, peak intensities on the order of 10^{14} W/cm^2 were reached. This allowed strong-field multi-photon ionization [67].

2.3 Ion trap with integrated time-of-flight mass spectrometer

2.3.1 Trap setup

A photograph of the LQT used in the experiments is shown in Fig. 2.2. The photograph shows the different trap electrodes and the applied RF and DC voltages are indicated according to the scheme presented in section 1.2. The LQT was operated at a peak-to-peak RF voltage of $2V_0 = 800$ V and a RF frequency of $\Omega_{\mathrm{RF}} = 2\pi \times 3.304$ MHz. DC voltages of about 5 V were applied to the end caps. A commercial high-voltage RF generator (Stahl-Electronics HF-DR 3.5-900 FL) was used. The photograph also shows an alignment fiber mounted on a translation stage, which can be moved to the center of the ion trap in order to align laser beams by maximizing the light scattered to the camera. Moreover, the repeller electrode E1 for the TOF-MS is shown (compare Fig. 2.1b). It is a nickel mesh (Precision Eforming) with 90% transmission that is positioned between the upper trap electrode rods. A second equivalent mesh electrode (E2) is located between the lower trap electrode rods. E1 and E2 are called top and bottom mesh, respectively.

2.3.2 Coulomb crystal loading procedure

To load a Ca^+ Coulomb crystal of standard size ($\sim$ 1000 ions) into the ion trap, the following procedure was used. Neutral Ca vapour from the oven was ionized using pulses from the fs laser focused to a diameter of $\approx$ 30 μm and the resulting Ca^+ ions were subsequently laser cooled. To avoid excessive double ionization of Ca^+ to Ca^{2+}, the fs laser focus was moved slightly away from the ion trap center. The 397 nm cooling laser was tuned to a red detuning of $\Delta_{397} \approx -2\Gamma_{397} = -42$ MHz ($\approx$ 20 fm) from the $^2S_{1/2} \rightarrow ^2P_{1/2}$ transition. The resonance condition $\Delta_{397} = 0$ is marked by the point where a Coulomb crystal "melts" due to the vanishing laser cooling efficiency on resonance and laser-induced heating for blue detuning $\Delta_{397} > 0$ [68]. After a defined crystal size was achieved, as observed on the camera, the Ca oven heating as well as the fs laser were switched off. The resulting crystal was cleaned by slowly ramping down the trap RF voltage to 36% of its initial value, and back. This removed impurity ions with mass

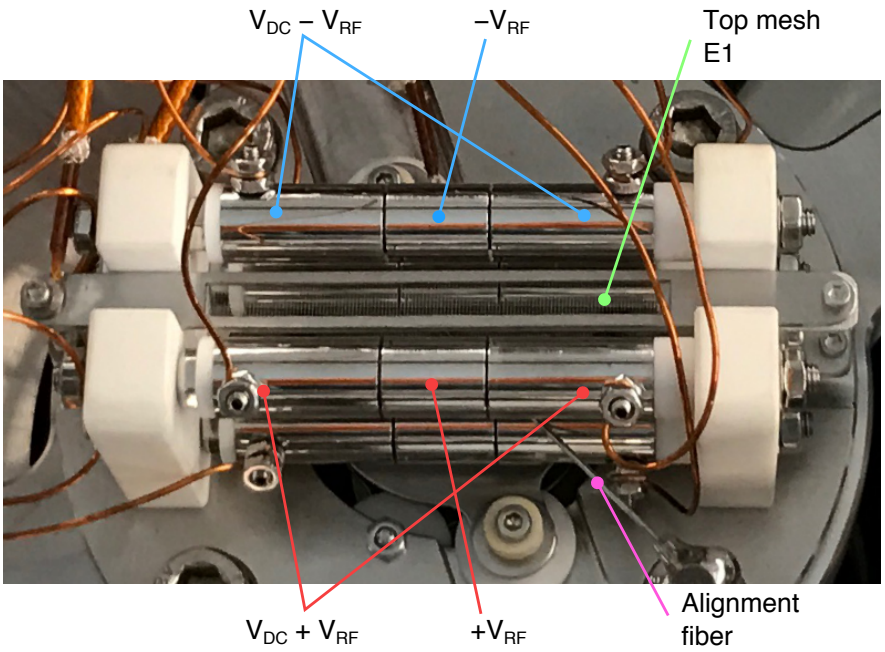

Figure 2.2: **Photograph of the LQT.** Electrodes and applied voltages are indicated.

larger than 40 u that resulted from reactive collisions of Ca^+ with residual background gases of the vacuum chamber (e.g. H_2O, O_2, N_2, H_2 or previously leaked gas). A cleaned Ca^+ crystal is shown in Fig. 1.4c. The constant size and composition of the ion Coulomb crystals was verified by TOF-MS.

For sympathetic cooling of molecular ions, the corresponding neutral gas is leaked into the trap chamber using the leak valve and ionized for a defined period of time via either fs laser pulses (see section 3 for N_2^+) or VUV radiation (see section 7 for $C_3H_6^+$).

2.3.3 Ion micromotion

The velocities of Coulomb-crystallized ions in RF traps are usually dominated by their micromotion, i.e., their fast motion driven by the RF fields [17]. The contribution of their secular motion can be neglected because of laser and sympathetic cooling. The spread of micromotion velocities across the crystal thus defines the velocity spread δv of the entire ion ensemble. This affects the collision velocity distribution of reactive collisions with the molecular beam (cf. chapter 3). The micromotion velocities scale with the radial position of the ions in the trap [69]. They are zero for ions located in the trap centre and maximal for the outermost ions of the crystal. For ions lighter than Ca^+, which accumulate at the trap center, the radial extension r can directly be determined from the edges of the non-fluorescing central region of the crystal images taken during the measurements. For N_2H^+ ions loaded in a Ca^+ crystal see inset in Fig. 3.1 of chapter 3. Using the analytical expressions of the ion trajectories in a quadrupole trap [69], the root-mean-square velocity for the outermost ions in the present N_2H^+ crystals at $r = 200$ μm was estimated to be $v_{\mathrm{rms}} = 163$ m/s. The corresponding micromotion energy was found

to be $E_{\mathrm{kin}} = k_B \times 47$ K.

2.3.4 Time-of-flight mass-spectrometer

The TOF-MS used in this work has been described in detail in refs. [61, 60].

Principle of TOF-MS The geometry of the TOF-MS is depicted in Fig. 2.1b. Ions are generated at the center of the ion trap using photoionization and a high voltage pulse applied to repeller electrode E1 accelerates them towards the MCP. The other electrodes E2 – E5 are grounded. When the ions arrive at the field-free flight tube at E5, they have acquired a kinetic energy that equals the potential energy drop qU_0 between their initial position and the entrance of the flight tube. The ion charge $q = ze$ is an integer multiple ($z \in \mathbb{N}$) of the elementary charge e. Hence, the velocity of an ion with mass m and charge q is given by

$$v = \sqrt{\frac{2qU_0}{m}} \tag{2.1}$$

Thus, the time of flight (TOF) t required to traverse the flight tube of length ℓ is given by

$$t = \frac{\ell}{v} = \sqrt{\frac{m}{z}} \frac{\ell}{\sqrt{2eU_0}} \tag{2.2}$$

It is proportional to the square-root of the mass/charge ratio m/z. Consequently, the measured TOF can be mapped onto m/z. In practice, the ion peaks appear at the arrival times $t' = t + t_0$ with an arbitrary offset t_0, e.g. due to the time of initial acceleration from the ion trap to the flight tube entrance. Calibration of m/z can be done by fitting the m/z values of known ion peaks to their respective arrival times t' using the relationship $m/z = a(t' - t_0)^2$. The fit parameters are the slope $a = 2eU_0/\ell^2$ and the time offset t_0. This fit requires knowledge of the m/z values of at least two ion peaks in the measurement. Convenient ion species for TOF-MS calibration are Ca^+, Ca^{2+} for TOF-MS of Coulomb crystals or the carrier and seed gases for molecular beams.

TOF-MS with ions from molecular beam For measurement of molecular beam profiles and deflection profile measurements the ions were generated by photoionization at the center of the ion trap. To enable a better ion selection in the TOF-MS, a voltage of 500 V was applied to the four end caps of the trap. For extraction of the ionized species, a permanent voltage of 4.0 kV was applied to the repeller electrode.

TOF-MS of trapped ions Two different modes of operation were used for the TOF-MS. For the determination of mass spectra of the reaction products in a wide mass range, a low-resolution mode was used to extract ions into the TOF-MS. First, the RF trapping fields were switched off within one RF cycle. After a delay of 0.1 μs, a 1 μs long pulse of 4.0 kV was applied to the repeller electrode E1, while all other electrodes were grounded. Fast high-voltage switches (Behlke HTS 61-01-HB-C, rise time 70 ns) were used to apply high-voltage pulses to the TOF-MS electrodes.

In order to measure high-resolution TOF mass spectra, additional 1 μs long high-voltage pulses of 4.0 kV and 3.2 kV, were applied to the extractor electrodes E3 and

E4, respectively [61]. These were delayed by 0.45 μs relative to the pulse on E1. For a narrow mass range, this focuses ions of different initial positions onto the MCP detector such that they arrive at the same time. In this way, the mass resolution was selectively enhanced for the Ca^+ and $C_4H_n^+$ species in the measurements presented in chapters 6 and 8.

2.3.5 Molecular dynamics simulations of Coulomb crystal TOF-MS

In an ion Coulomb crystal, ions spatially arrange according to their mass/charge ratio (cf. section 1.2.2). While light ions accumulate at the centre, heavy ions form rings around the lighter ions (Fig. 2.3a). The heavier the species, the further away from the crystal centre the ions localise thus forming an onion-like arrangement of ions around the core [17]. In the present reaction experiments (cf. chapter 6 and 8), the core is formed by the laser-cooled Ca^+ ions.

The shell-like ion arrangements strongly affect the ion dynamics during ejection into the TOF-MS flight tube and lead to a dispersion of the ion-velocities depending on their initial position in the ring. The extended ion packets impinging on the detector give rise to bimodal distributions in the TOF spectrum with peaks at two distinct arrival times [61]. The widths of the bimodal TOF signals strongly depend on the amount of lighter ions in the original Coulomb crystals which determine the diameter of the shells of heavier ions.

This effect has to be taken into account when analyzing TOF mass spectra of mixed species Coulomb crystals. In order to predict and accurately assign the signals appearing in the mass spectra measured in chapters 6 and 8, molecular dynamics (MD) simulations of mixed species Coulomb crystals ejected into the TOF-MS were performed using the software SIMION [70].[3] In the simulations, ion trajectories of a Coulomb crystal being ejected into the TOF-MS were calculated and the arrival times at the detector were extracted to determine the mass spectra.

To illustrate the effect of Coulomb crystal size on the shape of the TOF-MS signal, Coulomb crystals composed of two ion species were simulated. The mass of the first species was set to 40 u (Ca^+) and the mass of the other to 92 u. In the MD simulation, the number of ions with mass 92 u was fixed to 100 and the number of ions of mass 40 u was varied between 100 and 500. Simulated TOF mass spectra of these crystals are presented in Fig. 2.3b. While the lighter species produces a single TOF peak, the heavier ions show a bimodal distribution the width of which increases with increasing number of light ions.

2.3.6 Calibration of the TOF-MS sensitivity

To calibrate the absolute sensitivity of the TOF-MS, the TOF-MS signals generated by Coulomb crystals of a well-defined ion number were measured [71]. Fig. 2.4a shows fluorescence images of Ca^+ ion strings with a number of two to five ions. Counting the number of ions in each image was facilitated by integrating the fluorescence in the images along the vertical axis. The corresponding plots are shown below each of the fluorescence images with the red line indicating a moving average over 11 pixels. Fig. 2.4b shows

[3] L. Xu performed the SIMION simulation and kindly provided the data.

the correlation between the counted ion number and the total integrated fluorescence counts for a selection of 28 Coulomb crystal images with up to 9 ions. Fitting the data with a linear function gives a slope of 0.58(4) counts per ion. This relation enabled the determination of the number of ions given the integrated fluorescence of any Ca^+ Coulomb crystal. For a larger set of Coulomb crystals, both fluorescence images as well as TOF-MS data was acquired. Fig. 2.4c shows the integrated Ca^+ TOF-MS signal as a function of ion number (determined from fluorescence counts). In this measurement, a FEMTO HPCA pre-amplifier with a gain of 10^3 V/A was used. Fitting these data with a linear function gives a TOF-MS sensivity of 0.133(12) Vns/ion, where the uncertainty also includes the uncertainty in the relation between ion number and fluorescence counts.

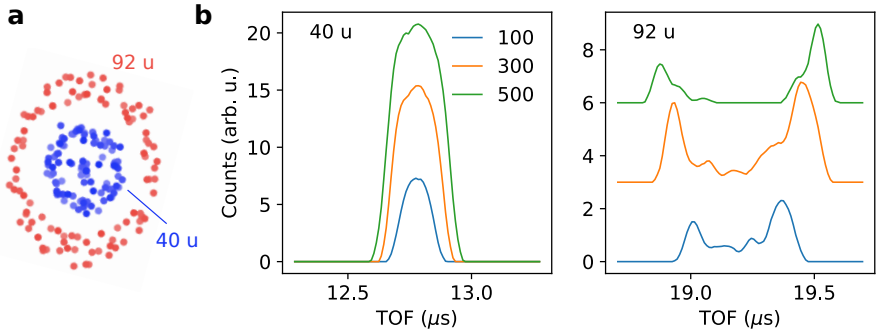

Figure 2.3: **Influence of Coulomb-crystal size on ion time-of-flight**. **a**, Simulated Coulomb crystal consisting of ions with mass of 40 u (blue) and mass 92 u (red). **b**, Simulated TOF mass spectra for Coulomb crystals consisting of a variable number (100, 300, 500) of ions with mass 40 u and 100 ions of mass 92 u. With increasing number of lighter ions, the width of the bimodal time-of-flight distribution for the ions with mass 92 u increases. TOF traces for the species at mass 92 u are vertically offset for clarity.

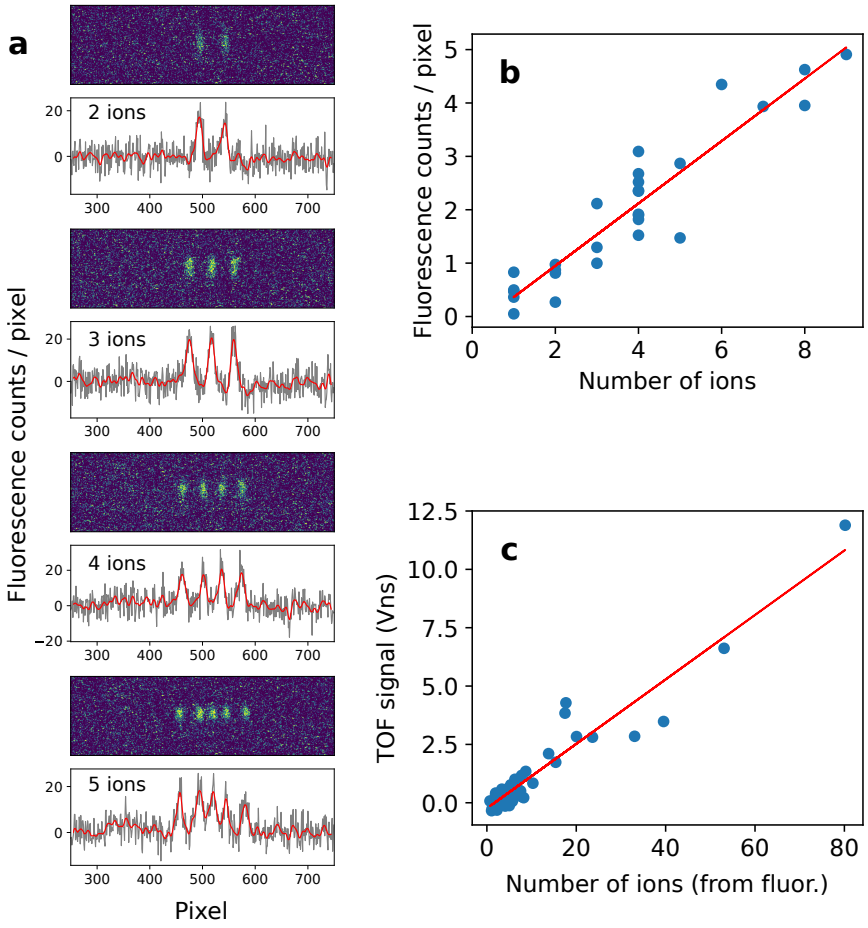

Figure 2.4: **Calibration of the TOF-MS sensitivity.** **a**, Fluorescence images of Ca^+ Coulomb crystals with 2 to 5 ions (top to bottom). Below each image, the fluorescence integrated along the vertical axis is shown. The red line is a moving average. **b**, integrated Ca^+ fluorescence counts as a function ion number with linear fit (red line). **c**, integrated Ca^+ TOF-MS signal as a function of ion number (determined from measured fluorescence counts using the fit in **b**) with linear fit (red line).

2.4 Controlled molecular beam apparatus

2.4.1 Experimental setup

Photographs of the cantilever piezo valve and the electrostatic deflector, including skimmers, are shown in Figs. 2.5a and b, respectively. The electrostatic deflector consists of a pair of 15.4 cm long electrodes separated by 1.4 mm [72]. COMSOL Simulations [73] of the electric field strength $\mathcal{E}$ and vertical gradient $\partial\mathcal{E}/\partial y$ for a deflector voltage of 15 kV applied to the deflector rod electrode and 0 kV to the trough electrode are displayed in Figs. 2.5c and d, respectively. The cross marks the position of the molecular beam propagation axis. Due to symmetry the orthogonal gradient $\partial\mathcal{E}/\partial x$ vanishes there. These simulated deflector fields are used for the calculation of molecular trajectories through the entire beam apparatus [6], by numerically integrating the differential equation (1.14) (see below).

Alignment of the molecular beam apparatus is achieved with the vacuum system under air. A laser beam is sent from reverse through the skimmers and allows the valve to be positioned in its center. Concentric rings around the laser beam are observed when the alignment is optimal. The valve is mounted on a three-dimensional translation stage

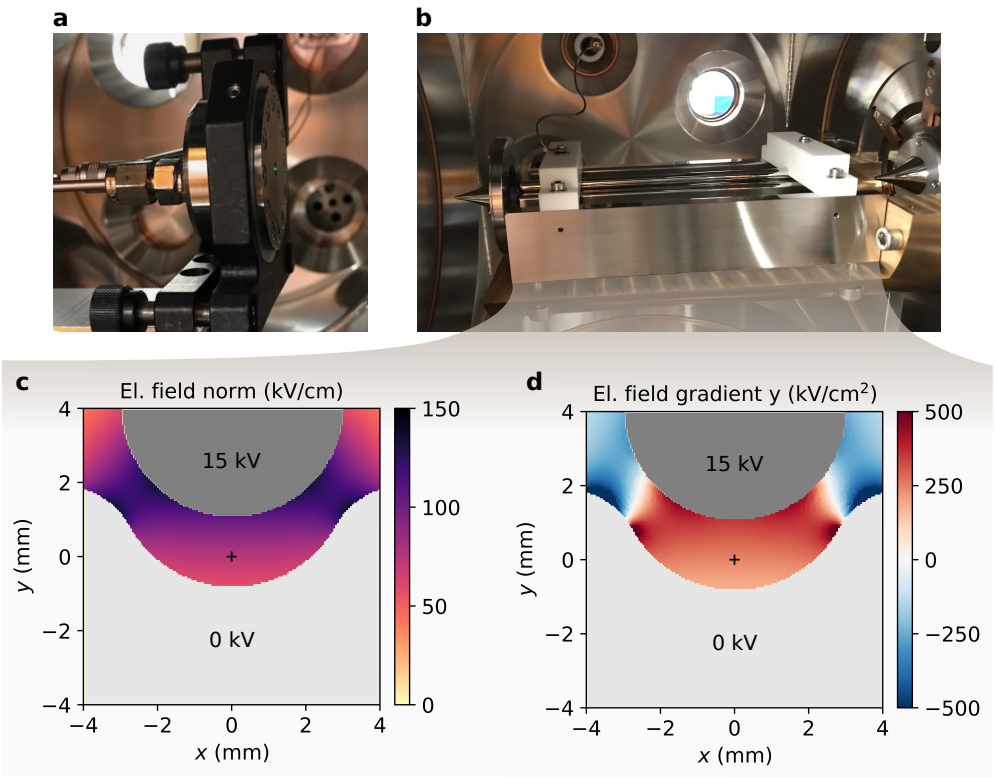

Figure 2.5: **Molecular beam apparatus.** **a**, Photograph of the piezo valve. **b**, Photograph of the electrostatic deflector and skimmers placed before and after the deflector. **c, d**, Simulated field strength and vertical gradient in the electrostatic deflector, respectively.

to optimize the alignment of the molecular beam relative to the skimmer apertures. Longitudinal translation of the valve is also used to measure the beam velocity (see below).

2.4.2 Monte-Carlo trajectory simulations for electrostatic deflection of water

Effective dipole moments and Stark energies of the individual rotational states of water were calculated using the CMIstark software package [49]. Figures 2.6a and c show simulated Stark energies and effective dipole moments, respectively, for the ground states of both isomers. All Stark components are high-field seeking with negative Stark shifts. The $|j_{K_aK_c}|M|\rangle = |1_{01}1\rangle$ state has the largest dipole moment resulting in the largest deflection in an electric field gradient, while $|1_{01}0\rangle$ shows the smallest Stark shift. Here, M denotes the quantum number of the space-fixed projection of $\vec{j}$. This results in a separation of the *ortho*-water $|M| = 0, 1$ states under electrostatic deflection. The value of the dipole moment of *para*-water in the $|0_{00}0\rangle$ state is in between those of *ortho*-water. Additionally, calculations of the Stark energies and dipole moments for the excited rotational states $|1_{10}\rangle$ and $|1_{11}\rangle$ are presented in Figures 2.6b and d. Their contribution to the measured deflection profiles is discussed in Appendix A.1.

The state-specific deflection profiles of the molecular beam traveling through the entire setup including deflector have been simulated using a home-made software package based on CMIfly [6]. The trajectory simulations were carried out with 10^6 water molecules

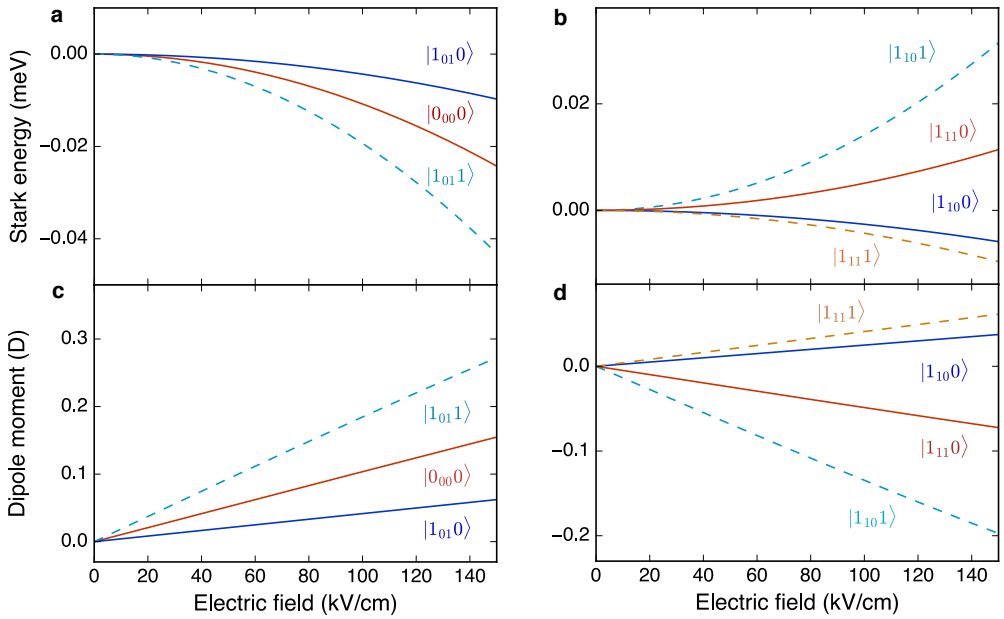

Figure 2.6: **Stark shift calculation for water.** Calculated stark energy shifts (**a**) and effective dipole moments (**c**) for the ground rotational states of *ortho*-($|j_{K_aK_c}|M|\rangle = |1_{01}0\rangle, |1_{01}1\rangle$) and *para*- ($|0_{00}0\rangle$) water as a function of the electric-field strength. **b, d** Stark shifts and effective dipole moments, respectively, for the higher excited rotational states $|1_{10}0\rangle, |1_{10}1\rangle$ and $|1_{11}0\rangle, |1_{11}1\rangle$.

per quantum state. Their initial positions were uniformly sampled across the nozzle cross section. Their initial velocities were sampled from a normal distribution with a mean longitudinal velocity of 575 m/s and standard deviations of 10 m/s in the transverse directions and 69 m/s in the longitudinal direction. An *ortho:para* ratio of 3:1 was imposed on the molecular beam set by the nuclear-spin statistics. For each quantum state, simulated deflection profiles were obtained from histograms of the coordinates of the molecules upon arrival in the reaction region. Thermally averaged deflection profiles $n_{\sigma,T}(y)$ ($\sigma \in \{o, p\}$) for each spin isomer at rotational temperature T were calculated from the deflection profiles of the individual quantum states $n_{jK_aK_cM}(y)$ using the expression

$$n_{\sigma,T}(y) = \frac{g_\sigma}{Q_\sigma} \sum_{j,K_a,K_c} \sum_{|M|=0}^{j} g_M g_{\sigma,K_aK_c} e^{-E_{jK_aK_c}/k_BT}\, n_{jK_aK_cM}(y), \tag{2.3}$$

with the rotational partition function

$$Q_\sigma = \sum_{j,K_a,K_c} \sum_{|M|=0}^{j} g_M g_{\sigma,K_aK_c} e^{-E_{jK_aK_c}/k_BT}. \tag{2.4}$$

Here, k_B denotes the Boltzmann constant and $E_{jK_aK_c}$ are the field-free rotational energies. The degeneracy factor g_M takes values $g_M = 1$ for $M = 0$ and $g_M = 2$ for $|M| > 0$. The nuclear-spin symmetry factors g_{σ,K_aK_c} are defined by

$$g_{\mathrm{o},K_aK_c} = \begin{cases} 1 & K_a + K_c \text{ odd} \\ 0 & K_a + K_c \text{ even} \end{cases} \tag{2.5}$$

for the *ortho*- and

$$g_{\mathrm{p},K_aK_c} = \begin{cases} 0 & K_a + K_c \text{ odd} \\ 1 & K_a + K_c \text{ even} \end{cases} \tag{2.6}$$

for the *para*-isomer. The nuclear-spin degeneracy factors are $g_\mathrm{p} = 1/4$ and $g_\mathrm{o} = 3/4$. The total thermal deflection profile was calculated from the sum of the deflection profiles of the *ortho*- and *para*-isomers,

$$n_{\mathrm{tot,T}}(y) = n_{\mathrm{para},T}(y) + n_{\mathrm{ortho},T}(y). \tag{2.7}$$

Results of the state-specific deflection profiles obtained from the Monte Carlo simulation are shown in Fig. 2.7. There, the beam profile at 0 kV (no deflection) is shown together with the deflection profiles of the rotational ground states of *para*- and *ortho*-water at a deflector voltage of 15 kV. In accordance with the calculated Stark energy curves (Fig. 2.6), the *ortho* ground state 1_{01} contains a strongly deflected $|M| = 1$ component and a weakly deflected $M = 0$ component. The *para* water ground state 0_{00} shows intermediate deflection.

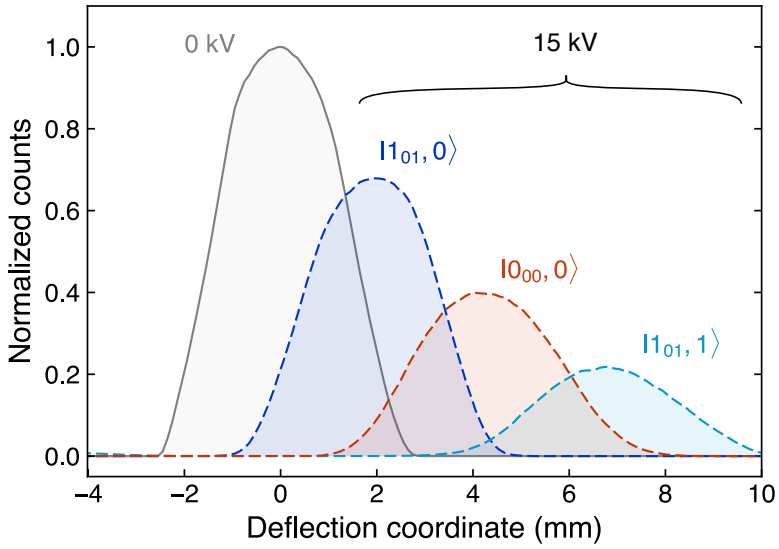

Figure 2.7: **Monte Carlo simulation of the deflection profile of water.** The grey curve shows the undeflected beam profile at a deflector voltage of 0 kV. Deflection profiles for a deflector voltage of 15 kV are shown for the *para* ground state $|0_{00}0\rangle$ (red) and the *ortho* ground states $|1_{01}0\rangle$ (dark blue) and $|1_{01}1\rangle$ (light blue).

2.4.3 Molecular beam of water

2.4.3.1 Beam velocity

The molecular beam was generated from water vapour at room temperature and seeded in argon carrier gas at 3 bar. The gas mixture was pulsed through the cantilever piezo valve at a repetition rate of 200 Hz and an electric pulse width of 30 μs.

The velocity of the molecular beam was determined by probing its time-resolved density profile in the ion-trap region at different longitudinal positions of the gas valve (Fig. 2.8a). The delay of the molecular beam center for each valve position was determined from a Gaussian fit to the beam profiles. By fitting the linear relation between valve position and the delay of the beam center (Fig. 2.8b), the velocity of the molecular beam was determined to be $v_{beam} = 575(50)$ m/s. This beam velocity was used for adiabatic-capture rate calculations and Monte Carlo trajectory simulations.

The velocity spread $\delta v_{beam} = 65(36)$ m/s of the beam was determined from the half-width-at-half-maximum δt (HWHM) of the temporal profiles of the gas pulses, which was assumed to be limited by the longitudinal velocity distribution of the molecules. The distance of the molecular beam propagation is $\ell = 0.9$ m from the nozzle to the ion trap. The time-of-flight for velocity v is thus given by $t = \ell/v$. For a given velocity spread δv, this results in a temporal spread of

$$\delta t = \frac{\ell}{v} - \frac{\ell}{v + \delta v} \approx \frac{\ell \delta v}{v^2} \tag{2.8}$$

Consequently, one can calculate the velocity spread from the HWHM δt using $\delta v = v^2 \delta t / \ell$.

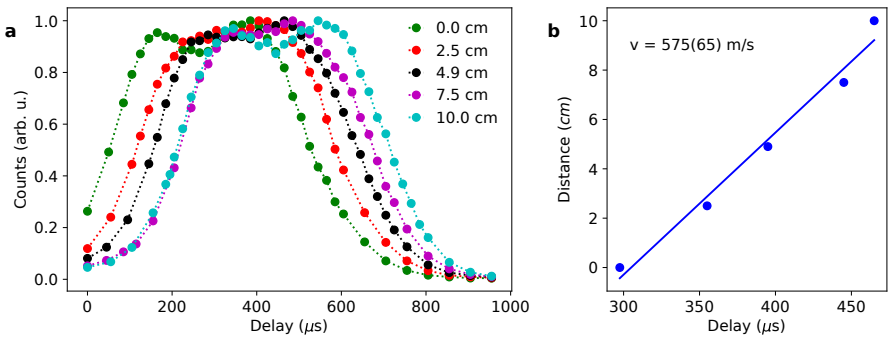

Figure 2.8: **Measurement of the beam velocity.** **a**, longitudinal beam profile measurement obtained by scanning the delay between valve pulse and fs laser pulse. This uses the argon signal. The longitudinal position of the valve is varied as indicated in the legend. **b**, plot of the valve position against the delay for which the peak molecular beam signal was observed. The line is a linear fit which gives the beam velocity.

2.4.3.2 REMPI spectroscopy of water

To determine the rotational state populations of water in the molecular beam, state-selective (2+1)-resonance-enhanced multiphoton-ionization (REMPI) via the $\tilde{C}$ electronic state of water was employed [74]. In (2+1)-REMPI, the H_2O molecules are excited to a selected intermediate rovibronic state via two-photon absorption (Fig. 2.9a). From there, the absorption of a third photon leads to ionization. Since the two-photon resonance must be met, REMPI allows sensitive rotational-state resolved ionization.

In order to determine the rotational temperature of the undeflected water beam, a (2+1) REMPI spectrum was recorded by monitoring the ion signal detected at mass-to-charge ratio $m/z = 18$ u in the TOF-MS as a function of the UV laser wavelength (Fig. 2.9b). The experimental spectrum was compared to a simulation using the software package PGOPHER [75]. Best agreement was found by assuming a rotational temperature of 7 K in line with previous studies [74, 15]. Two dominant transitions were identified, the $|j_{K_a K_c}\rangle = |2_{20}\rangle \leftarrow |1_{01}\rangle$ transition of *ortho*-water at 80724 cm^{-1} and the $|2_{21}\rangle \leftarrow |0_{00}\rangle$ transition of *para*-water at 80747 cm^{-1}. j, K_a, K_c denote the rotational quantum numbers of an asymmetric top. The experimental intensities of the lines, i.e., the areas A underneath the peaks, were determined from fits of a sum of two Lorentz functions to the spectral features.

The relative line strengths S_o and S_p of the two transitions for *ortho*- and *para*-water, respectively, were estimated from the relevant peak areas A_o and A_p. Assuming that both nuclear-spin isomers were cooled down to their relevant ground states and that the *ortho:para* ratio of 3:1 prevalent in the water vapour prior to expansion was conserved

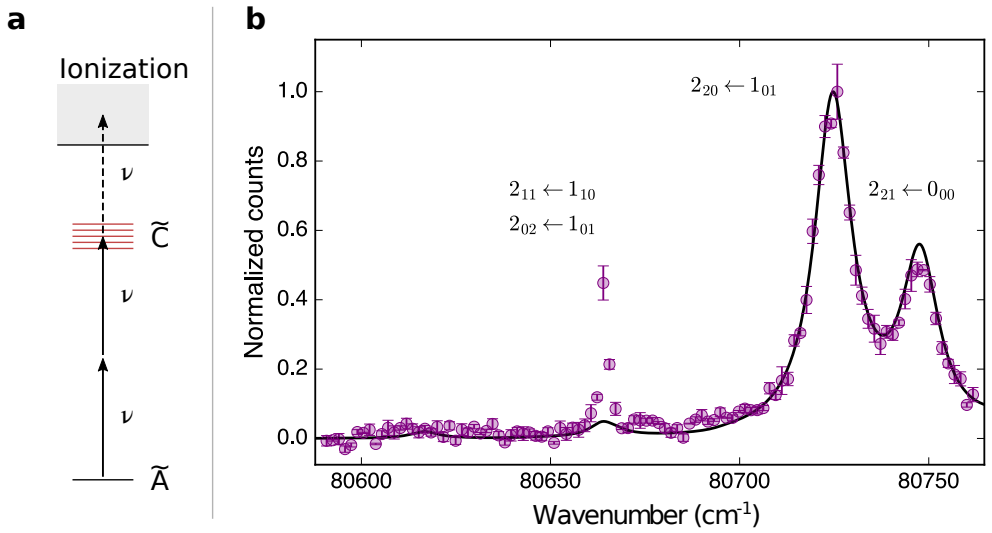

Figure 2.9: **REMPI spectroscopy of water.** **a**, schematic of (2+1) REMPI. **b**, measured (2+1) REMPI spectrum (data points) of a beam of water seeded in argon at a backing pressure of 3 bar and a simulation of the spectrum (line) at a rotational temperature of 7 K. Uncertainties correspond to one standard error.

in the molecular beam, it holds that

$$3 = \frac{A_\mathrm{o} S_\mathrm{p}}{A_\mathrm{p} S_\mathrm{o}}. \tag{2.9}$$

With $S_\mathrm{o} = 1$, $S_\mathrm{p} = 1.51(1)$ was obtained.

In the deflected water molecular beam (cf. chapter 3), REMPI spectroscopy was used to determine the populations p_o and p_p of the *ortho* and *para* isomers, respectively. From the fitted peak areas A_σ of the REMPI spectrum at a given deflection coordinate, the population of the isomer $\sigma \in \{o, p\}$ was calculated using

$$p_\sigma = \frac{A_\sigma / S_\sigma}{A_\mathrm{p}/S_\mathrm{p} + A_\mathrm{o}/S_\mathrm{o}}. \tag{2.10}$$

2.4.3.3 Composition of the molecular beam

Mass spectra of the molecular beam recorded after fs-laser ionization indicate the presence of water clusters in the supersonic expansion (Fig. 2.10). To minimize the amount of clusters formed by condensation of water molecules within the expansion region of the molecular beam, argon carrier gas has been chosen. For the heavier carrier gas krypton with a slower beam velocity, much stronger formation of water clusters was observed. For comparison, Fig. 2.11 shows a TOF-MS of a molecular beam of krypton seeded with water. Due to the low-velocity expansion, very strong cluster signals of water $(H_2O)_nH^+$ with n up to 16 are observed. Only peaks up to $n = 8$ are indicated in the figure.

The fs laser is able to ionize these clusters through strong-field ionization and break them into fragments including H_2O^+. The signal of these H_2O^+ cluster-fragment ions contributes to the $m/z = 18$ u signal of the water monomer ions in the mass spectra. This additional signal needs to be taken into account when evaluating the measured deflection profiles of water. Fig. 2.12 shows that cluster fragments with mass $m/z > 18$ u experience no significant deflection at a deflector voltage of 15 kV. It is therefore assumed that the detectable water clusters present in the molecular beam are largely undeflected and that the signal recorded at large deflection coordinates for $m/z = 18$ u is solely due to the water monomer. Thus, to avoid interference from reactions of the N_2H^+ ions with the clusters, the reaction rate measurements of chapter 3 were conducted at beam positions outside the region of deflection coordinates where undeflected water clusters would contribute to the rate measurements. These beam positions are labelled I–III in Fig. 2.12.

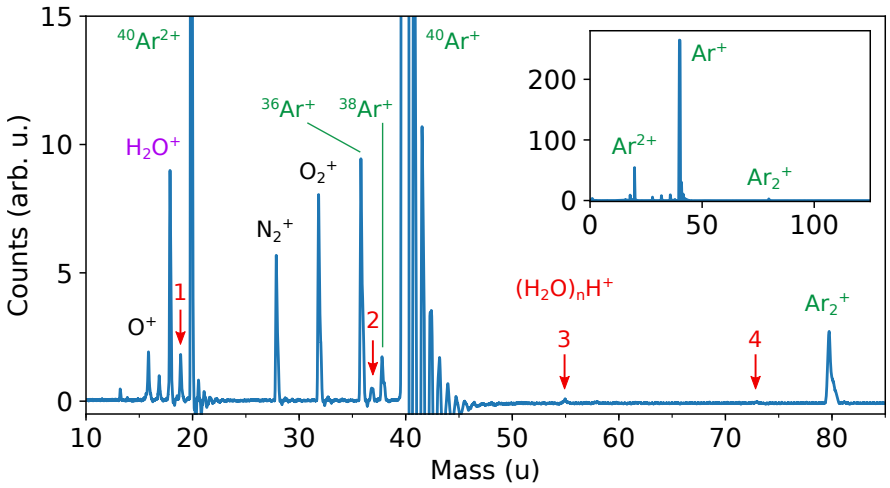

Figure 2.10: **TOF-MS of a molecular beam of water seeded in argon.**. This spectrum was measured at a deflector voltage of 15 kV and at deflection coordinate $y = 0.6$ mm. Weak signals of water clusters $(H_2O)_n^+$ with n up to 4 are observed. The remaining peaks are mostly due to Ar isotopes and residual gases.

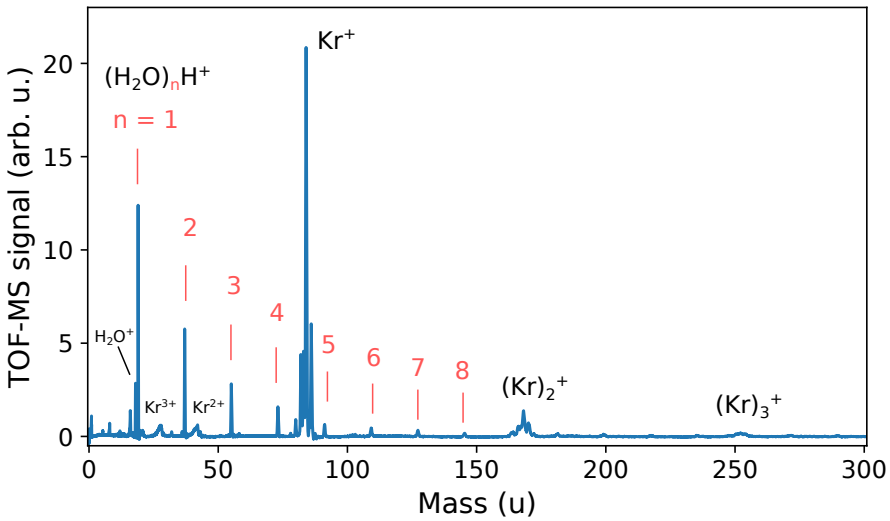

Figure 2.11: **TOF-MS of a molecular beam of water seeded in krypton.** Cluster signals for both H_2O as well as Kr are observed. The cluster signal appears to decay exponentially with the cluster size. The signal of the parent ion H_2O^+ is suppressed.

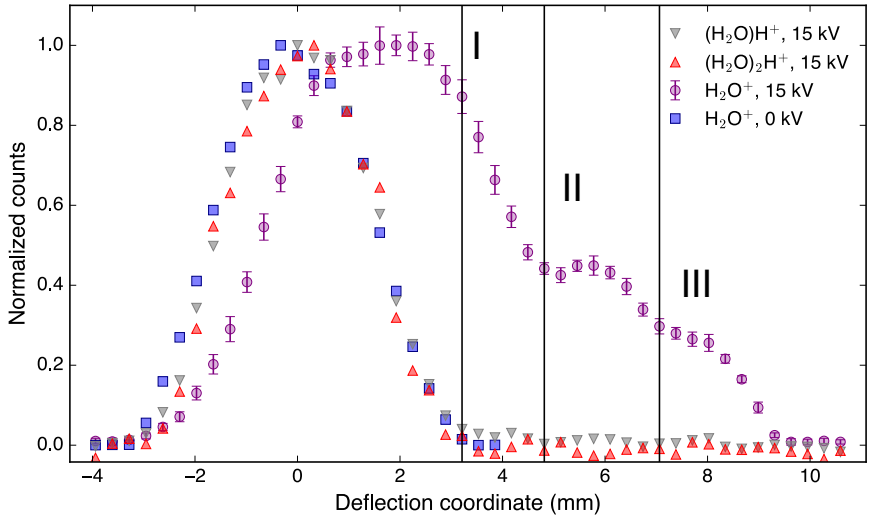

Figure 2.12: **Experimental deflection profiles of the water beam measured by fs-laser ionization.** Beam profiles of the parent water ion H_2O^+ were measured as function of the vertical deflection coordinate at deflector voltages of 0 kV (blue squares and 15 kV (purple circles). Deflection profiles of the water cluster as detected by their fragment ions $(H_2O)H^+$ and $(H_2O)_2H^+$ are also shown (grey and red triangles, respectively). These were produced from their parent clusters by fs-laser ionization and dissociation. No significant deflection is observed for these clusters. The vertical lines labelled I, II and III specify the positions at which the reaction rate measurements of chapter 3 were performed. Error bars correspond to one standard error.

2.4.3.4 Beam density

The time-averaged density of water molecules in the molecular beam, $n_{\mathrm{MB,avg}}$, relates to the density of molecules in one gas pulse, $n_{\mathrm{MB,pulse}}$, via

$$n_{\mathrm{MB,avg}} = n_{\mathrm{MB,pulse}} f_{\mathrm{rep}} \tau_{\mathrm{pulse}}, \tag{2.11}$$

where $f_{\mathrm{rep}} = 200$ Hz is the repetition rate of the gas valve and $\tau_{\mathrm{pulse}} = 487\mu$s is the FWHM of the temporal width of the molecular beam pulse in the reaction region.

To estimate $n_{\mathrm{MB,pulse}}$, the fs-laser ionization signal I_{MB} of H_2O from the molecular beam was compared with the signal I_{BG} obtained from ionization of water in the background gas of the trap chamber. In this measurement, the water beam was deflected at a deflector voltage of 15 kV and the deflection coordinate was set to $y = 4.5$ mm (position II), to avoid interference from water clusters. Assuming that the ionization volumes V_{MB} and V_{BG} were equal (the diameter of the molecular beam of 4 mm was larger than the laser-focus diameter of ≈ 50 μm), $n_{\mathrm{MB,pulse}}$ was estimated according to

$$n_{\mathrm{MB,pulse}} = n_{\mathrm{BG}} \frac{I_{\mathrm{MB}}}{I_{\mathrm{BG}}} \underbrace{\frac{V_{\mathrm{MB}}}{V_{\mathrm{BG}}}}_{\approx 1} = n_{\mathrm{BG}} \frac{I_{\mathrm{MB}}}{I_{\mathrm{BG}}} \tag{2.12}$$

Here, the density of water molecules in the background gas, n_{BG}, was estimated from a comparison of the measured pseudo-first-order rate constant of the reaction of background water with N_2H^+ ions with a literature value for the second-order rate constant at 300 K:

$$n_{\mathrm{BG}} = k'_{\mathrm{BG}} / k_{\mathrm{lit,300K}}, \tag{2.13}$$

with $k_{\mathrm{lit,300K}} = 2.6(4) \times 10^{-9}$ cm^{3}s^{-1} taken from [76]. The value of the time-averaged beam density thus obtained is $n_{\mathrm{MB,avg}} = 3.0(5) \times 10^5$ cm^{-3}. This value is in line with previous results [15] after adjustment for the different repetition rates of the experiments.

2.4.4 Molecular beam of DBB

The molecular beam was generated from DBB vapor at room temperature seeded in neon carrier gas at 5 bar. The repetition rate was set to 10 Hz for deflection profile measurements, matching the repetition rate of the YAG laser. For reaction rate measurements, it was set to 200 Hz to shorten the data acquisition time. A gas pulse duration of 250 μs was measured at the LQT.

For deflection experiments, a voltage of 13 kV was applied between the two deflector electrodes to generate the required vertical electric field gradient [46, 6, 72, 21]. By comparison of the measured deflection profiles with Monte-Carlo simulations [46, 13, 21], a rotational temperature of 1.0 K could be estimated.

2.4.4.1 Beam velocity

The beam velocity measurement for DBB in neon was conducted in the same way as the beam velocity measurement for water in argon (cf. section 2.4.3.1). The longitudinal beam profiles of DBB for different valve positions are shown in Fig. 2.13a. To determine the peak delays, Gaussian functions were fitted to the peaks. The resulting linear relation between the valve positions and peak delays is plotted in Fig. 2.13b. The linear fit yields a beam velocity of $v = 843$ m/s with a velocity spread of $\delta v = 58$ m/s determined from the temporal spread of the longitudinal beam profiles.

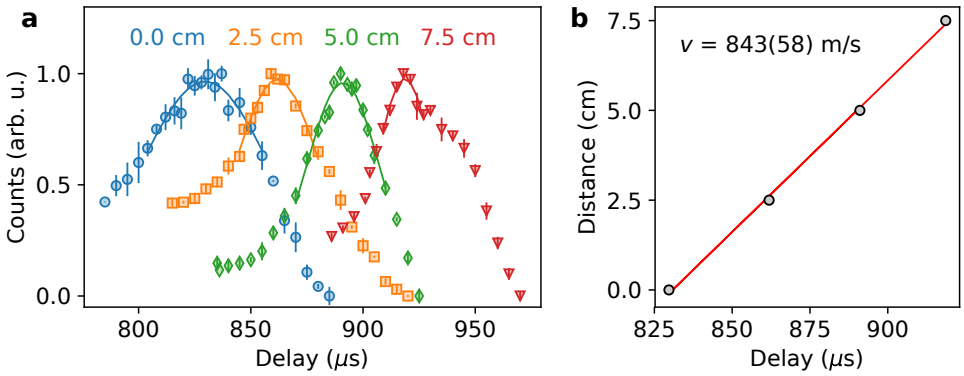

Figure 2.13: **Determination of the molecular beam velocity.** a)Beam profile measurements for different longitudinal positions of the piezo valve. The solid lines are Gaussian fits to the data. b) Linear fit through the maxima of the gaussian fits giving the beam velocity of 843(58) ms^{-1}.

2.4.4.2 Beam density

Knowledge of the DBB density in the molecular beam was necessary to convert the measured pseudo-first order rate constants in chapters 8 and 6 into bimolecular rate constants. Following refs. [67, 77], the DBB density was determined from a measurement of the ion yield as a function of the laser intensity for fs laser pulse ionization. The absolute ion yield was calibrated using the method of section section 2.3.6.

For this measurement, a voltage of 13 kV was applied to the deflector and the molecular-beam apparatus was set to a deflection coordinate of $y = 0$ mm. The molecular beam was ionised by multi-photon ionisation using laser pulses with a duration of 150 fs at 775 nm and the total, calibrated ion yield (cf. section 2.3.6) was measured as a function of the laser-pulse intensity (Fig. 2.14). In the saturated regime, the ion yield was found to scale logarithmically with laser intensity $I > 3.3 \times 10^{14}$ W/cm^2. This behaviour is expected for multi-photon ionisation [67] and allows the extraction of the molecular-beam peak density n_{peak} from the slope of the line [77]

$$m := \frac{\mathrm{d}S}{\mathrm{d}\ln I/I_0} = 2\pi\alpha\sigma_r^2 d n_{\mathrm{peak}} \tag{2.14}$$

where S is the ion count, I is the laser intensity, I_0 is the saturation intensity of the relevant molecular species, $\alpha = 0.57$ is the detection efficiency, $\sigma_r = 7.5$ μm is the $e^{-1/2}$ radius of the laser beam and $d = 2.5$ mm is the diameter of the molecular beam. The values $m = 39(2)$ and $I_0 = 2.56(5) \times 10^{14}$ W/cm^2 were determined from a linear fit of S as a function of $\ln(I)$ (Fig. 2.14). Using (2.14), a DBB density of $n_{\mathrm{peak}} = 7.8(7) \times 10^7$ cm^{-3} was obtained. The uncertainty also includes the propagated error of the TOF-MS calibration. Since the molecular beam was pulsed with a repetition rate $f_{\mathrm{rep}} = 200$ Hz and a pulse width $\tau_{\mathrm{pulse}} = 250$ μs at the LQT, the relevant average density for the reaction experiments was calculated to be $n_{\mathrm{avg}} = n_{\mathrm{peak}} f_{\mathrm{rep}} \tau_{\mathrm{pulse}} = 3.9(4) \times 10^6$ cm^{-3}.

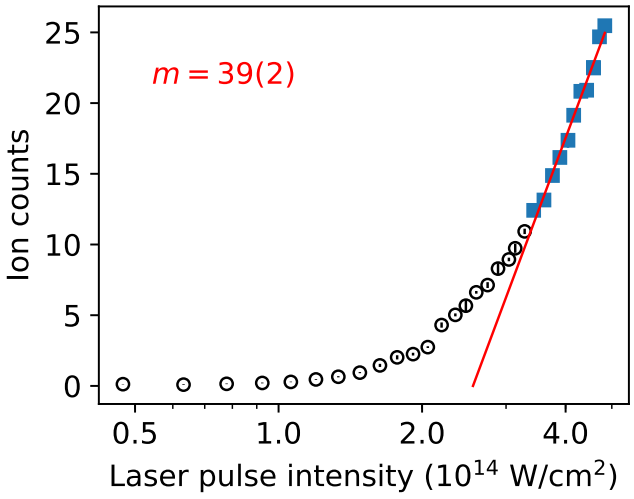

Figure 2.14: **Calibration of the DBB beam density.** The ion yield from fs-laser photoionisation was measured as a function of the laser intensity. At large intensities $> 3.3 \times 10^{14}$ W/cm^2 (blue squares), the ion yield was well represented by a logarithmic dependence on the laser intensity (red line).

3

Different reactivities of *para*- and *ortho*-water towards diazenylium ions

Water is one of the most fundamental molecules in chemistry, biology and astrophysics. It exists as two distinct nuclear-spin isomers, *para*- and *ortho*-water, which do not interconvert in isolated molecules. The experimental challenges in preparing pure samples of the two isomers have thus far precluded a characterization of their individual chemical behaviour. Capitalizing on recent advances in the electrostatic deflection of polar molecules, we separate the ground states of *para*- and *ortho*-water in a molecular beam to show that the two isomers exhibit different reactivities in a prototypical reaction with trapped diazenylium ions. Based on *ab initio* calculations and a modelling of the reaction kinetics using rotationally adiabatic capture theory, we rationalize this finding in terms of different rotational averaging of ion-dipole interactions during the reaction.

The content of this chapter has been published in [21][1].

3.1 Introduction

Water, H_2O, is one of the key molecules in nature, it acts as the fundamental solvent in biological systems and is one of the major molecular constituents of the universe. It exists in two forms, *para(p)*- and *ortho(o)*-water, which are distinguished by their values of the quantum number of the total nuclear spin I, where $I = 0$ and 1 for p- and o-H_2O, respectively (see section 1.1.1). Interconversion of the nuclear-spin isomers is forbidden in isolated molecules and nuclear-spin symmetry is usually conserved in collisions, by electromagnetic radiation and even in chemical reactions [18, 19, 20]. However, nuclear-spin-symmetry interconversion has been observed in a variety of polyatomic molecules and has been rationalized to occur via doorway states with a mixed nuclear-spin character [19, 78, 79]. For water in the vapour and condensed phases, the *para*/*ortho*-interconversion rates reported in the literature vary widely and remain a controversial topic [80, 81, 82].

Apart from their total nuclear spin, *para*- and *ortho*-water also differ in other important respects. Because the generalized Pauli principle dictates that the total molecular

[1] H. Gao assisted with the experiments presented in this chapter.

wavefunction has to be antisymmetric under the permutation of the two hydrogen nuclei in the molecule [18], *(ortho-) para*-water is associated with (anti)symmetric rotational functions in the electronic-vibrational ground state of the molecule. Thus, nuclear-spin and rotational symmetry are intimately linked [15]. As a consequence, the ground state of *para*-water is the absolute rotational ground state $|j_{K_aK_c}\rangle = |0_{00}\rangle$, whereas the ground state of *ortho*-water is the first excited rotational state $|j_{K_aK_c}\rangle = |1_{01}\rangle$. Here, j denotes the quantum number of the rotational angular momentum and K_a and K_c are the quantum numbers of the projection of the rotational angular momentum on the a and c principal axes of inertia of the molecule, respectively.

Considering the different properties of its two nuclear-spin isomers and the eminent importance of water in a variety of chemical contexts, it begs the question whether *para*- and *ortho*-water also show different chemical behaviour. In a wider context, this problem ties into ongoing efforts to understand how different molecular degrees of freedom (translation, nuclear spin, rotation, vibration, electronic motion) and the interplay between them influence chemical reactivity. Despite the significant amount of studies focusing on vibrational effects in chemical reactions [83, 84, 85], the roles of nuclear spin and molecular rotation have scarcely been explored experimentally. This is mainly due to the fact that rotational energy transfer is likely to happen in any collision rendering it difficult to prepare molecules in specific rotational levels [86, 6] so that only comparatively few rotational-state resolved studies have been reported so far [87, 88, 89]. A similar scarcity of data exists with regard to studies involving individual nuclear-spin isomers [90] which are in general difficult to separate and to prepare individually [15, 91].

Recent progress in manipulating polar molecules using electrostatic fields has made it possible to select and spatially separate different conformers and rotational states of molecules in supersonic molecular beams [6]. By combining this technology with a stationary reaction target of Coulomb-crystallized ions in a linear quadrupole ion trap (LQT) [17, 9], we have recently studied conformer-selected molecule-ion reaction dynamics and observed that reaction-rate constants can strongly depend on molecular conformation [13, 72]. Here, we extend this method to the separation of different nuclear-spin isomers using their different rotational properties in order to study ion-molecule reactions with control over the rotational and nuclear-spin state of the neutral reaction partner, a field on which only scarce experimental data are available so far. Our approach is particularly suited for polyatomic neutrals for which rigorous rotational state preparation is difficult to achieve solely by supersonic cooling [88]. As an example, we investigate the proton-transfer reaction of water with ionic diazenylium (N_2H^+),

$$H_2O + N_2H^+ \rightarrow N_2 + H_3O^+, \tag{3.1}$$

an important molecule in astrochemistry which has been observed in the interstellar medium [92]. Its detection has proven crucial to trace molecular nitrogen in pre-stellar clouds to understand the early stages of star formation [93, 94].

We find that the para-species reacts 23(9)% faster than the ortho-isomer. Based on ab initio calculations and a modelling of the reaction kinetics using rotationally adiabatic capture theory, we rationalize this finding in terms of different rotational averaging of ion-dipole interactions during the reaction.

3.2 Results

3.2.1 Experimental approach

The two ground states of *para*- and *ortho*-water show distinct responses to an electric field, i.e., different Stark-energy shifts and correspondingly different effective space-fixed dipole moments (see section 2.4.2 and [15]). This enables their spatial separation by the electric field gradient of the electrostatic deflector [15, 6].

The experimental setup is schematically depicted in Figure 3.1. It consists of a molecular-beam machine equipped with the electrostatic deflector connected to an ultrahigh-vacuum chamber housing an ion trap [72, 61]. A beam of internally cold molecules was formed in a pulsed supersonic expansion of water seeded in argon carrier gas. The molecular beam was collimated by two skimmers before entering the electrostatic deflector. A voltage of 15 kV was applied across the deflector electrodes in order to generate a vertical electric field gradient for the spatial separation of the two nuclear-spin isomers. After passing another skimmer, the beam was directed towards the LQT. The trap was loaded with Coulomb crystals of laser-cooled Ca^+ ions [17, 13] as well as sympathetically cooled N_2H^+ reactant ions (image inset in Figure 3.1). By vertically tilting the molecular beam apparatus relative to the LQT, different regions of the deflected molecular beam were overlapped with the Coulomb crystals [72]. The tilting angle of the molecular beam apparatus defined a deflection coordinate y for molecules arriving at the trap centre. After exposure to the molecular beam for a variable time period, the Coulomb crystals were ejected into a high-resolution time-of-flight mass spectrometer (TOF-MS) [61] for the mass and quantitative analysis of their constituents.

3.2.2 Isomer populations in the deflected water beam

In order to probe its composition in terms of quantum states and to characterize the spatial separation of the two nuclear-spin isomers, density profiles of the molecular beam were measured. A pulsed ultraviolet laser beam was used to generate water ions by (2+1) resonance-enhanced multi-photon ionization (REMPI) via selected rotational levels of the $\tilde{C}$ electronic state [74] (see section 2.4.3.2). The ions were subsequently ejected into the TOF-MS. This technique enabled the selective detection of the ground states of either *para*- or *ortho*-water and the determination of the individual density profiles of the two isomers in the beam. From a REMPI spectrum of an undeflected water beam, it was confirmed that the supersonic expansion was composed predominantly of the $j_{K_aK_c} = 0_{00}$ and 1_{01} rotational states of H_2O, i.e., the ground states of *p*- and *o*-H_2O, respectively (see section 2.4.3.2). A possible minor contribution from the 1_{10} state did not interfere with the present experiments (see section 2.4.2 and appendix A.1).

Figure 3.2a shows deflection profiles of *para*- (red diamonds) and *ortho*- (blue squares) water obtained from the ion signal at mass-to-charge ratio $m/z = 18$ u recorded as a function of the deflection coordinate y at a deflector voltage of 15 kV. The purple circles represent the sum of the *para*- and *ortho*-profiles. The different projections of the angular momentum of the ground state of *ortho*-water onto the space-fixed direction of the electric field leads to two components, $M = 0$ and $|M| = 1$, which exhibit a weak and strong Stark shift, respectively. These correlate with the two peaks of the *o*-H_2O deflection profile at low and high deflection coordinates, respectively. Contrarily, the *para*-isomer

only has one angular-momentum projection component $M = 0$ with an intermediate Stark shift such that its deflection profile shows a single peak situated in between the two peaks of the *ortho*-form. In this way, a partial spatial separation of the two isomers was achieved and the o/p-ratio was well defined at each deflection coordinate [15]. The solid and broken lines show corresponding theoretical deflection profiles derived from Monte Carlo trajectory simulations (see section 2.4.2).

In addition, a femtosecond (fs) laser was employed to probe molecules reaching the trap centre by strong-field ionization irrespective of the species or the internal quantum state [95]. Subsequent ion ejection into the TOF-MS enabled the determination of the combined relative density of *para*- and *ortho*-water molecules in the beam as a function of the deflection coordinate. The acquired beam profiles for deflector voltages of 0 and 15 kV are presented in Figure 3.2b as yellow triangles and purple circles, respectively. At 15 kV, experiment and simulation (dashed grey line) agree well at large deflection coordinates, but differ significantly around $y = 0$. In this region, the mass spectra indicate the presence of clusters formed in the supersonic expansion. A fs laser pulse can break these clusters resulting in water ions detected together with the water-monomer signal at $m/z = 18$ u in the TOF-MS. Our data also show that these clusters are not deflected and do not contaminate the beam at deflection coordinates larger than 2 mm (see section 2.4.3.3). This picture is corroborated by the reproduction of the experimental beam profile by a weighted superposition (black solid line) of simulations of the deflected water beam at 15 kV and an undeflected beam at 0 kV (grey solid line).

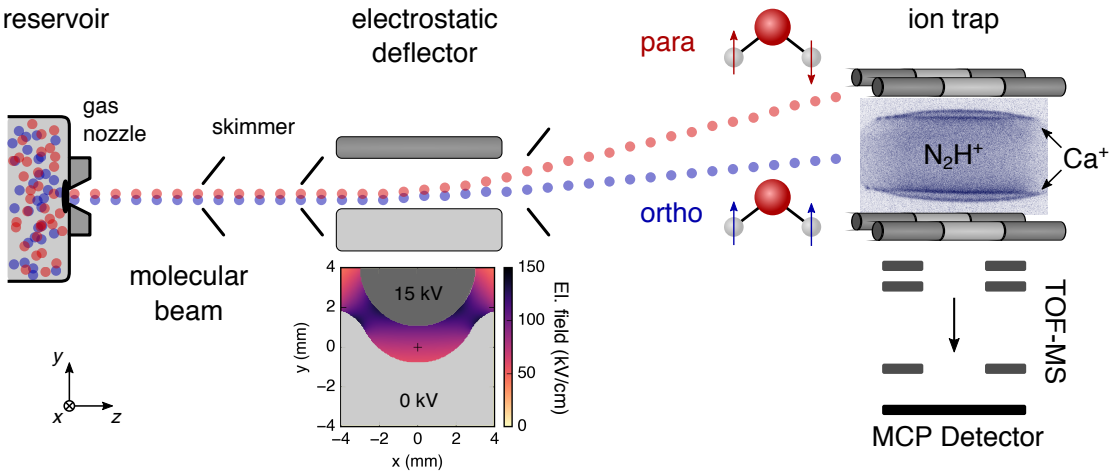

Figure 3.1: **Schematic of the experimental setup.** A pulsed molecular beam of water molecules seeded in argon emanates from a room-temperature reservoir through a pulsed gas nozzle and passes an electrostatic deflector. The inhomogeneous electric field inside the deflector (shown in the inset below) spatially separates *para*- and *ortho*-water molecules due to their different effective dipole moments. After the deflector, the beam is directed at an ion trap containing a Coulomb crystal of Ca^+ and sympathetically cooled N_2H^+ reactant ions (inset image). The products and kinetics of reactive collisions between N_2H^+ and H_2O are probed using a time-of-flight mass spectrometer (TOF-MS) [61].

Probing the specific reactivities of the two isomers requires the preparation of samples with well defined *para*/*ortho*-ratios. Based on the deflection profiles and the simulations in Figure 3.2a, three deflection coordinates with varying relative populations of *para*- or *ortho*-water were chosen. At each of these positions labelled I, II and III in Figure 3.2b, REMPI spectra were recorded from which the populations of *para*- and *ortho*-

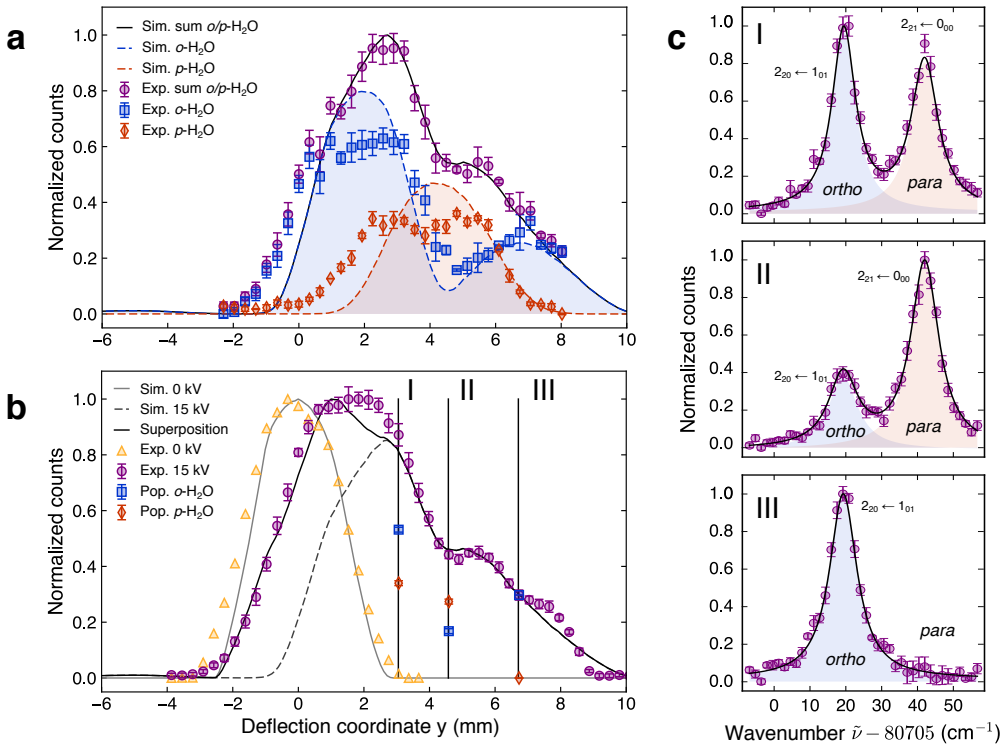

Figure 3.2: **Molecular-beam deflection profiles of the ground states of para and ortho-water. a** Experimental isomer-specific density profiles of *o*- (blue squares) and *p*-H_2O (red diamonds) in the deflected molecular beam (deflector voltage 15 kV) measured by (2+1) REMPI together with the total deflection profile (sum of the *ortho*- and *para*-signals, purple circles). The lines represent Monte-Carlo trajectory simulations of the deflection profiles. The contributions from *ortho*- and *para*-water are indicated by the blue and red shaded areas, respectively. **b** Total water deflection profile measured by femtosecond-laser ionization for deflector voltages of 0 kV (yellow triangles) and 15 kV (purple circles). The three vertical lines marked I, II and III indicate the deflection coordinates at which reaction rates were measured. The red/blue symbols represent the relative populations of the isomers normalized to the total signal at positions I, II and III as determined from the REMPI spectra shown in c. **c** REMPI spectra of H_2O measured at the three positions I, II, III (purple circles). The two peaks observed at 80724 cm^{-1} and 80747 cm^{-1} correspond to transitions from the ground states of *ortho*- and *para*-water, respectively. The peaks are fitted with a sum of two Lorentzians (solid black line) with contributions from *ortho*- and *para*-isomers depicted as blue and red shaded areas, respectively. Error bars correspond to one standard error of at least three independent measurements.

water were determined (Figure 3.2c). From fits of the intensities of the lines in the spectra, the relative populations of the two isomers were obtained (see section 2.4.3.2). The populations of *para*- (*ortho*-) water thus obtained were 39(1)% (61(1)%), 62(2)% (38(2)%) and 0% (100%) at positions I, II and III. We note that at position III, the beam consists of pure *ortho*-water within the measurement uncertainties and therefore enables a direct measurement of the reaction rate constant of *ortho*-water.

3.2.3 Reaction-rate measurements

With the molecular beam prepared with well-known ratios of the two isomers at different deflection coordinates, measurements of the rate of reaction (3.1) were performed. First, a Coulomb crystal of about 1000 Ca^+ ions was loaded into the LQT. Then, nitrogen gas was leaked into the vacuum chamber at a partial pressure of 4.0×10^{-9} mbar and N_2^+ ions were generated by fs-laser ionization. After the formation of N_2^+ ions in the trap, H_2 gas (partial pressure 2×10^{-9} mbar) was leaked into the vacuum chamber for 30 s to quantitatively convert N_2^+ into N_2H^+ via the reaction $N_2^+ + H_2 \rightarrow N_2H^+ + H$. The thus formed N_2H^+ ions were sympathetically cooled into the Coulomb crystal and accumulated at its centre (inset in Figure 3.1). Subsequently, the molecular beam apparatus was set to a specific deflection coordinate and the deflector was turned on at a voltage of 15 kV to direct the molecular beam at the Coulomb crystal and engage the reaction. After a variable period of exposure to the molecular beam, the reduction of the number of N_2H^+ reactant ions was probed by ejecting the Coulomb crystal into the TOF-MS [61] (Figure 3.3). In addition, the formation of H_3O^+ as the ionic reaction product was verified using the TOF-MS. At each of the three deflection coordinates I–III, five independent sets of data were taken, each consisting of one reaction measurement with a deflected molecular beam (deflector voltage 15 kV) and a subsequent measurement of the rate of reaction of N_2H^+ with the background gas in the vacuum chamber. The background measurement was performed by setting the deflector voltage to 0 kV while keeping the deflection coordinate constant, thus pointing the molecular beam away from the centre of the LQT. For each data set, the N_2H^+ ion signal $N(t)$ was recorded as a function of reaction time t in three consecutive measurements.

Since the number of water molecules is continuously replenished through the molecular beam, the rate constants could be determined within the framework of a pseudo-first-order kinetics treatment (cf. section 1.4.1). Hence, the data were analyzed according to an integrated pseudo-first-order rate law

$$\ln\left(\frac{N(t)}{N(0)}\right) = -k't \tag{3.2}$$

with the pseudo-first-order rate constant k' determined from a least-squares fit. For every data set, the pseudo-first-order rate constants of the reactions with background gas were directly subtracted from the total rate constants to give the rate constants for the reactions of the diazenylium ions with water from the molecular beam.

Combining the determinations of the total reaction-rate constants, of the relative populations of *o*- and *p*-H_2O at positions I, II and III, and of the combined density profile of the deflected beam, the individual reaction-rate constants k_o and k_p of *ortho*- and *para*-water, respectively, were deduced. For each of the three deflection coordinates

y_i ($i \in \{\mathrm{I}, \mathrm{II}, \mathrm{III}\}$), the total first-order rate constant $k'_{\mathrm{tot},i}$ is given by

$$k'_{\mathrm{tot},i} = \tilde{n}_i \left(p_{o,i}\, k'_o + p_{p,i}\, k'_p \right), \tag{3.3}$$

where $p_{o,i}$ and $p_{p,i}$ are the populations of *ortho*- and *para*-water extracted from the REMPI measurements, respectively, and $\tilde{n}_i$ are the relative densities of the water beam at positions y_i. $\tilde{n}_i$ is obtained from the beam profile $I(y)$ measured with the fs laser at 15 kV (Figure 3.2b) via $\tilde{n}_i = I(y_i)/I(y_{\mathrm{II}})$ with position II taken as reference point. All parameters defining the set of equations (3.3) are summarized in Table 3.1. Once k'_o and k'_p were known, the relative difference of the reaction rates of the two isomers was calculated as $r = 2(k'_p - k'_o)/(k'_p + k'_o)$.

The system of equations (3.3) was solved by a least-squares optimization, minimising

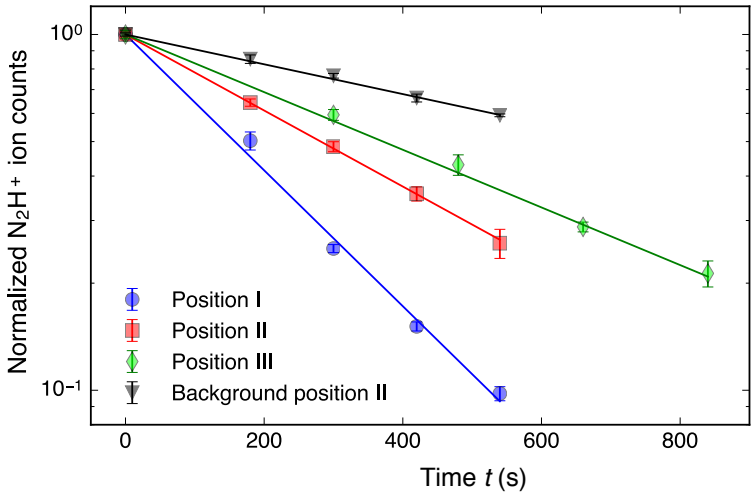

Figure 3.3: **Reaction-rate measurements at the deflection coordinates I–III indicated in Figure 3.2b.** The data are normalized to the ion signal at time $t = 0$. The lines represent fits to the data according to an integrated pseudo-first-order rate law. The black triangles show an example of a measurement of the reaction rate with background gas at position II for comparison. Error bars correspond to one standard error of four independent measurements.

Region i	Pseudo 1st oder rates k'_i [s^{-1}]	Populations $p_{o,i} : p_{p,i}$	Normalized ion signal I_i
I	$3.13(5) \cdot 10^{-3}$	0.61(1) : 0.39(1)	0.87(4)
II	$1.63(4) \cdot 10^{-3}$	0.38(2) : 0.62(2)	0.44(1)
III	$0.95(5) \cdot 10^{-3}$	1 : 0	0.30(2)

Table 3.1: **Summary of measured data.** Total pseudo-first-order reaction-rate constants k'_i, nuclear-spin isomer populations p_σ and normalized ion signal I_i at the three positions i = I, II and III.

the cost function

$$S(k'_o, k'_p) = \sum_i \left[k'_{\mathrm{tot},i} - \tilde{n}_i(p_{o,i}\, k'_o + (1 - p_{o,i})\, k'_p)\right]^2 . \tag{3.4}$$

From the least-squares fit to the experimental data, the pseudo-first-order rate constants were determined to be $k'_o = 1.4(1) \times 10^{-3}$ s^{-1} and $k'_p = 1.8(1) \times 10^{-3}$ s^{-1} yielding a relative difference $r = 23(9)\%$ between the reactivities of the *para*- and *ortho*-isomers (see Table 3.2).

Absolute bimolecular reaction-rate constants $k_{o/p}$ were calculated using the relation $k_{o/p} = k'_{o/p}/n_{\mathrm{H_2O,II}}$, where the total time-averaged beam density at the reference position II, $n_{\mathrm{H_2O,II}} = 3.0(5) \times 10^5$ cm^{-3}, was estimated according to the procedures described in section 2.4.3.4. Using this information, the absolute bimolecular reaction rates obtained from this experiment are $k_o = 4.8(9) \times 10^{-9}$ cm^{3}s^{-1} for *ortho*-water and $k_p = 6(1) \times 10^{-9}$ cm^{3}s^{-1} for *para*-water, respectively.

3.3 Discussion

To understand the reason for the different reactivities of *para*- and *ortho*-water in the present case, *ab initio* calculations of the energy profile of the reaction were performed.[2] In order to test whether the reaction $H_2O + N_2H^+ \rightarrow H_3O^+ + N_2$ is barrierless, electronic structure calculations were carried out using the Gaussian 09 suite of codes [97]. It was assumed for this purpose that the O-H^+ distance approximates the reaction coordinate. This distance was constrained while optimizing all other internal coordinates at the CCSD/aug-cc-pVTZ level of theory. The resulting electronic energies for the optimized structures along the O-H^+ coordinate are shown in Fig. 3.4. Over the full range of O-H^+ distances from 100 to 260 pm, the energy continuously decreases from the reactants towards the products (from right to left in Fig. 3.4). No transition state could be located.

As can be seen in Figure 3.5a, the reaction was found to be barrierless and to proceed via the formation of an intermediate complex in which one hydrogen atom is shared between the nitrogen and water moieties. The energy of the products was found to be about 2 eV lower than the one of the reactants. This situation suggests that the kinetics can be modelled within the framework of a rotationally adiabatic quantum capture theory for barrierless ion-molecule reactions [56, 58] (cf. section 1.4.3). According to this approach, the reaction rates are entirely dominated by the properties of the long-range interaction potential of the reactants and centrifugal effects. All collisions up to a maximum total angular momentum J_{max} for which the relative kinetic energy exceeds the height of the centrifugal barrier lead to a successful reactive encounter.

For the present case, the relevant terms in the long-range interaction potential are the charge-induced dipole and charge-permanent dipole interactions. Molecular parameters for water used in this calculation are given in Table A.1. Adiabatic-capture rate constants k^{AC} were calculated using equation (1.35) for the ground states of the two nuclear-spin

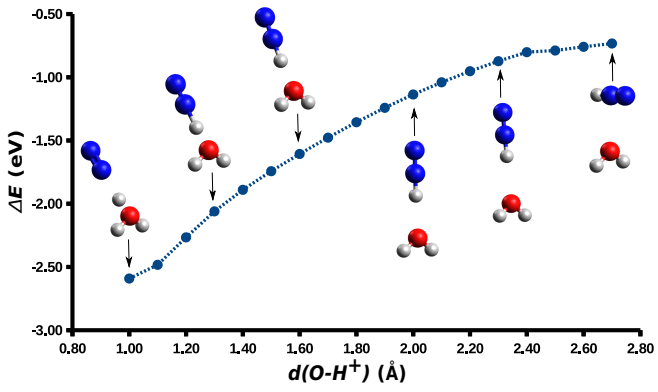

Figure 3.4: **Electronic structure calculations.** Optimized structures along the reaction coordinate (O – H^+ distance) of the proton transfer between N_2H^+ and H_2O at the CCSD/aug-cc-pVTZ level of theory. The energy is relative to that of the reactants. Blue spheres represent nitrogen atoms, red spheres oxygen atoms and white spheres hydrogen atoms.

[2] The quantum chemical calculations were performed by U. Rivero [96].

isomers. The mean collision velocity was assumed to be the molecular beam velocity $v = 575$ m/s (see section 2.4.3.1). In addition, the velocity distribution of the H_2O molecules in the molecular beam (see section 2.4.3.1) as well as the micromotion velocities of the N_2H^+ ions in the Coulomb crystals (see section 2.3.3) lead to a spread of the collision energy. The total uncertainty of the experimental collision velocity was calculated to be

$$\delta v = \sqrt{v_{\mathrm{rms}}^2 + \delta v_{\mathrm{beam}}^2} = 175 \text{ m/s}. \tag{3.5}$$

Here, the longitudinal velocity spread of the molecular beam $\delta v_{\mathrm{beam}} = 65$ m/s as well as the root-mean-squared ion micromotion velocity of $v_{\mathrm{rms}} = 163$ m/s were used. This spread δv of the collision velocity v was used to calculate the uncertainties of the theoretical rate constants $\delta k^{\mathrm{AC}} = [k^{\mathrm{AC}}(v + \delta v) - k^{\mathrm{AC}}(v - \delta v)]/2$. The calculated rates $k^{\mathrm{AC}}_{o/p}$ and their relative difference r are listed in table 3.2 and compared with the experimental values.

In the current experiments, both nuclear-spin isomers were cooled down to their relevant rotational ground states. The anisotropic nature of the ion-dipole interaction implies that it is sensitive to the rotational quantum state of the neutral molecule. Figures 3.5b and c show rotationally adiabatic, centrifugally corrected interaction potentials for collisions of N_2H^+ with *o*- and *p*-H_2O, respectively, as a function of the total angular

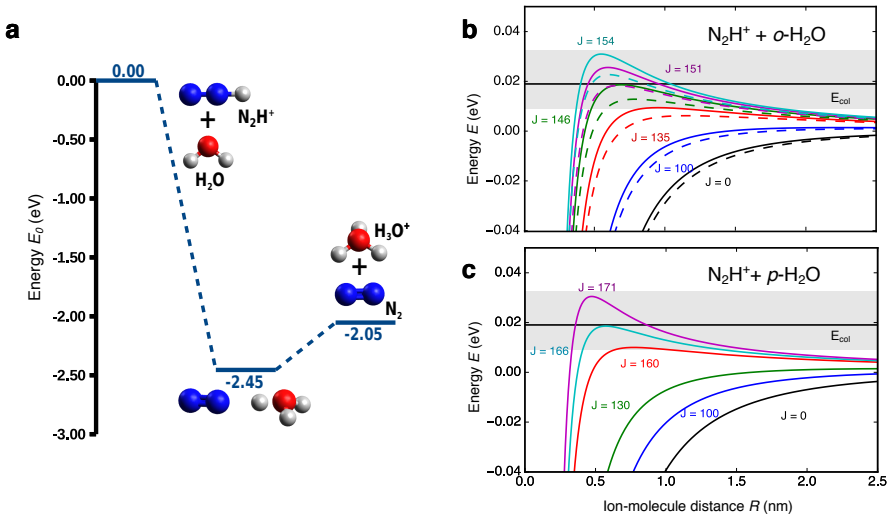

Figure 3.5: **Theoretical predictions from *ab initio* calculations and adiabatic capture theory.** **a** Potential-energy profile along the reaction coordinate for the proton transfer reaction between N_2H^+ and H_2O at the CCSD/aug-cc-pVTZ level of theory. The relative energies with respect to the reactants as well as the structures of the stationary points are shown. Blue, red and white spheres represent nitrogen, oxygen and hydrogen atoms. **b, c** Rotationally adiabatic, centrifugally corrected long-range interaction potentials for the reaction of the ground states of *o*- (b) and *p*- (c) H_2O with N_2H^+ for different values of the total angular momentum quantum number J. In b, the dashed (solid) lines correspond to the $|\Omega| = 0(1)$ components of the *ortho*-ground state. The grey-shaded areas show an estimate of the uncertainty in the experimental collision energy E_{col} indicated by the black horizontal line.

momentum quantum number J. For the case of vanishing total angular momentum ($J = 0$), one can see that the potential energy curves for the *ortho*-species are less steep than the one of the *para*-isomer, reflecting the stronger rotational averaging of the ion-dipole interaction in the ground state of *o*-H_2O. For the $|j_{K_a K_c}|\Omega|\rangle = |0_{00}0\rangle$ ground state of the *para*-species one obtains a maximum collisional angular-momentum $J_{\max} = 166$ at the experimental collision energy $E_{\mathrm{col}} = 0.019$ eV. Here, Ω is the quantum number of the projection of $\vec{j}$ on the distance vector between the ion and the neutral molecule in a body-fixed coordinate system describing the collision [56, 58]. This value can be compared to $J_{\max} = 151$ and $J_{\max} = 146$ for the $|1_{00}0\rangle$ and $|1_{01}1\rangle$ states of the *ortho*-isomer, respectively.

The quantum capture model predicts a reaction-rate constant of $k_p^{\mathrm{AC}} = 5(1) \times 10^{-9}$ cm^{3}s^{-1} for *para*-water compared to $k_o^{\mathrm{AC}} = 4.0(9) \times 10^{-9}$ cm^{3}s^{-1} for *ortho*-water (see table 3.2). The value for the *ortho*-species was obtained by summing over the contributions of all Ω components to the reaction cross section assuming that the original preparation of M states of $o{-}H_2O$ in the deflector was scrambled during the transit of the molecules through the RF fields in the ion trap. In a classical interpretation of this result, the higher maximum angular momentum obtained for the *para*-isomer implies a larger impact parameter and, therefore, a higher reaction rate. The theoretical predictions agree with the measured values within their experimental uncertainties. The relative difference of the theoretical reaction-rate constants was calculated to be $r = 24(5)\%$ which can be compared with the experimental value of $r = 23(9)\%$. The errors in the calculated rate constants arise from the uncertainty in the collision energy due to the experimental velocity distribution of the molecular beam and the micromotion of the ions in the large Coulomb crystals [17].

	k'[s^{-1}]	k[cm^{3}s^{-1}]	k^{AC} [cm^{3}s^{-1}]
o-H_2O	$1.4(1) \cdot 10^{-3}$	$4.8(9) \cdot 10^{-9}$	$4.0(6) \cdot 10^{-9}$
p-H_2O	$1.8(1) \cdot 10^{-3}$	$6(1) \cdot 10^{-9}$	$5(1) \cdot 10^{-9}$
Rel. difference r	23(9)%		24(5)%

Table 3.2: **Comparison of experimental and calculated rate constants.** Experimental pseudo-first-order and second-order rate constants k' and k, respectively, and theoretical adiabatic capture-rate constants k^{AC} for the reaction of N_2H^+ with *o*- and *p*-H_2O.

3.4 Conclusion

In conclusion, we have studied chemical reactions of the spatially separated ground states of *para*- and *ortho*-water with trapped diazenylium ions. We found a 23(9)% higher reactivity for the *para* nuclear-spin isomer which we attribute to the smaller degree of rotational averaging of the ion-dipole long-range interaction compared to the *ortho*-species. The observed difference in reactivities is thus a rotational effect which is induced by the nuclear-spin symmetry via the generalized Pauli principle. The present results highlight the interplay between nuclear-spin and rotational symmetry and its ramifications on chemical reactivity. They also provide an illustration of the effects of exchange symmetry on chemical processes which may be put in context with, e.g., its manifestations in the dynamics of ultracold collisions [98]. Measurements such as the ones presented here fill a gap in experimental investigations of ion-neutral reactions with control over the quantum states of the reactants. Indeed, to our knowledge the present study is the first in which rotationally state-selected polyatomic neutral molecules have been reacted with ions. The methods employed here are applicable to studies of a broad range of ion-neutral processes. They enable a quantitative understanding of how different molecular quantum states and, as demonstrated in our earlier study [13], molecular conformations, influence chemical reactivity.

4

Generation of vacuum-ultraviolet radiation

4.1 Introduction

Photoionization of molecules is an important tool for mass-spectrometry [99, 100, 101], the preparation of molecular cations in ion traps [17] as well as for high-resolution spectroscopy [102]. One common approach is multi-photon ionization, where a molecule simultaneously absorbs multiple photons to overcome its ionization energy [103]. This technique makes use of commercial high-power pulsed lasers in the ultraviolet to near-infrared wavelength range. Due to the short laser pulse lengths on the ns to fs timescale, extremely large peak intensities can be reached in the laser focus, which enable significant ionization probabilities. One drawback of this method is, however, that these large optical intensities can also cause the dissociation of covalent bonds and thus lead to fragmentation of the molecules. This effect is particularly undesirable for mass-spectrometry as well as the preparation of molecular cations in ion traps. Consequently, these applications require "soft" ionization using excitation by single high-energy photons. Single-photon ionization is possible already at low optical intensities and thus avoids molecular fragmentation caused by multi-photon ionization [104, 105, 106, 100].

The ionization potentials of most organic molecules are below $\sim$ 10 eV [107]. This corresponds to a photon wavelength of about 120 nm in vacuum, which falls into the vacuum ultraviolet (VUV) optical spectrum. Due to its ionizing power, absorption in air as well as standard optical glasses and crystals is high in the VUV and precludes the availability of commercial laser sources. Instead, light in this wavelength range must be guided in vacuum and can be generated by nonlinear optical frequency conversion in gases [108]. In this thesis, non-resonant third-harmonic generation (THG) in a xenon/argon mixture was employed to produce coherent radiation at 118 nm from a pulsed UV laser at 355 nm [109, 110, 104].

4.2 Theoretical background

Atomic gases exhibit a small third-order nonlinear susceptibility which can be exploited for four-wave mixing (FWM) at sufficiently large optical powers (for an overview, see [108]). FWM couples four optical waves and can be used to mix three input (pump) photons into one output (signal) photon. If one uses a single pump laser at frequency ν_1, FWM generates a signal field at the third harmonic frequency $\nu_3 = 3\nu_1$ by combination of three pump photons (see Fig. 4.1a). Alternatively, one can use two pump lasers with different frequencies to generate a signal at the sums or differences of their frequencies. This enables a tunable frequency of the generated signal field by tuning the frequency of one input field. In addition one can then exploit atomic resonances to enhance the conversion efficiency [108, 100]. However, since two input laser sources are required, the setup becomes more complicated. Consequently, for our purpose of VUV ionization, third-harmonic generation using a single UV pump laser is sufficient.

The combination of three pump photons into one signal photon is subject to both energy and momentum conservation. Energy conservation is simply given by the constraint $h\nu_3 = 3h\nu_1$ on the photon frequencies. Momentum conservation requires that the wave vectors $\vec{k}_1$ of the pump photons add up to the wave vector $\vec{k}_3$ of the signal photon (see Fig. 4.1b). The wave vector norms are $k_i = |\vec{k}_i| = 2\pi n_i/\lambda_i$ where $n_i = n(\nu_i)$ is the refractive index of the gas at the optical frequency ν_i. The experimental procedure of matching the sum of the pump wave-vectors to the signal wave-vector is called phase-matching and the phase mismatch is defined as

$$\Delta k = k_3 - 3k_1 = 2\pi\left(\frac{n_3}{\lambda_3} - \frac{3n_1}{\lambda_1}\right) = \frac{2\pi}{\lambda_3}(n_3 - n_1). \tag{4.1}$$

Consequently, the phase mismatch Δk is proportional to the difference $n_3 - n_1$ between the refractive indices of the gas at the VUV and UV frequencies. Proper phase matching is important to achieve constructive interference of the VUV photons emitted by all atoms in the focus of the UV pump laser.

Figs. 4.1b,c and d show cases of different phase mismatch $\Delta k < 0$, $\Delta k = 0$ and $\Delta k > 0$, respectively. It is clear, that a phase match in terms of the wave-vectors is only possible if $\Delta k \leq 0$. The phase-matching condition $\Delta k = 0$ is only optimal for a plane wave pump laser. In practice, the pump laser is strongly focused to a beam waist w_p. This enhances the optical intensity and thus the efficiency of the nonlinear process. In this geometry, in which the length of the focus, given by the confocal parameter $b = k_1 w_p^2$, is much shorter than the length of the gas cell, the phase-matching efficiency can qualitatively be evaluated in terms of the geometrical factor [109, 111, 108]

$$F = \begin{cases} (\pi \Delta k b)^2 e^{\Delta k b} & \Delta k < 0 \\ 0 & \Delta k \geq 0 \end{cases} \tag{4.2}$$

Consequently, optimal phase matching requires that $\Delta k < 0$ or $n_3 < n_1$ in the nonlinear medium. The maximum of F is achieved at $\Delta k b \approx -2$ [109, 111, 108].

In order to adjust the phase mismatch Δk to its optimal value $-2/b$ for a given UV focus, the refractive index difference $n_3 - n_1$ needs to be modified. In the configuration $\lambda_1 = 355$ nm and $\lambda_3 = 118$ nm, xenon gas already provides the correct sign $n_3 - n_1 < 0$

for phase matching due to a nearby optical resonance [110]. To fine-tune the refractive indices, one typically adds a second gas with $n_3 - n_1 > 0$. At $\lambda_3 = 118$ nm, a combination of xenon and argon is a common choice [112, 105, 106, 113, 114, 115]. The precise Xe:Ar mixing ratio depends on the confocal parameter and the precise pump frequency, but empirical ratios of Xe:Ar $\approx$ 1:10 are common.

The total output power of the third harmonic is given by [108]

$$P_3 \propto \rho^2 |\chi^{(3)}|^2 P_1^3 F \tag{4.3}$$

Here, ρ is the density of the atomic gas, $\chi^{(3)}$ is its nonlinear (third-order) susceptibility and P_1 is the pump-power. Clearly, P_3 depends quadratically on the atomic density and on the third power of the optical pump power. Hence, large densities and large pump powers are needed to improve the UV-to-VUV conversion efficiency P_3/P_1.

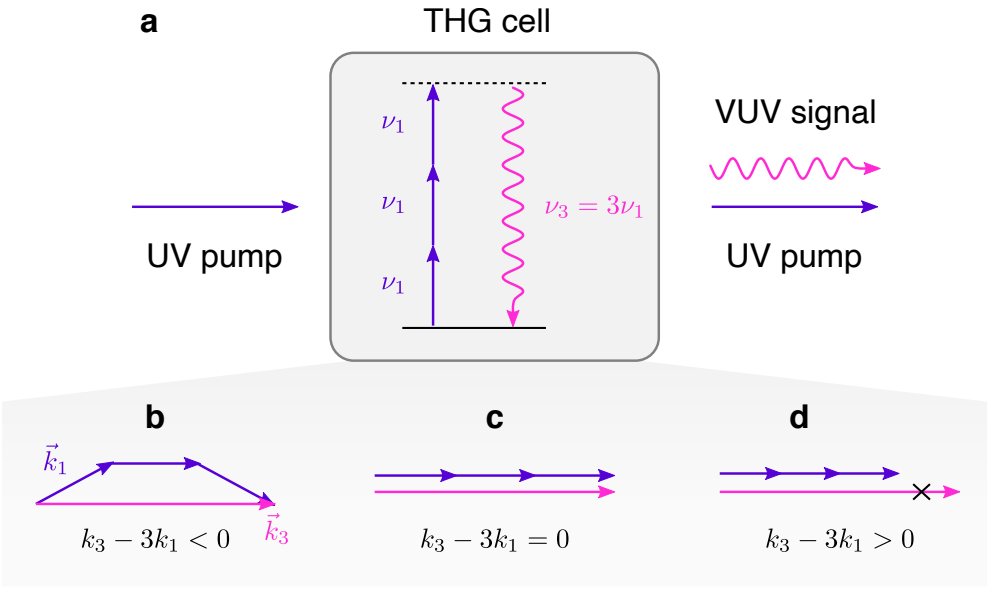

Figure 4.1: **Generation of VUV by THG. a**, schematic atomic level scheme of THG in which three UV photons with frequency ν_1 produce one VUV photon of frequency $\nu_3 = 3\nu_1$. This involves exciting the atom from the ground state to a virtual excited state (dashed line) and subsequent decay accompanied by emission of a VUV photon. **b**–**d**, different cases of phase-mismatch between the pump and signal photons. **b**, negative mismatch $\Delta k < 0$ is required for efficient THG in a focused beam. **c**, zero mismatch $\Delta k = 0$ is required in a collimated plane-wave geometry. **d**, positive mismatch $\Delta k > 0$ disallows THG.

4.3 Experimental setup

The experimental setup[1] for VUV generation and delivery of the VUV light to the experiment is depicted in Fig. 4.2a. The UV pump laser at $\lambda_1 = 355$ nm is a frequency-tripled Nd:YAG laser (Quantel Brilliant, pulse length 5 ns) with a repetition rate of 10 Hz and pulse energy adjustable up to 30 mJ. Using an anti-reflection coated UV-grade fused silica lens (Thorlabs, $f = 250$ mm), the beam is focused into the VUV cell from a diameter of 4 mm to a calculated waist of $w_p = 15$ μm.

The 30 cm long VUV cell is filled with a Xe:Ar gas mixture for optimization of the phase-matching, the total gas pressure is monitored on a pressure gauge. A slow flow of gas through the cell can be set up to improve stability of the VUV generation. VUV light is generated in the focus of the UV laser beam by THG and co-propagates with the UV light towards a magnesium fluoride lens (MgF_2, UV-grade, Thorlabs LA6008, $f = 200$ mm), which has an optical transmission of about 0.5 at 118 nm [116]. The beams hit the lens off-center and under a small angle of $\sim 2°$. Due to the different indices of refraction of MgF_2 at 355 nm and 118 nm, this deflects and separates the VUV from the UV beam in the subsequent beam line [105, 114, 115]. For alignment of the beam paths, the lens is mounted on a manual translation stage that can be actuated from the outside. For in-vacuum lubrication of the translation stage, APIEZON N vacuum grease is used, which is silicone free and does not creep onto the lens surface. By clamping the MgF_2

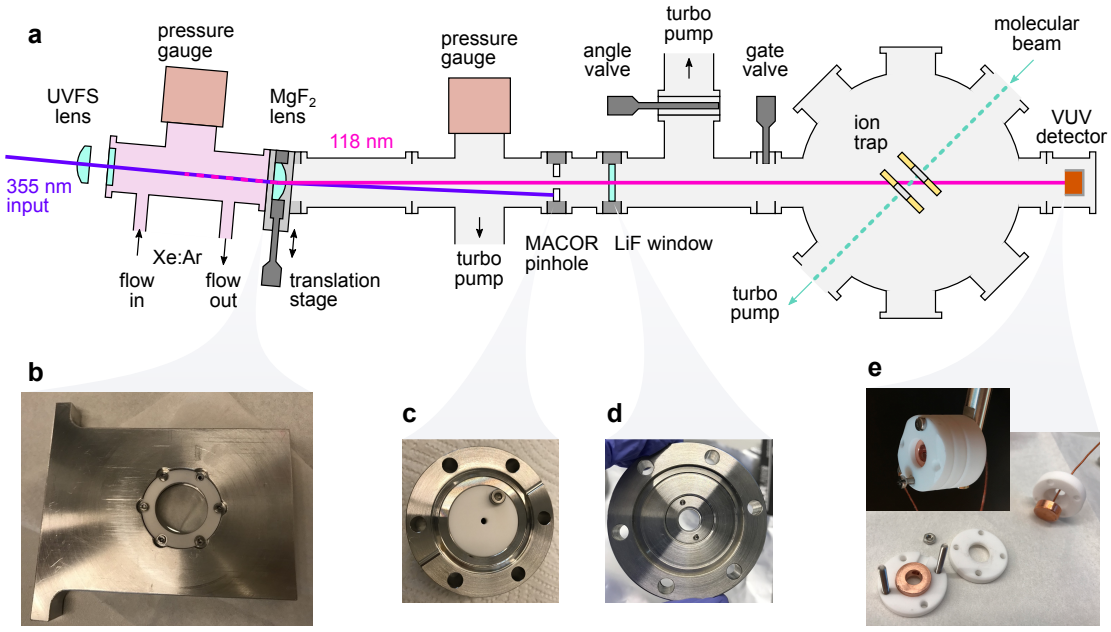

Figure 4.2: **Experimental setup for VUV generation.** **a**, Sketch of the experimental setup. **b**, Sledge mount for the MgF_2 lens. **c**, Pinhole of 3 mm diameter with MACOR cover. **d**, LiF window. **e**, VUV detector manufactured from two copper electrodes with MACOR spacers.

[1] Initial design by H. Gao.

lens using VITON O-rings, it also serves as a vacuum window between the VUV cell filled with the Xe:Ar mixture, and the subsequent VUV beam line held under vacuum (pressure $< 10^{-5}$ mbar). In various places, MACOR covers are installed to protect the borders of the lens, the VITON O-rings, as well as metal surfaces from the intense UV radiation at 355 nm (Fig. 4.2b). Evacuation of the VUV cell and the beam line is done using oil-free membrane and turbo pumps, respectively, to avoid contamination of the optics due to VUV-induced decomposition of hydrocarbons.

In the beam line after the MgF_2 lens, the collimated UV beam is blocked using a MACOR covered pinhole with aperture diameter of 3 mm. The VUV beam passes through the pinhole (Fig. 4.2c) and enters the main experiment vacuum chamber after transmission through a metal-sealed lithium fluoride (LiF) window (Fig. 4.2d). LiF is chosen here because of its wider optical transmission in the VUV down to $\sim$ 105 nm [116]. In order to facilitate exchange of the LiF window in case of damage or contamination, a gate valve is flanged between the LiF window and the main experiment chamber. The CF tube between the LiF window and the gate valve can be connected to a turbo pump by opening an all-metal angle valve for evacuation.

In the main experiment chamber, the VUV beam gets weakly focused to a waist of about 100 μm at the position of the ion trap, which is located at a distance of 82 cm from the MgF_2 lens. Afterwards, it impinges on an in-vacuum VUV detector constructed from two copper electrodes held by a MACOR spacer (Fig. 4.2e). A bias voltage of 1 kV is applied across the two electrodes and the VUV induced photocurrent is measured across a 50 Ohm resistance on an oscilloscope.

Alignment of the VUV beam line is aided by a home-made ray-tracing simulation of the UV and VUV beam paths (Fig. 4.3). In Figs. 4.3a and b, rays of VUV and UV light are traced from the Xe:Ar cell through the VUV beam line for different transverse displacements of the MgF_2 lens. The UV focus in the Xe:Ar cell is located 125 mm in front of the MgF_2 lens. The propagation axis of the incident UV light is tilted by 2° relative to the axis connecting the MgF_2 lens and the ion trap and hits the MgF_2 lens off-center. Due to the different indices of refraction in the UV and VUV (n(118 nm) = 1.68, (n(355 nm) = 1.39 [117]), the MgF_2 lens acts like a prism and deflects the UV and VUV beams under different angles. Precise adjustment of the transverse lens position Δx using the translation stage allows either the VUV light to be transmitted to the ion trap (Fig. 4.3a) or instead the UV light (Fig. 4.3b). Moreover, the VUV light gets re-focused after passing through the lens, while the UV light remains slightly divergent, preventing damage to the pinhole where it is blocked. At the pinhole, the beam centers have a transverse displacement of about 6 mm in Fig. 4.3a.

Initial alignment of the VUV beam line is achieved by sending a 397 nm cw laser beam backwards through the system from the ion trap to the VUV cell. For this purpose, the VUV detector can be moved out of the way. During this alignment at 397 nm, the MgF_2 lens is shifted to the configuration shown in Fig. 4.3b that allows the 355 nm beam (at low power) to be transmitted through the pinhole. After this coarse alignment, the MgF_2 lens is fully centered ($\Delta x = 0$) and the power in the 355 nm beam is raised to enable THG. Slowly moving the translation stage then allows one to find to the position $\Delta x = 3.8$ mm of Fig. 4.3a, where the 355 nm beam is blocked while the VUV passes through the pinhole and reaches the VUV detector. After this coarse alignment using the translation stage, fine alignment of the VUV beam is achieved using an xy-translation

stage that laterally moves the UVFS lens in front of the VUV cell. At any stage, care must be taken that the UV beam does not pass through the pinhole at full power to avoid damaging the LiF window.

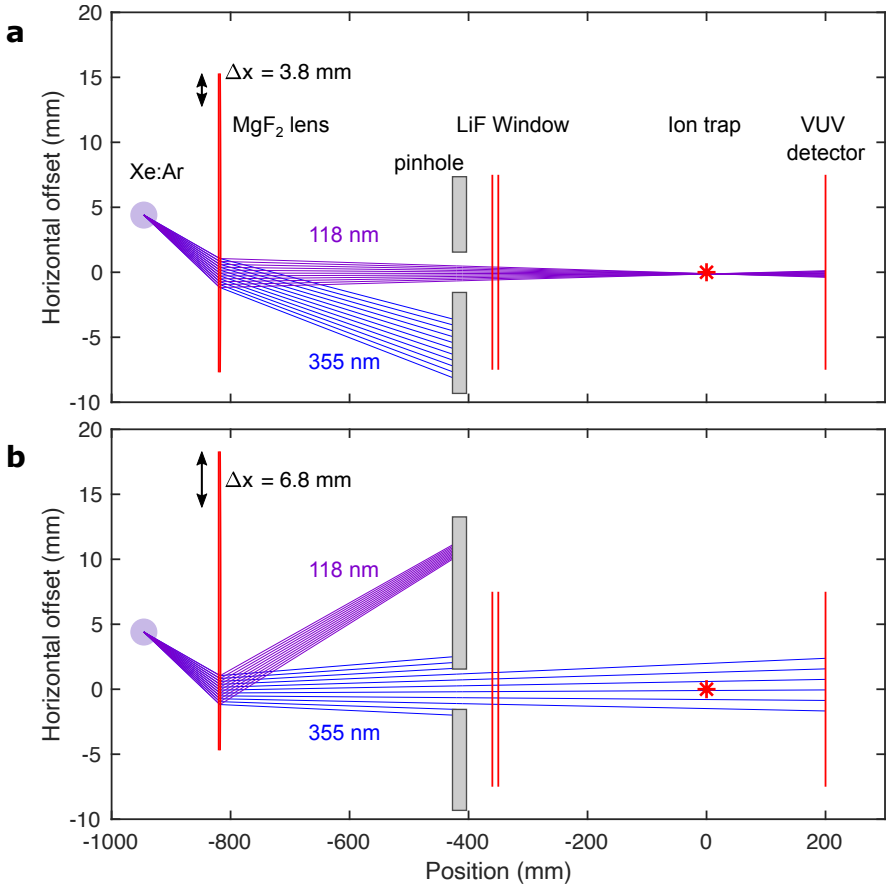

Figure 4.3: **Ray tracing simulation of UV and VUV. a**, MgF_2 lens position to allow VUV transmission to the ion trap. UV light is blocked at the pinhole. **b**, Further displacement of the MgF_2 lens allows the UV light to be transmitted through the pinhole. This setting is used for pre-alignment. The red star marks the position of the ion trap.

4.4 Characterization

4.4.1 Phase-matching

The first step towards finding good working parameters for VUV generation was the optimization of phase matching. For this purpose, the composition of the Xe:Ar gas mixture in the VUV cell was varied. The different curves of Fig. 4.4a show the VUV detector signal at different Xe partial pressures of 11, 20, 30 and 40 mbar. Ar gas was gradually added to the VUV cell to change the Xe:Ar mixing ratio. The total Xe+Ar pressure is given on the horizontal axis. Example VUV detector traces for different total pressures at a Xe partial pressure of 30 mbar are shown in Fig. 4.4b. In each curve of Fig. 4.4a, the VUV signal first rises with increasing total pressure, reaches a peak and then drops sharply. The optimal Xe:Ar ratio at which the peak VUV signal occurs is found to be about 1:11, independent of the total Xe+Ar pressure. This ratio for optimal phase-matching is consistent with other experiments [113, 114, 115]. In terms of the total Xe+Ar pressure, the peak VUV yield at optimum phase-matching is largest for intermediate pressures of 250 and 370 mbar, and decreases again for larger pressure, potentially due to absorption within the gas or additional nonlinear effects [108].

To interpret the individual curves of Fig. 4.4a, it is noted that the total Xe+Ar pressure on the x-axis directly relates to the phase mismatch Δk. In the gas mixture, the total refractive index n of the gas is the sum of the refractive indices of its components Xe and Ar, i.e. $n = n^{(\mathrm{Xe})} + n^{(\mathrm{Ar})}$. The refractive index of each component is proportional to its partial pressure, i.e. $n^{(\mathrm{Xe})} \propto p^{(\mathrm{Xe})}$ and $n^{(\mathrm{Ar})} \propto p^{(\mathrm{Ar})}$. At $\lambda_3 = 118$ nm, Xe gas has a negative refractive index difference $n_3^{(\mathrm{Xe})} - n_1^{(\mathrm{Xe})} < 0$, while for Ar $n_3^{(\mathrm{Ar})} - n_1^{(\mathrm{Ar})} > 0$ [110]. Consequently, adding Ar to the Xe gas tunes the value of the phase mismatch $\Delta k \propto n_3 - n_1$ from negative to positive values. In each curve, the location of the peak corresponds to the optimum phase-matching condition $\Delta k = -2/b$ and $\Delta k = 0$ is reached after the sharp drop in VUV signal at higher total pressures. The shapes of the individual curves and their asymmetry about the peak resemble the phase-matching efficiency function F from equation (4.2).

4.4.2 Efficiency

With optimum phase-matching conditions identified, the VUV conversion efficiency and its dependence on the UV pump power were characterized. Measurements of the VUV signal as a function of the UV pulse energy E_1 are shown in Fig. 4.5a. Individual VUV detector traces are displayed in Fig. 4.5b. From equation 4.3, a cubic dependence of the VUV pulse energy $E_3 \propto E_1^3$ on the pump laser pulse energy E_1 is expected. Consequently, the data were fitted using the function $y = aE_1^3 + b$ with scaling parameter a and detector offset b. The fit is plotted as the red line in Fig. 4.5a and agrees well with the data points, confirming the cubic relationship between pump and signal powers.

An estimate of the UV-to-VUV conversion efficiency was calculated in the following way [115]. Incident VUV light on the VUV detector generates a photocurrent I that is measured across a 50 Ohm resistance on an oscilloscope, resulting in the detector traces shown in Fig .4.4b with peak voltage of about 1 V. The detection efficiency of the copper photocathode is estimated to be $\eta_{\mathrm{det}} = 10^{-2}$ [118] and the total VUV transmission from the Xe:Ar cell to the detector is approximately given by $\eta_{\mathrm{tr}} = 0.5^2 = 0.25$. From the

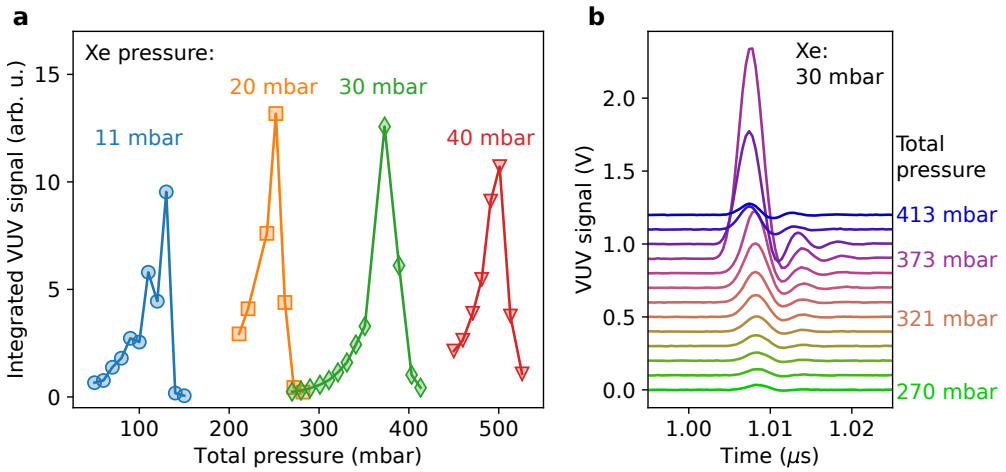

Figure 4.4: **Phase matching.** **a**, VUV signal as a function of the total Xe + Ar pressure at fixed Xe pressures. This varies the Xe:Ar mixing ratio and tunes the phase mismatch. **b**, Selected VUV signal traces at Xe pressure equal to 30 mbar. The traces are vertically offset for clarity.

measured peak photocurrent $I = 1\text{V}/50\Omega$ and laser pulse length $\tau = 5$ ns, the VUV energy per pulse is calculated to be

$$E_3 = \frac{I}{\eta_{\text{det}}\eta_{\text{tr}}}\frac{h\nu_3}{e}\tau \approx 0.4\ \mu\text{J} \tag{4.4}$$

Here, e is the elementary charge and h is the Planck constant. This corresponds to a VUV photon number of about $E_3/(h\nu_3) \approx 3\times10^{11}$ per pulse. With a UV pump power of $E_1 = 30$ mJ, this gives a conversion efficiency of $E_3/E_1 \approx 1\times10^{-5}$, which is comparable with the values achieved in other works [113, 115].

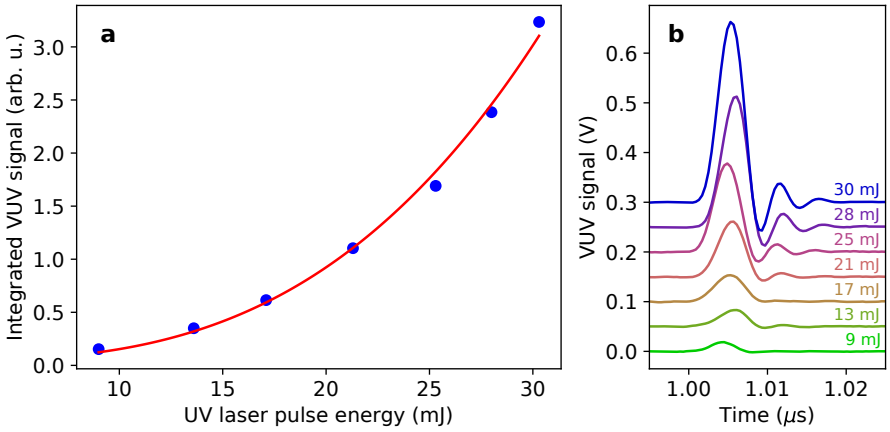

Figure 4.5: **VUV generation efficiency as function of UV pump power.** **a**, VUV signal counts as a function of the UV laser pulse energy. **b**, oscilloscope traces of the VUV detector signal for the data in **a**. The traces are vertically offset for clarity.

4.4.3 Stability

An important requirement for application of the generated VUV light in experiments is to achieve continuous stable operation. This depends on a number of parameters. Optical transmission between the Xe:Ar cell and the main experiment chamber has to be maintained over extended periods of time without degradation of the optics. Possible causes of damage to the MgF_2 lens and the LiF window are: Too strongly focused UV pump light can directly damage the optics. The optic material can degrade due to color-center-formation [119] if the material quality is not of VUV grade. Finally, contamination of the vacuum with trace amounts of oil coming from the vacuum pumps or other hydrocarbons can lead to VUV-induced decomposition and deposition of opaque layers on the optical surfaces [120].

In Fig. 4.6, the VUV detector signal is measured as a function of the total time of operation. The blue circles show the measured VUV signal during an early stage of the experiment, when a rotary vane pump was used to evacuate the VUV beam line. A rapid exponential decrease of the VUV signal is observed within 10 minutes. The origin of this decay was identified as pump oil contamination of the vacuum. Upon irradiation with VUV, this led to a local surface degradation of the LiF window (shown in the inset) which gradually reduced the optical transmission and was impossible to clean using standard solvents.

As a solution, a turbo pump backed by a membrane pump was installed for evacuation of the VUV beam line. Moreover, silicone grease that had initially been used to lubricate the translation stage for the MgF_2 lens was replaced by Apiezon N grease, which is not

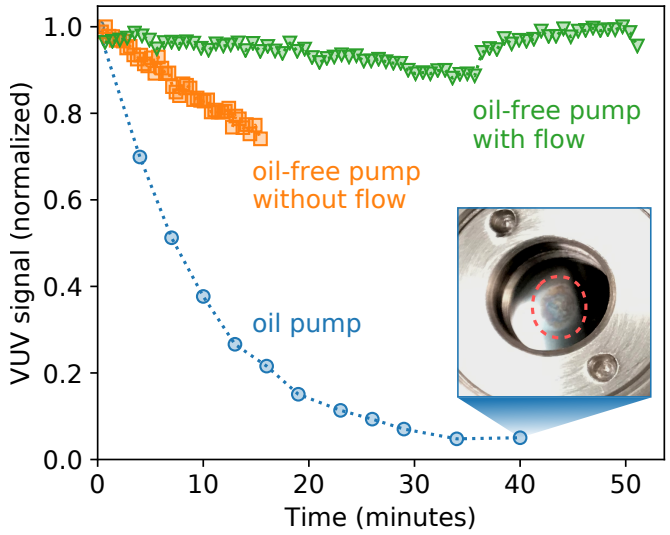

Figure 4.6: **VUV signal stability.** Normalised VUV detector signal as a function of the exposure time to VUV. The blue circles correspond to the situation where the VUV beam line was evacuated using an oil pump. The inset image applies to this case and shows vitrified hydrocarbon contamination on the LiF window, which caused the drop in VUV signal. The other curves correspond to using an oil-free pump with gas flow through the Xe:Ar cell (green triangles) or no flow (orange squares).

prone to creeping along surfaces and has a very low vapour pressure of 6×10^{-10} mbar at room temperature. With these changes the VUV signal was found to be more stable (orange squares in Fig. 4.6). However, the life time was still limited to about 30 minutes. This is due to depletion of Xe and Ar by multi-photon ionization in the UV and VUV focus [121].

In order to achieve long-term stability, a constant flow of the Xe:Ar gas mixture through the VUV cell had to be implemented (green data points in Fig. 4.6). For this purpose, the VUV cell was connected to a gas bottle with the Xe:Ar mixture on one side and a membrane vacuum pump on the other side. Needle valves in both lines allowed the control of a slow flow through the cell, while keeping the cell pressure level at the optimum value for maximum THG efficiency. With this improvement, the generated VUV power delivered to the main experiment was stable for hours of operation.

An additional measure to secure long-term stability was the integration of a mechanical shutter into the UV laser beam path. This shutter was remotely controlled from the experiment control software using a microcontroller (Arduino) and was opened only when VUV is needed for the experiment. This minimized the overall exposure of the setup to UV and VUV radiation.

4.4.4 VUV-induced ionization

A final characterization step was to test VUV-induced photoionization of molecular samples. The ionization potentials (IP) of selected molecules used in this work are given in table 4.1, all below the photon energy 10.5 eV of the generated VUV.

Fig. 4.7 contains three TOF-MS traces obtained by VUV ionization. To measure these spectra, the TOF-MS pulse was synchronized with the Nd:YAG laser pulse via a pulse generator. The lowest trace in blue color shows the signal when propene is leaked into the main experiment chamber using a leak valve at a partial pressure of $\sim 10^{-9}$ mbar. A single peak belonging to the parent $C_3H_6^+$ ion is observed without any fragment ions or clusters. When propene was ionized from a molecular beam (5% in neon, 3 bar, pulse width 200 μs), a series of smaller peaks appear at longer time of flight / larger mass next to the parent ion signal (orange curve). These peaks can be attributed to protonated propene clusters $(C_3H_6)_nH^+$ with $n = 2, \ldots, 6$. Characteristic for these cluster signals is that their intensity peaks at $n = 4$. Similar peaked distributions of cluster ion signals were observed for molecular beams of methanol and ethanol ionized by VUV [113]. If instead the same molecular beam was ionized using fs laser pulses at 775 nm (see Fig. 4.8a) the distribution of observed cluster peaks changed dramatically. In this case, almost no parent ion was observed and the dominant peak was due to the protonated monomer (Fig. 4.8b). The signal strength of larger clusters then decreased

Table 4.1: Ionization potentials of selected molecules.

Name	sum formula	IP (eV)	ref.
Propene	C_3H_6	9.69	[107]
Acetone	C_3H_6O	9.68	[107]
Cyclohexane	C_6H_{12}	9.81	[107]
2,3-dibromobutadiene (DBB)	$C_4H_4Br_2$	9.12 (calc.)	[96]

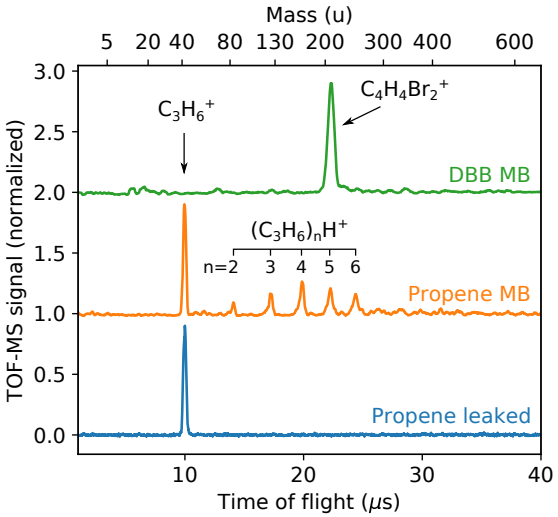

Figure 4.7: **TOF-MS traces using VUV photoionization.** All traces are normalized and vertically offset for clarity. Bottom: propene leaked to the chamber. Middle: propene from a molecular beam, showing series of clusters signals. Top: DBB from a molecular beam.

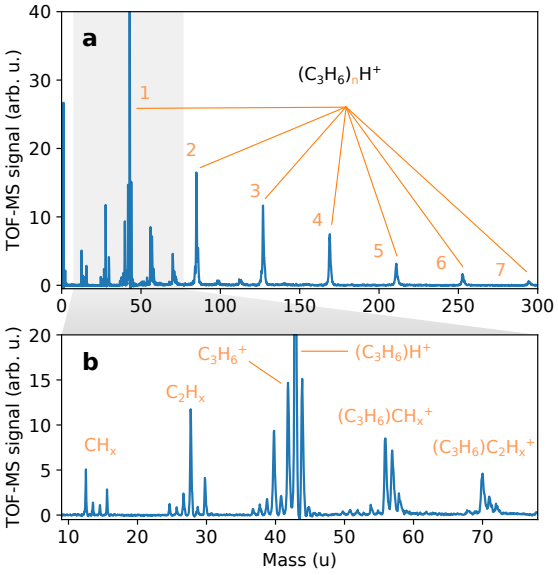

Figure 4.8: **TOF-MS of propene using fs laser pulse ionization. a**, Overview of the mass spectrum. The series of peaks is due to propene clusters $(C_3H_6)_nH^+$ with $n = 1, \ldots 7$ visible here. In total, clusters up to a mass of 700 u were observed. **b**, Magnified view around the dominant peak. The strongest peak at 43 u is due to the $(C_3H_6)H^+$ protonated monomer while the parent ion peak at 42 u is suppressed. Different side peaks to the left and right correspond to subtraction and addition of up to two C-atoms from the monomer, respectively.

exponentially with the number n of monomers. In addition a range of fragment peaks were observed (Fig. 4.8b). These effects can be explained by the fundamentally different mechanisms of single-photon and multi-photon ionization. While VUV selectively ionizes the parent molecule, high-intensity multi-photon ionization predominantly affects the weakly-bound clusters and leads to fragmentation.

Finally, the green trace of Fig. 4.7 shows VUV-ionization of 2,3-dibromobuta-1,3-diene (DBB) from a molecular beam ($\sim 0.1\%$ in neon, 3 bar, pulse width 200 μs). In this spectrum only the parent ion peak at 212 u is observed. Clusters or fragment ion peaks are absent in the data, in contrast to multi-photon ionization using fs laser pulses (see chapter 5). For DBB, cluster formation might be suppressed in part due to its low vapour pressure, resulting in a lower beam density compared to propene. In the case of water, the amount of clusters present in the molecular beam was also found to depend on the carrier gas (see chapter 2). In other measurements (see appendix Fig. A.2), VUV was successfully used to ionize acetone leaked into the TOF-MS chamber as well as cyclohexane from a molecular beam, both without visible fragmentation.

4.5 Conclusion

In this chapter, an experimental setup to produce VUV radiation at 118 nm by non-resonant third harmonic generation in a phase-matched Xe:Ar gas mixture has been presented. Under typical conditions, a UV-to-VUV conversion efficiency of 10^{-5} is achieved. The apparatus delivers VUV pulses with stable power and sufficient intensity for soft photoionization in the TOF-MS. The generated radiation allows ionization of molecules with ionization energy < 10.5 eV. This capability has been demonstrated for propene, dibromobutadiene, acetone and cyclohexane. In comparison to multi-photon ionization using fs laser pulses, single-photon ionization in the VUV produces significantly less fragment ions [104, 122, 105, 99]. Consequently, the VUV source is an important tool for the mass spectrometric characterization of molecular beams. In this work, the generated VUV light was used to ionize DBB in a molecular beam without fragmentation. This allowed the characterization of the electrostatic deflection of the two DBB conformers (see chapter 5). In addition, the VUV light was used to ionize propene molecules leaked into the experiment chamber and load them into the ion trap (see chapter 7). They were subsequently used as ionic reactants for reaction experiments with a conformer-controlled molecular beam of DBB (see chapter 8).

5

Separation of the conformers of 2,3-dibromobuta-1,3-diene

The Diels-Alder cycloaddition, in which a diene reacts with a dienophile to form a cyclic compound, counts among the most important tools in organic synthesis. Achieving a precise understanding of its mechanistic details on the quantum level requires new experimental and theoretical methods. Here, we present an experimental apparatus that separates the different diene conformers in a molecular beam. This enables the investigation of their individual cycloaddition reaction kinetics and dynamics under single-collision conditions in the gas phase. A low- and high-level quantum-chemistry-based screening of more than one hundred dienes identified 2,3-dibromobutadiene (DBB) as an optimal candidate for efficient separation of its *gauche* and *s-trans* conformers by electrostatic deflection. A preparation method for DBB was developed which enabled the generation of dense molecular beams of this compound. The theoretical predictions of the molecular properties of DBB were validated by the successful separation of the *gauche* and *s-trans* conformers of DBB in the molecular beam. A marked difference in photofragment ion yields of the two conformers upon femtosecond-laser pulse ionization was observed, pointing at a pronounced conformer-specific fragmentation dynamics of ionized DBB. Our work sets the stage for a rigorous examination of mechanistic models of cycloaddition reactions under controlled conditions in the gas phase.

The content of this chapter has been published in [33].

5.1 Introduction

Besides polar and radical reactions, pericyclic processes are one of the three fundamental reaction types that form the basis of synthetic organic chemistry. Given their great significance in organic synthesis, rigorously defined mechanistic pathways are an important resource for reaction developers. The Diels-Alder cycloaddition [24], in which a diene and a dienophile react to form a cyclic product, is a practical and widely used pericyclic reaction in organic synthesis. While the broad strokes of its mechanism are well understood, the detailed reaction manifold for any given substrate is often extensively discussed [26, 123, 28, 124, 125, 126]. Given its mechanistic subtleties and its importance,

the Diels-Alder reaction has served as a test-bed for establishing new types of mechanistic analysis [127]. In case of the "canonical" concerted pathway, which involves a cyclic transition state and is widely discussed in the literature [26, 123, 28, 124, 125, 126], only the *s-cis* conformer of the diene reacts to form the cyclic product – while in a stepwise mechanism also the *s-trans* conformer can contribute to the reaction. Stepwise pathways become particularly important for ionic variants of the reaction, i.e., polar cycloadditions, for which traditional concepts for rationalizing the mechanism such as the conservation of orbital symmetry break down [32, 28, 128, 126]. Thus, an experimental investigation of the mechanistic impact of individual rotamers is clearly warranted. This, however, requires a way to probe the reactivities of the individual conformers of a specific diene, a difficult task under standard liquid-phase reaction conditions.

In recent years, molecular beams have become an important tool for the investigation of gas-phase chemical reaction dynamics under highly controlled conditions[6, 9]. In particular, the use of inhomogeneous electric fields has enabled the electrostatic deflection and thus spatial separation of different molecular conformers and isomers according to their different electric dipole moments[12, 10, 14, 13, 21]. The combination of such a "controlled" molecular beam with a stationary reaction target of sympathetically cooled molecular ions in an ion trap forms a powerful tool for studies of the kinetics and dynamics of ion-molecule reactions [13, 72, 9, 21]. Recently, this approach has enabled the measurement of individual chemical reactivities of the *cis* and *trans* conformers of 3-aminophenol with trapped Ca^+ ions [13, 72] and of the two nuclear-spin isomers of water [15] toward trapped diazenylium ions (N_2H^+) in a proton-transfer reaction [21]. Consequently, molecular beams in conjunction with ion traps offer a direct and precise way to measure conformer-specific rate constants and thus to investigate the reaction mechanism of polar cycloadditions. The key challenge is the identification of suitable model systems amenable to a characterisation under these specific experimental conditions. In the present context, this means that (i) both reactants, the diene and the dienophile, need to be volatile enough to enable their preparation in the gas phase, (ii) the energy difference between the *s-cis* and *s-trans* conformers of the diene needs to be small enough so that both can be populated in the cold environment of a supersonic molecular beam, and (iii) the difference of their permanent dipole moments in the molecular frame needs to be large enough to enable their efficient electrostatic separation [13, 6].

The selection of an optimal model system is, therefore, a multi-dimensional optimization problem. Traditionally, the choice would be guided by chemical and physical insight. Nowadays, numerical simulations of reactions can provide meaningful atomistic insights to support experimental efforts [129]. In the context of designing experiments, virtual screening has proven to be a powerful approach for suggesting compounds matching the physical and chemical properties of interest. Computational screening has already been successfully applied in protein, materials and catalytic design [130, 131, 132]. Here, we apply this approach to identify optimal dienes suitable for controlled gas-phase polar cycloaddition reactions.

This work combines methods of theoretical, organic, and physical chemistry to lay the foundations for a subsequent experimental characterization of conformational effects in polar cycloaddition reactions. Quantum-chemical calculations were performed to screen the reactant space for a diene with physical properties optimized toward its use in conformer-selected reaction-dynamics experiments in the gas phase. A synthesis for the

theoretically identified optimal diene, 2,3-dibromobutadiene (DBB), was then developed. Finally, the physical properties of the compound were validated in a molecular-beam experiment separating the two conformers by electrostatic deflection.

5.2 Theoretical and experimental methods

5.2.1 Theoretical screening

We applied the concept of computational screening[1] towards the problem of exploring chemical space from first principles [133] in order to find a polar diene for conformer-selective Diels-Alder cycloadditions. The chemical role of polar dienes in Diels-Alder reactions was already explored computationally in various preceding studies, see, e.g., references [134, 128]. Efficient electrostatic separation necessitates a certain difference in electric dipole moments $\Delta\mu$ between the *s-cis* and *s-trans* conformers of the diene [46, 6]. Moreover, a small energy difference ΔE between the ground states of the conformers is required to ensure a significant thermal population of both species in the molecular beam. For a successful experiment, a suitable diene has to be identified which satisfies both of these conditions.

High-throughput based virtual design of novel compounds typically starts from an initial scaffold, which can easily be modified at multiple sites through functionalization by substituting atoms or functional groups [135]. Theoretical screening then yields the best mutated combinations selected according to their proximity to the desirable physical or chemical target-property values.

In the present work, we computationally searched the chemical space of butadiene derivatives for which the *s-cis* and *s-trans* isomers exhibit maximal and minimal differences in dipole moments and energies, respectively. Substituting CH_2 in positions 1 and 4 by NH, or O, and substituting the hydrogen attached to carbon in position 2 and 3 by halogens (F, Cl, Br, I), a preliminary density functional theory (DFT) based scan of 144 candidates, not accounting for symmetrically redundant species, resulted in the identification of di-halogen substituted butadiene as a promising series of candidates for experiments. Due to the chemical reactivity of iodine-substituted compounds, potentially hampering subsequent synthetic efforts, we have only included the difluoro, dichloro, and dibromo 2,3-substituted butadienes for further in-depth theoretical analysis.

Torsional energy profiles were subsequently calculated for all three species using DFT with the double-hybrid functional DSD-PBEP86-D3BJ[136] and a large basis set (def2-QZVPP)[137] which was previously shown to give good performance for the prediction of torsional potential energy surfaces of similar molecules[138]. For the torsional profiles, the geometry optimizations were restricted by keeping the torsional angle $\Theta = \Theta_{H_3C-CC-Y}$ constant, imposing achirality. The entire range of $0° < \Theta < 180°$ was scanned in steps of $\Delta\Theta = 20°$. Note that due to the applied constraints for the torsional angles throughout the geometry optimization, the torsional profile is symmetric $[E(360° - \Theta) = E(\Theta)]$. Calculations were carried out with the Gaussian09 program package [97].

[1] The theoretical screening described here was performed by D. Tahchieva and R. Ramakrishnan in the group of Prof. O. A. von Lilienfeld.

5.2.2 Stark-energy and trajectory simulations

To theoretically assess the behaviour of DBB in an electrostatic deflection experiment, Stark energies and effective dipole moments of individual rotational states of DBB were calculated using the CMIstark software package[49]. The calculated rotational constants and dipole moments as listed in Table 5.2 were used as input parameters. The Stark energies served as input parameters for simulating state-specific deflection profiles of the molecular beam by the electrostatic deflector with a home-made software package based on CMIfly [6].

Trajectory simulations were carried out for *gauche*-DBB with 10^5 molecules for each rotational state up to a maximum rotational quantum number of $j_{\max} = 20$. For the unpolar *s-trans*-DBB, only a single quantum state, $j = 0$, needed to be simulated with a total number of 10^6 trajectories. In all cases, initial positions were uniformly sampled across the cross section of the orifice of the gas nozzle generating the molecular beam. The initial velocities of the molecules were sampled from a normal distribution. The velocity distribution was matched to the experimentally determined mean longitudinal velocity of 843 m/s with a longitudinal velocity spread of 10 % (see section 2.4.4.1). A transverse velocity spread of 4 m/s was chosen to match the divergence of the beam to the acceptance angle of the skimmers in the assembly. According to the theoretical energy difference between the ground states of *gauche*- and *s-trans*-DBB in Table 5.2, the ratio of their thermal populations at room temperature is $p_{\text{gauche}}/p_{\text{trans}} = 0.30$, taking into account the two-fold degeneracy of the *gauche* structure, see Fig. 5.4. This ratio was used to scale the simulated deflection profiles of the two species.

In order to calculate thermally averaged deflection profiles $n_{\sigma,T}(y)$ for each conformer ($\sigma \in \{gauche, s\text{-}trans\}$) at a specific rotational temperature T, we followed a similar procedure as before [46, 21]. For each rotational quantum state $|j_{K_a K_c} M\rangle$, histograms of the arrival positions $n_{\sigma j_{K_a K_c} M}(y)$ normalized by the initial sample size were extracted from the simulated trajectories. Here, j is the quantum number for overall angular momentum neglecting nuclear spin, i.e., for the overall rotation, K_a and K_c are pseudo-quantum numbers for the projection of the angular momentum onto the molecular axes, and M is the quantum number for the projection of the rotational angular momentum onto the external-field axis. Thermal averaging was performed using the relation

$$n_{\sigma,T}(y) = \frac{p_\sigma}{Q_\sigma} \sum_{j=0}^{j_{\max}} \sum_{K_a,K_c} \sum_{M=0}^{j} g_M e^{-E_{j_{K_a K_c}}/k_B T} \, n_{\sigma j_{K_a K_c} M}(y), \tag{5.1}$$

with the rotational partition function

$$Q_\sigma = \sum_{j=0}^{j_{\max}} \sum_{K_a,K_c} \sum_{M=0}^{j} g_M e^{-E_{j_{K_a K_c}}/k_B T}. \tag{5.2}$$

Here, k_B denotes the Boltzmann constant, p_σ are the populations of the conformers at room temperature and $E_{j_{K_a K_c}}$ are the field-free rotational energies. The degeneracy factor g_M takes values $g_M = 1$ for $M = 0$ and $g_M = 2$ for $M > 0$. The total thermal deflection profile was calculated from the sum of the deflection profiles of the *gauche*- and *s-trans*-conformers,

$$n_{\text{tot,T}}(y) = n_{gauche,T}(y) + n_{s-trans,T}(y). \tag{5.3}$$

5.2.3 Synthesis of DBB

Since DBB is an unstable compound which is not commercially available, a synthetic route needed to be devised that delivered the material in sufficiently high purity and quantity for molecular-beam experiments. Prior to this work, Stewart Jr. et al. [139] reported a synthesis of DBB from 1,4-dihalo-2-butyne and a cuprous halide which formed activated halide ions present in solution. DBB was obtained through continuous distillation during the reaction. After extensive screening of potential conditions, it was found[2] that the elimination reaction of 1,2,3,4-tetrabromobutane (TBB) with the sterically hindered base 1,8-Diazabicyclo[5.4.0]undec-7-ene (DBU) primarily delivered the elimination product DBB (see Fig. 5.1). The most effective conditions involved adding DBU to a solution of TBB in diethyl ether under a constant stream of nitrogen, with NaI as an additive to accelerate the substitution. Under these conditions, near complete conversion to DBB was observed after 1 hour of reaction time. The purified sample was directly used in the molecular beam apparatus. Further information on the synthesis can be found below.

Materials and methods:
Diethyl ether and sodium iodide were purchased from Sigma-Aldrich. 1,8-Diazabicyclo[5.4.0]undec-7-ene was purchased from Alfa Aesar. 1,2,3,4-tetrabromobutane was purchased from TCI-chemicals. All reagents were used without further purification. Chloroform for NMR measurements was purchased from Cambridge Isotope Laboratories. All ^{1}H and ^{13}C NMR spectra were recorded on a Bruker Avance III (HD)NMR instrument operated at 400 MHz and 101 MHz, respectively. Chemical shifts (δ) are reported in parts per million (ppm) relative to residual solvent peaks.

Synthetic route:
In a 500 ml three-neck round bottom flask 1,2,3,4-tetrabromobutane (12.0 g, 32.12 mmol, 1 eq) were suspended in diethyl ether (150 ml, extra pure, stabilized with BHT). Sodium iodide (9.64 g, 64.24 mmol, 2 eq., anhydrous $>$ 99.5 %) was added to the suspension. A flow of nitrogen was continuously passed through the flask during the entire operation. By making use of a dropping funnel, 1,8-Diazabicyclo[5.4.0]undec-7-ene (19.2 ml, 1.29 mol, 4 eq.) was slowly added to the suspension (see Fig. 5.2a). During the addition the formation of a dense yellow suspension was observed. The dropping funnel was rinsed

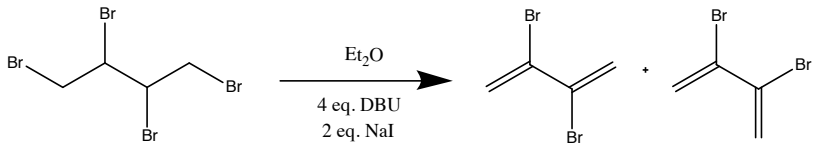

Figure 5.1: **Scheme of the synthesis of 2,3-dibromobutadiene.**

[2]The synthetic route described here was developed by D. Bachmann in the group of Prof. D. Gillingham.

with diethyl ether (30 ml) and the reaction mixture was allowed to stir for 1 hour. Then, the precipitate was filtered off over a frit and was washed with diethyl ether (3×20 ml). The organic phase was washed with saturated ammonium chloride (3×100 ml), distilled water (1×100 ml), and brine (1×100 ml)(see Fig. 5.2b). The organic phase was dried with $MgSO_4$ and concentrated using a rotatory evaporator at 0 °C and reduced pressure to yield the crude product DBB (3.74 g, 55 %). Two methods to purify the crude product were tested. First, column chromatography was conducted under a nitrogen atmosphere. Here, silica gel was used as the stationary phase and a mixture of pentane and diethyl ether (10:1) as the mobile phase (see Fig. 5.2c). Second, a Schlenk technique distillation at cold temperatures (−5 °C to 5 °C) and reduced pressures (4 mbar) was employed. The DBB vapours were condensed in a Schlenk flask that was immersed in a liquid nitrogen bath (see Fig. 5.2d). Both methods resulted in an equivalent product purity. The second method, however, was found to be more cost effective. The purified product was observed to react violently with excessive heat formation when in contact with air at room temperature. In order to prevent the sample from degradation and self-polymerization, it was stored below −78 °C. A ^{1}H NMR spectrum of the reactant and the product can be found in Fig. A.3 of appendix A.3.

^{1}**H NMR** (400 MHz, CDCI3) δ 6.43 (d, $J = 1.5$ Hz, 2H), 5.89 (d, $J = 1.5$ Hz, 2H)
^{13}**C NMR** (101 MHz, CDCI3) δ 125.13, 124.75

Figure 5.2: **Synthesis of DBB and clean-up procedure. a**, Batch reaction. **b**, Washing of the organic phase through extraction. **c**, Purification through column chromatography. **d**, Schlenk line distillation.

5.2.4 Experimental setup for conformer separation

A schematic of the experiment is depicted in Fig. 5.3. Details of the experimental setup are described in chapter 2 and earlier work [13, 72, 61, 21]. A supersonic jet of DBB seeded in neon was generated using a pulsed gas valve and passed through two skimmers before entering the electrostatic deflector (see section 2.4.4). The resulting molecular beam contained a mixture of the *gauche* and *s-trans* conformers of DBB. The inset of Fig. 5.3 depicts the inhomogeneous electric field in the deflector with a cross marking the nominal molecular beam axis. Here, the two conformers were angularly dispersed and thus spatially separated according to their different dipole moments [6]. Behind the deflector, the molecular beam was directed at a linear-quadrupole ion-trap (LQT) coupled to a time-of-flight mass spectrometer (TOF-MS). The entire molecular beam setup can be tilted vertically with respect to the TOF-MS, which allows probing different regions of the dispersed molecular beam. The tilting angle thus defines a deflection coordinate y. When entering the TOF-MS, the DBB molecules were ionized by either pulsed vacuum-ultraviolet (VUV) radiation (for details see chapter 4) or femtosecond (fs) laser pulses (see section 2.2) and accelerated onto a microchannel-plate detector (MCP) using high-voltage electrodes.

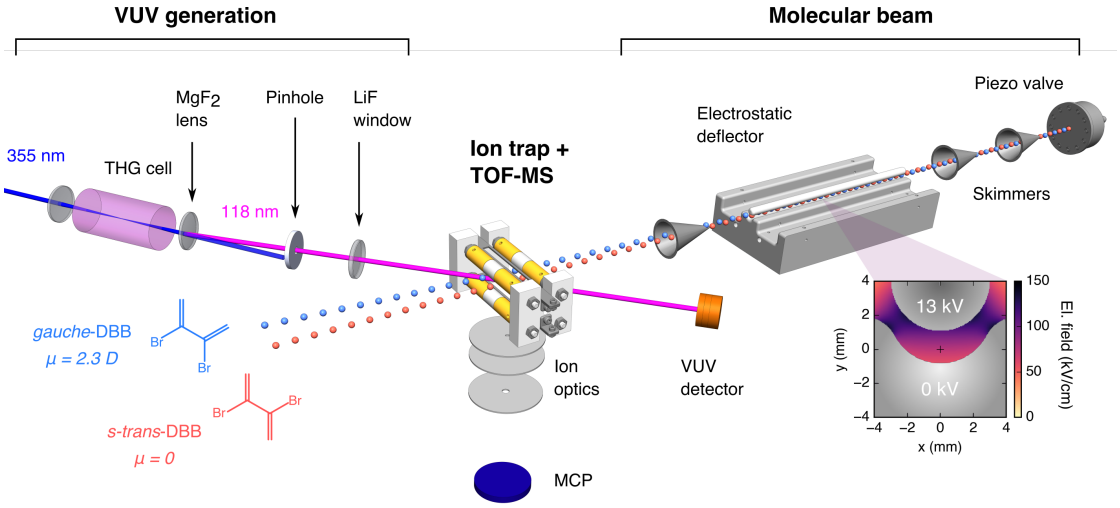

Figure 5.3: **Overview of the experimental setup.**

5.3 Results

5.3.1 Torsional profiles of the 2,3-dihalobutadienes

A graphical representation of the torsional profiles of the 2,3-difluoro-, dichloro-, and dibromobutadienes is shown in Fig. 5.4 (a). The global minimum was found to be the *s-trans* structure (at $\Theta = 180°$) in all cases. Local minima were found to be near *gauche* (rather than *s-cis*) structures at torsional angles varying from $\Theta = 50°$ to 60° depending on the specific molecule.

Subsequently, differences in potential energy and absolute dipole moment between the local and global minima were calculated including harmonic and anharmonic thermal corrections of zero-point vibrational energy and Gibbs free energy. The harmonic and anharmonic frequency calculations were performed using DSD-PBEP86-D3BJ as implemented in Gaussian09. No specific parameters were applied. The DFT results for the torsional potentials and dipole moments were in very good agreement with CCSD(T)-F12/cc-pVTZ-F12 [140, 141, 142, 143] calculations (Table 5.1). We additionally checked if including Douglas-Kroll-Hess (DKH) scalar relativistic effects on the DFT calculations would effect the results. The dipole moments reduced to 1.9369 D for dibromobutadiene, 1.9946 D for dichloro-butadiene, and 2.0113 D for difluoro-butadiene, and no change was observed in the cis-trans energy differences upon including DKH corrections. Since DSD-PBEP86-D3BJ results without DKH scalar relaxation effects are closer to the CCSD(T)VTZ-F12 reference, these corrections were not applied for the results presented here. Furthermore, relaxation at the CCSD/cc-pVTZ-F12 level resulted in geometries identical to those found with DSD-PBEP86-D3BJ/def2-QZVPP with a root-mean-square deviation (RMSD) of 1.9 pm between the final geometries. These results confirm the reliability of our DFT predictions.

While still exhibiting non-negligible conformational energy differences, see Table 5.1, the large dipole moment differences among the 2,3-di[halogen]but-1,3-diene conformers appeared promising, motivating its selection for subsequent experimental investigations. For instance, the dipole-moment difference for 2,3-dibromo-1,3-butadiene was computed at the CCSD(T)/cc-pVTZ-F12 level of theory (neglecting all relativistic effects) to be $\Delta\mu = 2.13$ D.

As the main result of the theoretical screening, 2,3-dibromobuta-1,3-diene (DBB) was identified as an optimal diene for the envisaged experiments that possesses both a

Method	CH_2=C(Br)-C(Br)=CH_2	CH_2=C(Cl)-C(Cl)=CH_2	CH_2=C(F)-C(F)=CH_2
	ΔE (eV)		
CCSD(T)/cc-pVTZ-F12	0.097	0.117	0.151
DSD-PBEP86-D3BJ/def2-QZVPP	0.097	0.114	0.155
DSD-PBEP86-D3BJ/def2-QZVPP + harm. therm. corr.	0.050	0.069	0.142
DSD-PBEP86-D3BJ/def2-QZVPP + anharm. therm. corr.	0.049	0.068	0.139
	$\Delta\mu$ (Debye)		
CCSD(T)/cc-pVTZ-F12	2.1266	3.1001	2.5380
DSD-PBEP86-D3BJ/def2-QZVPP	2.2963	2.3837	2.5938

Table 5.1: **Results of the screening.** Differences in potential energy ΔE and dipole moment $\Delta\mu$ between the local and global torsional minimas of DBB including thermal corrections at T=298.15K (zero-point and Gibbs free energy) for selected 2,3-dihalogen-substituted butadienes.

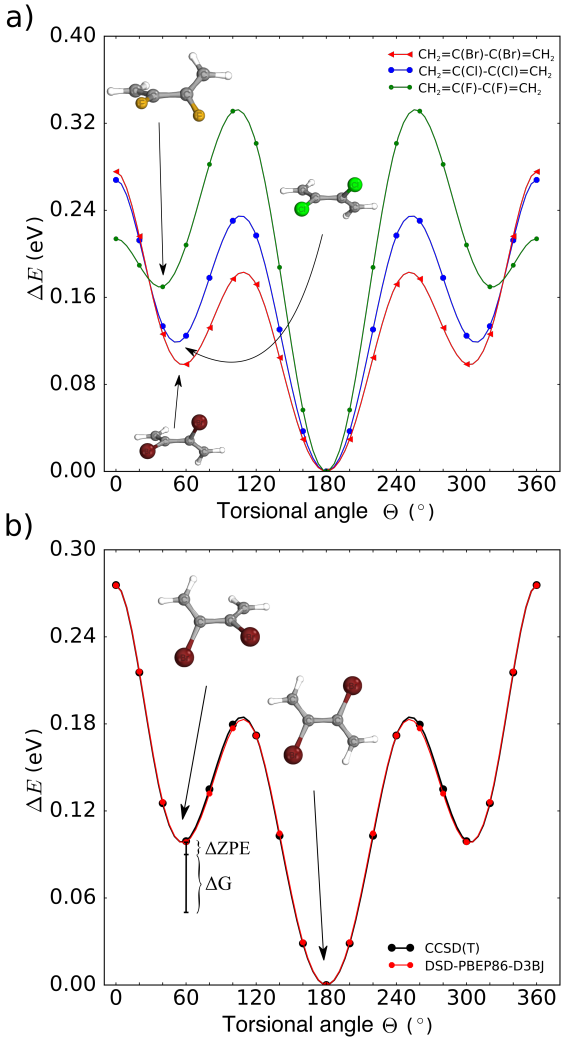

Figure 5.4: **Calculated torsional energy profiles.** a) Cuts through the potential energy surface of 2,3-dibromo-1,3-butadiene (CH_2=C(Br)-C(Br)=CH_2), 2,3-dichloro-1,3-butadiene (CH_2=C(Cl)-C(Cl)=CH_2), and 2,3-difluoro-1,3-butadiene (CH_2=C(F)-C(F)=CH_2) along the torsional coordinate Θ calculated using the DSD-PBEP86-D3BJ functional. Due to the symmetry of the molecules, the torsional profiles are symmetric with respect to mirroring at $\Theta = 180\,°$. The figure shows relative energies ΔE referenced to the energies of the *s-trans* structures at $\Theta = 180°$. b) Potential energy of 2,3-dibromo-1,3-butadiene as a function of the torsional angle Θ calculated at CCSD(T)/VTZ-F12 and DSD-PBEP86-D3BJ/def2-QZVPP levels of theory. The lowering of the energy at the local minima due to the zero point vibrational energy (ΔZPE) and the Gibbs free energy (ΔG) is illustrated for the *gauche* structure. Due to its symmetry, the molecule exhibits two equivalent *gauche* structures.

	Energy $\Delta E = E_{\text{cis}} - E_{\text{trans}}$ (eV)	Dipole moment μ (D)	Rotational constants (GHz) A_e	B_e	C_e
gauche-DBB	0.049	2.29	2.3526	0.8793	0.7097
s-trans-DBB		0.00	4.6077	0.5997	0.5306

Table 5.2: **Summary of molecular parameters of DBB.** Differences in energy, dipole moments and rotational constants of *gauche*- and *s-trans*-2,3-dibromobuta-1,3-diene (DBB) calculated at the DSD-PBEP86-D3BJ/def2-QZVPP level of theory including anharmonic thermal corrections.

sufficiently small energy gap between the *gauche* and *s-trans* ground states as well as a large enough difference in the electric dipole moment of the two species (Fig. 5.4 (b) and Table 5.2) . For *gauche*-DBB a dipole moment of $\mu = 2.29$ D was calculated at the DSD-PBEP86-D3BJ/def2-QZVPP level of theory, while the *s-trans* isomer is apolar on grounds of its inversion symmetry. Table 5.2 summarizes the calculated energy difference as well as the absolute values of the dipole moments and the rotational constants for both conformers.

5.3.2 Simulations of the electrostatic deflection of DBB

Based on the molecular properties obtained from the computations, we predicted trajectories of *gauche*- and *s-trans*-DBB molecules through the electrostatic deflector. In Fig. 5.5, calculated Stark energies (a) and effective dipole moments (b) for rotational states with angular momentum quantum numbers up to $j = 20$ of the *gauche* and *s-trans* conformers of DBB are shown as a function of electric field strength. In the applied electric fields, all rotational states of the *gauche* conformer are strong-field seeking with negative Stark shifts, whereas the *s-trans* conformer does not exhibit a DC Stark effect because of its vanishing dipole moment in the molecular frame. In Fig. 5.5 c), rotational state populations for *gauche*- and *s-trans*-DBB at a rotational temperature of 1.0 K are shown. At this temperature, rotational states up to $j = 14$ are significantly populated and can be expected to contribute to the beam-deflection profiles for both conformers.

The density profiles of the molecular beam along the deflection coordinate at the position of intersection with the probe laser (deflection profiles) are plotted in Fig. 5.5 d) for the *gauche* conformer. The color-coded curves show the contributions from the individual rotational states with angular momentum up to $j = 20$, while the thick black line corresponds to the total thermally averaged deflection profile at a rotational temperature of 1.0 K. For clarity, the contributions of the individual rotational states have been multiplied by a factor of 4 in the figure. The inset contains the same curves with heights normalised to 1 to allow for a better comparison. The grey area in the main plot is a simulation of the undeflected beam profile, at a deflector voltage of 0 kV, which also corresponds to the profile of the unpolar *s-trans* conformer with the deflector voltages turned on. The rotational states of the *gauche* conformer with largest deflection are the low-angular-momentum states (small j). Consequently, significant spatial separation of the *gauche* and *s-trans* conformers can only be achieved experimentally for samples with a sufficiently low rotational temperature [144].

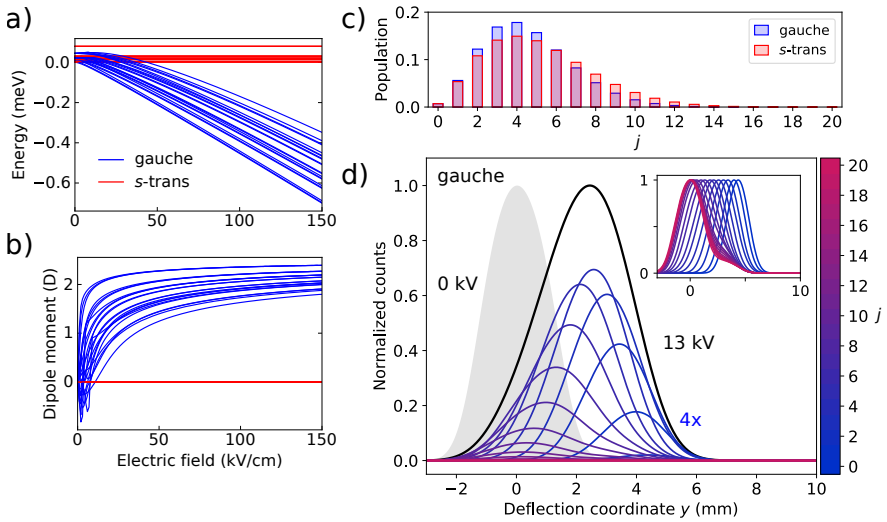

Figure 5.5: **Simulations of Stark shifts and electrostatic deflection for DBB.** Calculated Stark energies (a) and effective dipole moments (b) *vs.* electric field strength for individual rotational states with $j = 0, 1, 2$ of the *gauche* and *s-trans* conformers of DBB. c) Rotational state populations, summed over all levels with the same angular momentum quantum number j, for *gauche* and *s-trans* DBB at a rotational temperature of 1.0 K. d) Simulated deflection profile of the *gauche* conformer (black line) with its different rotational-state contributions in color. The contributions of the different j states are color-coded according the color scale indicated. The undeflected beam profile is shown by the gray area.

5.3.3 Experimental deflection profiles

In order to measure the spatial profiles of the DBB molecules beam emanating from the electrostatic deflector, the molecules were ionized by laser pulses and ejected into the TOF-MS. The choice of the ionization method turned out to be crucial. In Fig. 5.6 a), typical TOF-MS traces obtained using fs-laser-pulse ionization (top) and VUV ionization (bottom) are shown. While fs-laser ionization yielded a large quantity of fragmentation products of the parent DBB molecule, VUV ionization produced a clean mass spectrum with a single peak originating from DBB at 212 u. The inset shows an extended mass range around the DBB peak, illustrating that other species or clusters with larger mass cannot be observed under the present experimental conditions.

Analysis of the different fragment-ion signals obtained from fs-laser ionization, Fig. 5.7 a), revealed that most of the fragments show distinct deflection profiles. Intriguingly, the mass signal corresponding to the parent molecule does not seem to exhibit deflection. This signal could in principle be generated by the break up of larger DBB-containing clusters which may exhibit only very small dipole moments, similar to the situation observed in the deflection of H_2O [21]. However, DBB cluster ions are not observed in the TOF spectra, Fig. 5.6 a), and hence we can essentially rule out that the lack of deflection observed for the DBB^+ mass peak measured by fs ionization is due to breakup of molecular aggregates. The different deflection profiles recorded for ion signals of the individual fragments are caused by the fs-laser-induced breakup of the parent DBB

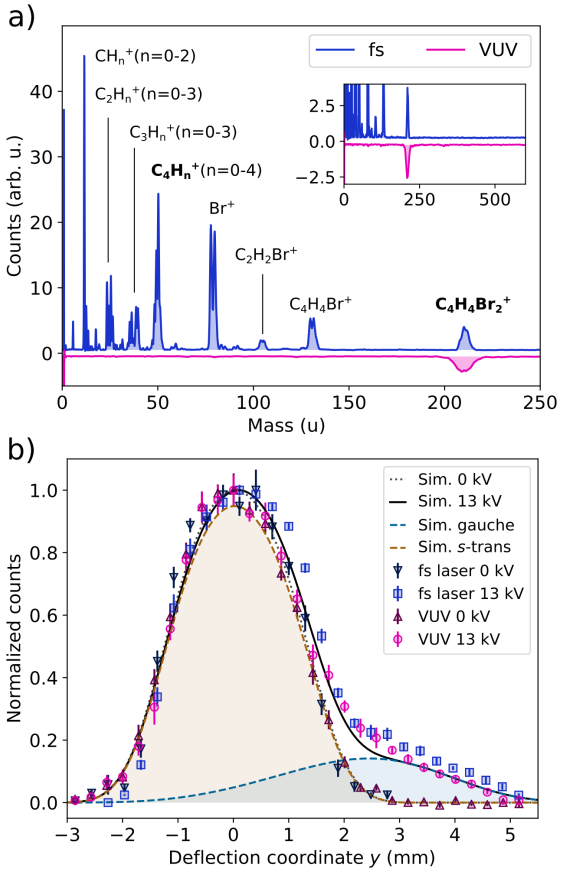

Figure 5.6: **Deflection profiles.** a) Representative TOF-MS trace obtained using fs-laser-pulse ionization (top) and VUV ionization (bottom) of DBB. b) Molecular-beam profiles measured using both ionization methods at deflector voltages of 0 kV and 13 kV together with corresponding simulations. For fs-laser-pulse ionization, the profiles for the fragment $C_4H_n^+$ are shown. Error bars represent standard errors of at least five independent measurements.

molecule. It is possible that the electric field of the relatively long laser pulses drives different multiple-ionization dynamics for the polar *gauche* conformation than for to the apolar *s-trans* conformation, thus leading to distinct conformer-specific fragmentation patterns [145]; these are further discussed on the next page.

The complexity of the observed fragmentation dynamics prevented us from unambiguously determining the deflection profile of the DBB parent molecule using fs-laser ionization. Therefore, we implemented soft VUV ionization, which is capable of ionizing DBB without fragmentation as apparent from Fig. 5.6 a) and the corresponding molecular-beam profiles in Fig. 5.6 b). While the data points measured with VUV (purple triangles and circles, respectively) probe DBB directly, the data shown for fs-laser-pulse ionization corresponds to the accumulated signal for the fragments $C_4H_n^+$ ($n = 0 \ldots 4$) (blue triangles and squares, respectively) produced under these conditions. The experimental data points for VUV ionization agree very well with the simulated thermally-averaged beam profiles at a rotational temperature of 1.0 K, which are shown as grey

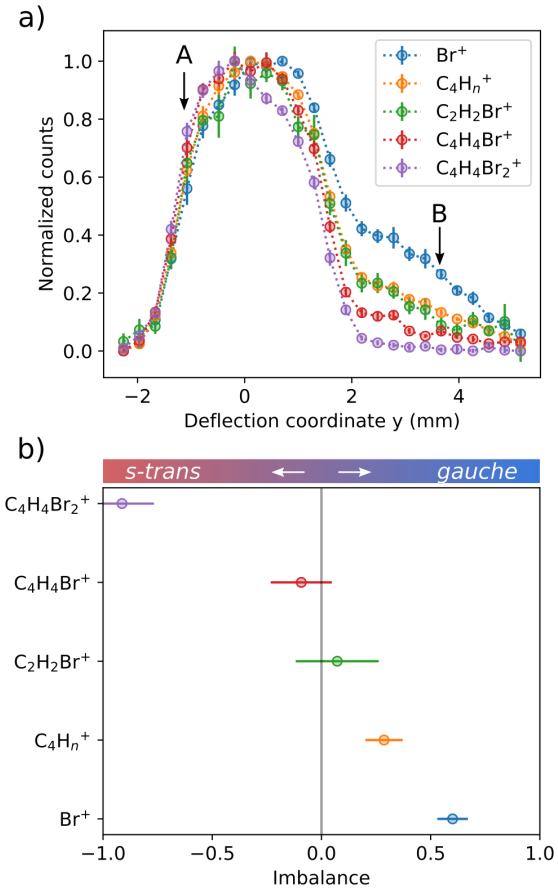

Figure 5.7: **Deflection curves of a molecular beam containing DBB probed at different ionic fragment masses produced by fs-laser-pulse ionization.** a) Ion counts of four molecular fragments and the mass of the parent DBB molecule vs. deflection coordinate. b) Measured imbalance of fs-laser ionization products between the two points A and B in a). See text for details. Error bars represent standard errors of six independent measurements.

dotted line (0 kV) and black solid line (13 kV). Corresponding individual contributions from the *gauche* and *s-trans* conformers are depicted as the blue and orange shaded areas, respectively. The deflection profile at 13 kV shows a tail towards higher deflection coordinates where simulations indicate the presence of pure *gauche*-DBB. The overall very good agreement between the measured and simulated deflection profiles allows us to confirm the successful separation of the DBB conformers and validates the accuracy of the theoretical calculations.

Further evidence for the separation of the *gauche* and *s-trans* conformers can be found in the measured fragmentation products due to fs-laser-pulse ionization of the molecular beam. Fig. 5.7 a) shows normalized profiles of four representative fragment families Br^+, $C_4H_4^+$, $C_2H_nBr^+$, $C_4H_4Br^+$ and the parent molecule DBB^+ as a function of the deflection coordinate. Clearly, the tail of the profile towards large deflection coordinates, where one expects the contribution from *gauche*-DBB, varies strongly among the different

fragments, with Br^+ showing the largest and DBB^+ almost zero amplitude. In the region around $y \approx -1$ mm, this behavior is inverted. At this location, our trajectory simulations predict a predominance of *s-trans*-DBB. In order to quantify the imbalance of the observed fragment yields for the *gauche* and *s-trans* conformers, we selected the data points at the locations labeled A and B in the figure. From our simulations, we estimate that the populations are $p_{s-trans} \approx 1$ at A and $p_{s-trans} \approx 0$ at B. We evaluate the imbalance between *gauche* and *s-trans* for any fragment X as the relative difference $a_X = (n_X^A - n_X^B)/(n_X^A + n_X^B)$ with $n_X^{A,B} = N_X^{A,B}/N_{\mathrm{VUV}}^{A,B}$ being the fragment counts $N_X^{A,B}$ normalized by the total DBB beam density $N_{\mathrm{VUV}}^{A,B}$ at the respective point as measured by VUV ionization. The imbalance a_X takes values in the range $[-1, +1]$, corresponding to a strong correlation with *s-trans* or *gauche* DBB, respectively. Fig. 5.7 b) shows the obtained imbalance values which range from $-0.9(1)$ for DBB^+ to $0.60(7)$ for Br^+. All fragments show a tendency of increasing imbalance towards *gauche* with decreasing fragment size, thus suggesting that *gauche* DBB is more likely to break up into smaller parts during the interaction with the fs laser pulse. A rationalization of this phenomenon requires further study.

5.4 Conclusion

Driven by the motivation to gain a precise understanding of the effects of molecular conformation in cycloaddition reactions, a quantum-chemical screening was performed to identify diene candidates suitable for conformer separation in a molecular-beam apparatus. As an optimal diene, 2,3-dibromobuta-1,3-diene was found to exhibit the desired large difference in electric dipole moments and small energy difference between the two conformers. Since this particular dihalogenated diene cannot be purchased, mainly due to its intrinsic tendency to undergo polymerization, a synthesis was developed to produce the compound in adequate purity. Experimental validation of the calculated properties was achieved by seeding DBB in a molecular beam and separating its *gauche* and *s-trans* conformers in an electrostatic field gradient. A deflection profile of DBB was measured by subsequent ionization and ejection into a time-of-flight mass-spectrometer. The implementation of a vacuum-ultraviolet light source achieved ionization of the parent diene without fragmentation and therefore made it possible to directly measure its deflection behavior. Spatial separation of the two conformers was then confirmed by a close agreement of the observed deflection profiles with Monte-Carlo simulations based on the theoretical molecular properties. Comparison between ion yields from VUV and non-resonant fs-laser-pulse ionization suggest different fragmentation patterns for the *gauche* and *s-trans* conformers during ionization in the strong field. The polar *gauche* conformer showed an enhanced tendency to fragment in comparison with the apolar *s-trans* conformer. The successful separation of the *gauche* and *s-trans* conformers of this tailor-made diene paves the way toward studies of conformer-selected polar cycloaddition reactions in a cold and controlled environment.

6

Reaction of *gauche*- and *s-trans*-DBB with laser cooled Ca^+ ions

Understanding gas-phase ion-molecule reactions is of profound importance to gain knowledge about chemical processes taking place in the atmosphere and in space. Reactions involving different conformational isomers of organic molecules are particularly intriguing because of their high selectivity. Here, we create samples of selected *gauche* and *s-trans* 2,3-dibromobutadiene (DBB) in a molecular beam and study their reaction with Coulomb crystals of laser-cooled Ca^+ ions in an ion trap. The rate constant is found to strongly depend on both the conformation of DBB and the electronic state of Ca^+. In the excited states of Ca^+ ($^2P_{1/2}$ and $^2D_{3/2}$), the rate constants are capture-limited and enhanced for the *gauche* conformer due to its permanent dipole moment. With Ca^+ in the ground state ($^2S_{1/2}$), the rate for *s-trans* DBB is unchanged, while that for *gauche* DBB is strongly suppressed, pointing to the presence of an energy barrier in the short-range reaction pathway. This shows that molecular conformation can efficiently promote reactivity in ground-state ion-molecule reactions.[1]

6.1 Introduction

Gas phase ion-molecule reactions play an important role in the ionosphere of the earth and in interstellar clouds [54, 146, 55]. Recently, various organic compounds have been identified on Saturn's moons: in the atmosphere of Titan [147, 148] and in cryo-volcanic plumes ejected from Enceladus [149]. To understand the life cycle of extraterrestrial organic material, promising laboratory techniques for the exploration of ion-molecule reactions under controlled conditions have emerged [9]. Another important application of reactions between organic molecules and metal ions arises in the context of catalysis, where gas-phase studies can help to elucidate the mechanisms of bond activation [150, 151]. A powerful method for the investigation of ion-molecule reactions is based on trapped and laser-cooled atomic ions forming Coulomb crystals [17, 8, 9]. Coulomb crystals can be considered as reaction vessels in which other reactant and product molecular ions can be co-trapped and cooled sympathetically by the laser-cooled species. Control

[1] J. Wang and L. Xu are acknowledged for assistance with the measurements presented here.

over the neutral reactant can be achieved in molecular beams created by supersonic expansions [6, 7]. In particular, the use of inhomogeneous electrostatic fields has enabled the spatial separation of different molecular conformations and rotational states based on their different electric dipole moments [12, 10, 13, 14, 15, 33]. Combining such a state-selected molecular beam with trapped ions as the reaction target has enabled the measurement of reaction rate constants of individual conformers [13] and rotational states [21].

If an ion-molecule reaction proceeds without an energy barrier along the reaction path, the rate constant is usually determined only by the long-range part of the ion-molecule interaction [152, 52]. In this case, capture theories can be applied to model rate constants [56]. So far, the experiments observing conformational effects in reactions between trapped ions and state-selected molecular beams have explored these scenarios [13, 21]. The observation of conformational effects caused by short-range ion-molecule interactions has remained elusive.

Additionally, a number of studies focused on the direct reaction of atomic ions, e.g. Mg^+ [153, 154] or Ca^+ [68, 155, 13, 63, 64], with molecular beams or thermal samples of neutral atoms or molecules. These studies typically found that fast reactions proceeded from excited states of the ion while reactions involving the ground state were kinetically hindered. Here, we perform kinetic measurements of trapped Ca^+ ions with a molecular beam of 2,3-dibromobutadiene (DBB) molecules and use electrostatic deflection to separate its *gauche* and *s-trans* conformers [33]. Our measurements show that the reaction rate constant of Ca^+ with *s-trans* DBB is capture-limited irrespective of the electronic state of Ca^+, i.e. $^2S_{1/2}$, $^2P_{1/2}$ or $^2D_{3/2}$. For the *gauche* conformer, on the contrary, we find that the reaction is capture-limited only with Ca^+ in its $^2P_{1/2}$ or $^2D_{3/2}$ excited states. In the $^2S_{1/2}$ ground state, however, the reaction rate is strongly suppressed, which could be explained by the presence of a transition state or submerged barrier. This implies the existence of different reaction pathways for the two conformers.

6.2 Results

6.2.1 Experimental setup

The experimental setup (Fig. 6.1a) consisted of a molecular beam apparatus interfaced with an ion trap that has been described before in [13, 21]. An internally cold beam of the neutral reaction partner DBB seeded in neon carrier gas at 5 bar was formed by pulsed supersonic expansion with a pulse duration of 250 μs and a repetition rate of 200 Hz. The beam passed through a series of skimmers and an electrostatic deflector before it reached the ion trap. The deflector's inhomogeneous electric field allowed the separation of the polar *gauche* conformer of DBB (dipole moment $\mu_{\text{gauche}} = 2.29$ D) from the apolar *s-trans* conformer ($\mu_{\text{trans}} = 0$). In the ion trap, laser-cooled Ca^+ ions formed a Coulomb crystal [9] and served as a collision target for the molecular beam. Different conformers of DBB were selectively brought into reaction with the Ca^+ ions by vertically tilting the molecular beam apparatus.

The reaction of Ca^+ with the *gauche* and *s-trans* DBB conformers proceeded via individual pathways with bimolecular reaction rate constants k_g and k_t, respectively (Fig. 6.1b). Throughout the reaction, the fluorescence of Ca^+ ions due to laser cooling

on the $^2S_{1/2} \rightarrow {}^2P_{1/2}$ transition at 397 nm was imaged on a camera (Fig. 6.1b). As the reactions progressed, the Coulomb crystals changed shape due to loss of Ca^+ ions and accumulation of heavier product ions around the Ca^+ core. Quantitative analysis of the reaction kinetics and products was performed by ejecting the trapped ions into a time-of-flight mass-spectrometer (TOF-MS) radially coupled to the ion trap [61]. Two different modes of operation were used for the TOF-MS. For the determination of mass spectra of the reaction products, a low-resolution mode was used to extract ions into the TOF-MS by applying a 1 μs long pulse of 4.0 kV to the repeller electrode. For the rate measurements, additional high-voltage pulses, delayed by 0.45 μs, were applied to the extractor electrodes to selectively enhance the resolution for the Ca^+ and $C_4H_n^+$ species [61].

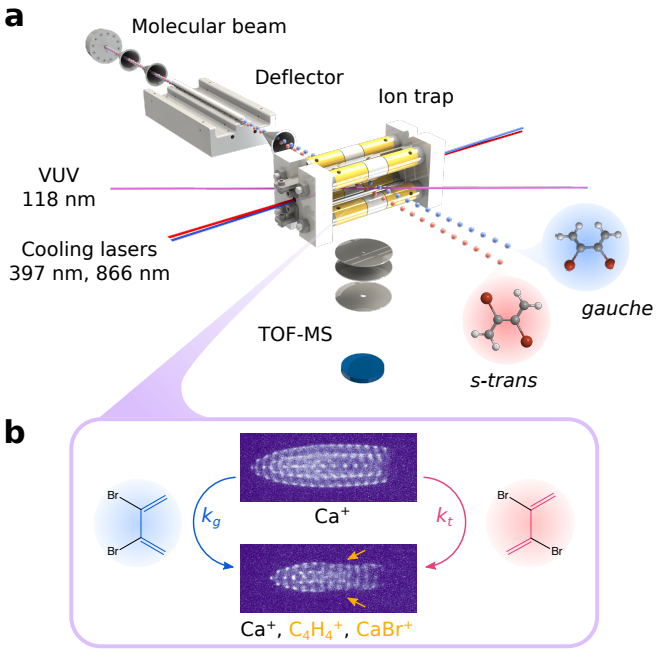

Figure 6.1: **Overview of the experiment. a**, Drawing of the experimental setup. The two conformers of DBB are separated by electrostatic deflection in a molecular beam and directed at an ion trap holding a Coulomb crystal of trapped Ca^+ ions. Reaction kinetics are measured by ion extraction into a TOF-MS. **b**, Depiction of the reaction between the *gauche* and *s-trans* conformers of DBB with Ca^+, each featuring a different reaction rate constant k_g and k_t, respectively. Fluorescence images of the initial laser-cooled Ca^+ Coulomb crystal is shown on the top and after reaction with DBB in the bottom. Arrows indicate regions where ions heavier than Ca^+ accumulate in the trap.

6.2.2 Reaction products

As a first step, the product ions of the reaction were characterised using TOF-MS after a reaction time of 2 minutes (Fig. 6.2). The electrostatic deflector was switched off and a high-flux molecular beam of DBB with thermal (300 K) *gauche:trans* conformer mixture

of 1 : 3.3 (cf. chapter 5) was directed at the ion trap. TOF-MS traces averaged over 45 experiments are displayed in Fig. 6.2a and compared against a control experiment in which the molecular beam did not contain DBB (grey inverted trace). Besides a dominant peak corresponding to Ca^+ (40 u) at a time of flight of $t = 12.9$ μs, the spectra contain four main features that were assigned to specific molecular compounds with assistance of molecular dynamics simulations (cf. section 2.3.5).[2]

In mixed-species Coulomb crystals, the ions arrange in layers such that lightest ions are trapped at the center and successively heavier ions accumulate around the lighter ions in shells of increasing radius. This inhomogeneous ion distribution leads to a broadening and bimodal structure of the peaks in the TOF-MS [61]. In the simulations, a typical Coulomb crystal of 500 Ca^+ ions (mass 40 u) was assumed, additionally containing 20 ions of each of the masses 50 u, 51 u, 52 u, 57 u, 72 u, 120 u and 200 u. A comparison of the experimental data of Fig. 6.2a with the simulation is shown in Fig. 6.3. Different colours

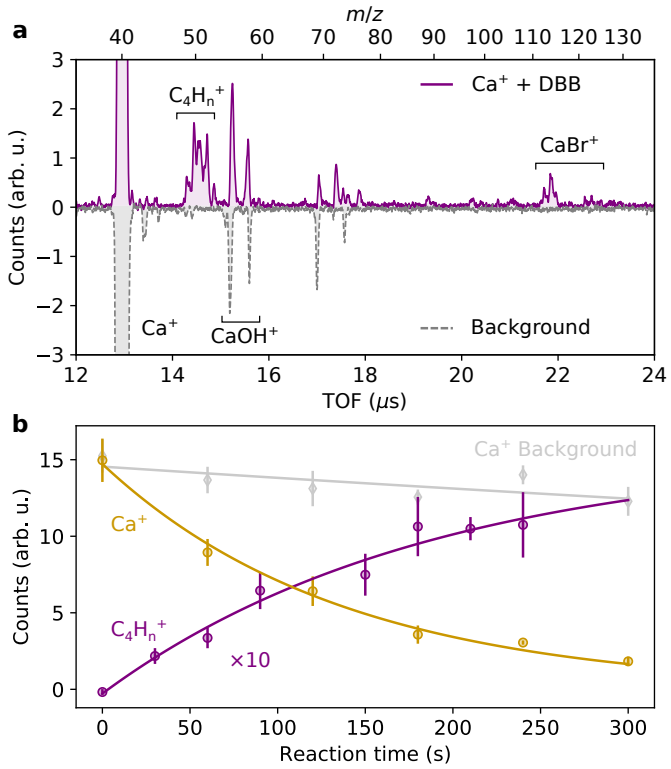

Figure 6.2: **Reaction products.** **a**, Low-resolution TOF-MS of the trapped ions after reaction (purple) and comparison to a Coulomb crystal of Ca^+ exposed to a molecular beam without DBB (gray). Each trace is an average of at least 45 individual measurements. **b**, Reaction-time-dependent ion counts measured using high-resolution TOF-MS: depletion of Ca^+ (yellow) with corresponding background measurement (gray) and formation of $C_4H_n^+$ (purple) were measured on different days. $C_4H_n^+$ signal is rescaled for better visibility. Error bars are standard errors of three independent measurements.

[2]MD simulations were performed by L. Xu.

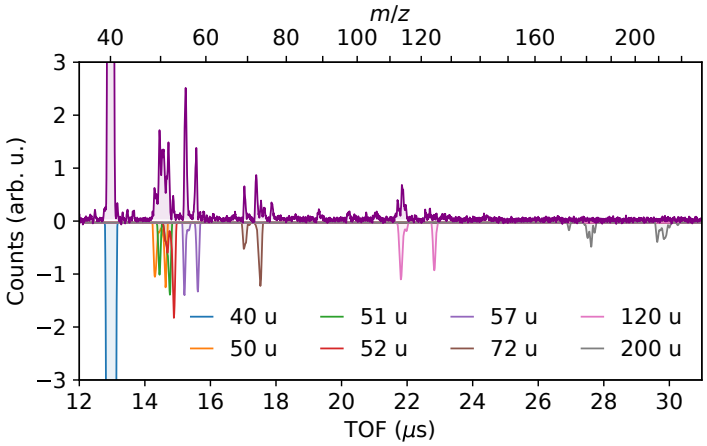

Figure 6.3: **Comparison of experimental and simulated TOF-MS spectrum.** The upper curve shows the measured spectrum while the inverted curve shows a simulated spectrum for 500 ions with mass 40 u and 20 ions of each of the masses 50, 51, 52, 57, 72, 120 and 200 u, highlighted in different colours.

highlight the contribution of each ion mass in the simulation. The time coordinates of the simulation have been shifted globally to match the location of the Ca^+ peaks. The locations and splittings of the individual mass peaks reproduce the measured TOF spectra fairly well. A signal due to $CaBr_2^+$ (200 u) is absent in the data. Slight differences between the simulated and observed splittings of the peaks can be explained by different sizes of the simulated and experimental Coulomb crystals. Based on the good agreement between data and simulation, the product peaks of Fig. 6.3 were assigned to different molecular compounds as summarised in Table 6.1.

In Fig. 6.2a, the main background signal at $t \approx 15$ μs corresponds to $CaOH^+$ (57 u), formed by the reaction of Ca^+ with residual water in the vacuum chamber (pressure 4×10^{-10} mbar). Another weaker impurity signal around $t \approx 17$ μs with approximate mass 72 u could be due to CaO_2^+ [64]. Clearly, ions forming uniquely as products of the reaction $Ca^+ + DBB$ were observed at $t \approx 14.5$ μs and $t \approx 22$ μs and were identified as $C_4H_n{}^+$ (n=2–4, 50 – 52 u) and $CaBr^+$ (119 and 121 u), respectively. Another possible reaction product could be $CaBr_2^+$ (200 u), which was however not detected (see Fig. 6.3). Excess kinetic energy after the reaction or excitation by the UV cooling laser for Ca^+ could lead to its rapid dissociation to $CaBr^+$. A $(H)Br^+$ fragment was also not detected.

Table 6.1: Assignment of molecular compounds to the TOF spectra based on the MD simulation.

Mass (u)	Possible compounds
50,51,52	$C_4H_n^+$, n=2,3,4
57	$CaOH^+$
72	CaO_2^+
120	$CaBr^+$
200	$CaBr_2^+$

Consequently, the reaction leads to a Br-abstraction from DBB and a localisation of the charge on either $CaBr^+$ or the butadiene moiety. The observation of $C_4H_n^+$ fragments points to H-abstraction from the expected $C_4H_4^+$ product [156]. The reaction kinetics for the observed products $C_4H_n^+$ and $CaBr^+$ can thus be modeled using the following equations,

$$Ca^+ + C_4H_4Br_2 \xrightarrow{k^{(1)}} CaBr^+ + C_4H_4Br \tag{6.1}$$

$$\xrightarrow{k^{(2)}} C_4H_n^+ + CaBr_2 + (4-n)H \tag{6.2}$$

with bimolecular rate constants $k^{(1,2)}$. To explore the reaction kinetics, the number of Ca^+ and $C_4H_n^+$ ions were determined as a function of reaction time using the TOF-MS in high-resolution mode [61] in separate experiments (Fig. 6.2b). The event rate of $CaBr^+$ detection was too low to measure its kinetics of formation with significant statistics. Fig. 6.2b compares the decay of Ca^+ in the reaction with DBB (yellow data points) with the formation of the product fragment $C_4H_n^+$ (purple points). The amplitude of the latter is scaled by a factor of 10 for better visibility. For reference, decay of Ca^+ caused by background collisions is also shown (grey points). Due to the constant DBB density n_{DBB} in the molecular beam, the reaction kinetics could be modeled using a pseudo-first-order rate law, i.e.

$$\frac{d}{dt} n_{Ca^+} = -\tilde{k}_{tot} n_{Ca^+}, \tag{6.3}$$

$$\frac{d}{dt} n_{C_4H_n^+} = \tilde{k}^{(2)} n_{Ca^+}. \tag{6.4}$$

Here, $\tilde{k}_{tot} = \tilde{k}^{(1)} + \tilde{k}^{(2)}$, is the total decay rate of Ca^+ and $\tilde{k}^{(1,2)} = k^{(1,2)} n_{DBB}$ are pseudo-first-order rate constants. The solutions are

$$n_{Ca^+}(t) = n_{Ca^+}(0)\, e^{-\tilde{k}_{tot} t}, \tag{6.5}$$

$$n_{C_4H_n^+}(t) = n_{Ca^+}(0)\, \frac{\tilde{k}^{(2)}}{\tilde{k}_{tot}} \left(1 - e^{-\tilde{k}_{tot} t}\right), \tag{6.6}$$

where $n_{Ca^+}(0)$ is the initial Ca^+ density at $t = 0$. The equations (6.5) and (6.6) were independently fitted to the corresponding data traces (lines in Fig. 6.2b) and allowed the extraction of values for $\tilde{k}_{tot}$. From the fit of equation (6.6) to the $C_4H_n^+$ data, a value $\tilde{k}_{tot} = 5.4(3) \times 10^{-3}\ s^{-1}$ was found. Fitting the Ca^+ decay using equation (6.5) yields a value of $\tilde{k}_{tot} = 5.6(4) \times 10^{-3}\ s^{-1}$ after background correction. The good agreement between the two independently determined values for $\tilde{k}_{tot}$ confirms that $C_4H_n^+$ is indeed a product of the bimolecular reaction (6.2). The small yield of $C_4H_n^+$ compared to initial Ca^+ number indicates a small branching ratio $k^{(2)}/k_{tot}$. The kinetic model then implies that $CaBr^+$ should be formed in much larger quantities, which is however not observed in the TOF-MS (Fig. 6.2a). An explanation could be increased loss of heavier product ions from the ion trap. The effective rf-trapping potential is inversely proportional to the ion mass, which leads to their localization further away from the laser-cooled Ca^+ core and renders sympathetic cooling less efficient [45]. Loss from the trap can then be facilitated both by excess micro-motion as well as collisions with the molecular beam.

6.2.3 Conformer-specific rate constants

To investigate the effect of the molecular conformation of DBB on the reaction kinetics, the electrostatic deflector was used to prepare samples of defined conformational compositions. A density profile of the DBB molecular beam along the deflection coordinate (a deflection profile) was measured by vacuum ultraviolet (VUV) ionization of DBB at the position of the ion trap (Fig. 6.4a) [33]. With the deflector turned off (deflector voltage 0 kV), the molecular beam contains a thermal 1:3.3 mixture of the *gauche* and *s-trans* conformers of DBB, respectively. At a deflector voltage of 13 kV, the *gauche*-DBB conformers are deflected away from *s-trans*-DBB in the beam and produce a shoulder at high deflection coordinates in the density profile. A Monte Carlo simulation of the particle trajectories yields good agreement with the data for a rotational temperature of 1 K and independently measured beam velocity $v_{\mathrm{beam}} = 843(58)$ m/s (see section 2.4.4.1). At 13 kV, the peak density of DBB was measured to be $n_{\mathrm{DBB}} = 3.9(5) \times 10^6$ cm^{-3} (see section 2.4.4.2).

The Monte Carlo simulation was used to determine the conformer populations as a function of deflection coordinate (Fig. 6.4b). Three beam positions, marked I–III in Figs. 6.4a and b, corresponding to pure *s-trans* conformer (I), thermal mixture (II) in undeflected beam, and pure *gauche* conformer (III), were chosen for reaction rate measurements. In each position, the Ca^+ ion count was measured as a function of reaction time (Fig. 6.4c). The background loss rate of Ca^+ was determined separately by adjusting the molecular beam such that it did not hit the Coulomb crystal (grey data points in Fig. 6.4c). All traces exhibit an exponential decay of the number of Ca^+ ions which confirms the validity of using a pseudo-first-order rate law for the bimolecular reaction of DBB + Ca^+ with a constant DBB density. Pseudo first-order rate constants $\tilde{k}_{\mathrm{tot},i}$ ($i = \mathrm{I}, \mathrm{II}, \mathrm{III}$) were obtained by fitting exponential-decay models to the data and subtracting the corresponding background rate. From the $\tilde{k}_{\mathrm{tot},i}$, the bimolecular rate constants $k_{\mathrm{tot},i} = \tilde{k}_{\mathrm{tot},i}/n_i$ were calculated using the DBB beam densities n_i at each position i=I, II, III in the deflection profile.

Figure 6.4d shows the measured bimolecular rate constants k_i as a function of the *s-trans* population p_{t} obtained from the Monte-Carlo simulation. The bimolecular rate constant for the depletion of Ca^+ was modeled as the linear combination $k_{\mathrm{tot},i} = p_{\mathrm{g},i}k_{\mathrm{g}} + p_{\mathrm{t},i}k_{\mathrm{t}}$ of the conformer-specific rate constants $k_{\mathrm{g/t}}$ (*gauche/s-trans*). The weighting factors $p_{\mathrm{g/t},i}$ are the respective conformer populations at location i (Fig. 6.4b). A least-squares fit (solid line in Fig. 6.4d) with this model was applied to the data and yielded the bimolecular reaction rate constants $k_{\mathrm{g}} = 0.92(5) \times 10^{-9}$ cm^{3}s^{-1} for the *gauche*-conformer and $k_{\mathrm{t}} = 1.3(6) \times 10^{-9}$ cm^{3}s^{-1} for the *s-trans*-conformer. This implies a relative difference $r_{\mathrm{exp}} = 2(k_{\mathrm{g}} - k_{\mathrm{t}})/(k_{\mathrm{g}} + k_{\mathrm{t}}) = -0.35(7)$ by which the *s-trans*-conformer is observed to react faster than the *gauche*-conformer.

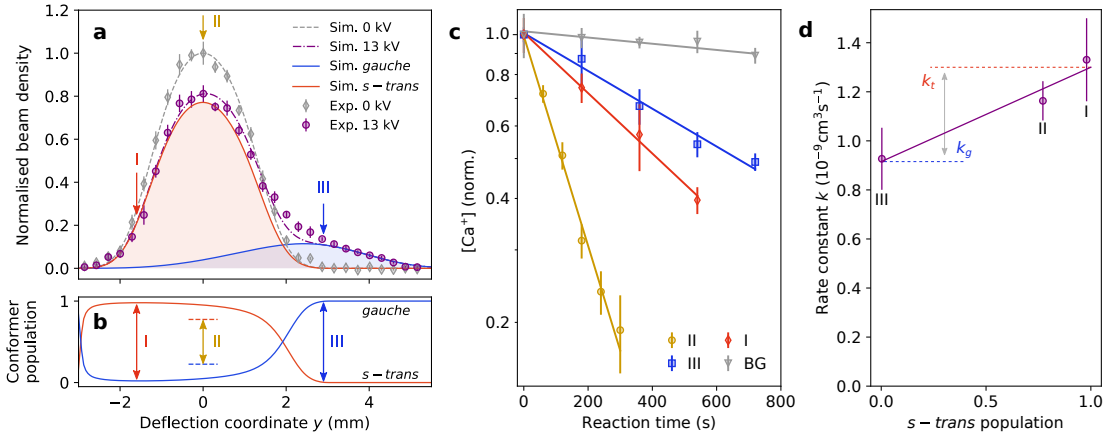

Figure 6.4: **Conformer-specific reaction rate constants.** **a**, Measurement of the DBB molecular beam density profile along the deflection coordinate for deflector voltages 0 kV and 13 kV. The data are in good agreement with Monte Carlo simulations which show the separation of the two conformers. **b**, Simulated conformer populations in the molecular beam obtained from the Monte Carlo simulation. **c**, Reaction kinetics measured in terms of the decay of Ca^+ ion number (normalised to initial value) as a function of reaction time for the three positions I–III marked in **a, b** and a background measurement (BG). The exponential decay of Ca^+ concentration implies pseudo-first-order kinetics. **d**, Bimolecular rate constants extracted from the pseudo-first-order rate constant measurements as a function of the *s-trans*-conformer population with linear fit. Error bars are standard deviations of three independent measurements.

6.2.4 Adiabatic capture rate calculation

To explain the difference in the observed rate constants for the two DBB conformers with Ca^+, rotationally-adiabatic capture theory [56, 58] was employed as detailed in section 1.4.3. The AC calculation proceeded in two steps. First, rotationally-adiabatic and centrifugally-corrected long-range interaction potentials were calculated for each rotational state of *gauche* and *s-trans*-DBB. The ion-molecule interaction includes charge-induced dipole and charge-permanent dipole couplings. The isotropic polarizability volumes $\alpha_g = 13.54$ Å^3 for *gauche*-DBB and $\alpha_t = 13.60$ Å^3 for *s-trans*-DBB were calculated using Gaussian09 [97] in the course of the theoretical screening of chapter 5.

Figs. 6.5a and b show the long-range potentials for collisions of Ca^+ with *gauche*- and *s-trans*-DBB, respectively. Each set of curves corresponds to a different value of the total collisional angular momentum quantum number J. With increasing value of J, a centrifugal energy barrier emerges. The individual curves for each value of J belong to all rotational quantum state $|j_{K_aK_c}, \Omega\rangle$ of DBB with angular momentum quantum number $j = 4$, which is calculated to have the strongest thermal population at $T = 1$ K. Given these long-range potentials, AC theory assigns unit reaction probability to any collision with $J < J_{max}$, for which the centrifugal energy barrier lies below the experimental collision energy $E_{coll} = \mu v_{beam}^2/2 = 124(17)$ meV (black solid line in Figs. 6.5a,b). For each rotational state $|J_{K_aK_c}\Omega\rangle$ of *gauche/s-trans* DBB (g/t), the corresponding value of $J_{max,g/t}(E_{coll}, J_{K_aK_c}, \Omega)$ is determined numerically. Using equation (1.35) AC rate constants were calculated for each rotational state and then averaged according to equation (1.36) assuming a thermal rotational state distribution with rotational temperature of 1 K.

Figs. 6.5a,b show that the centrifugal barrier increases faster with J for *s-trans*-DBB than for *gauche*-DBB such that the maximum collisional angular momenta for a reactive encounter at the experimental collision energy are $J_{max,t} \approx 308$ and $J_{max,g} \approx 427$, respectively, implying a larger cross-section $\sigma \propto J_{max}^2$ for *gauche*-DBB. For the lowest values of J, one notices a steeper slope of the ion-molecule potential for *gauche*-DBB. This points to a stronger attractive interaction between the ion and the permanent dipole of *gauche*-DBB as opposed to the apolar *s-trans* conformer and explains the observed difference in conformer-specific reaction rates. The anisotropic charge-permanent dipole interaction of *gauche* DBB, which is absent for *s-trans* DBB, also leads to a stronger dependence of its rotationally adiabatic potential on the rotational state. This appears as a larger spread between the different potential energy curves for a given value of J.

At the experimental collision energy and rotational temperature, the AC calculation yields bimolecular rate constants of $k_{AC,g} = 2.44 \times 10^{-9}$ cm^{3}s^{-1} for *gauche*-DBB and $k_{AC,t} = 1.26 \times 10^{-9}$ cm^{3}s^{-1} for *s-trans*-DBB, with a calculated relative rate difference between the *gauche* and *s-trans* conformers of $r_{AC} = 0.64$.

The measured rate constant for the *s-trans* conformer agrees with the calculated value. In contrast, adiabatic capture theory predicts a significantly faster reaction rate for *gauche* DBB, for which the data, however, show a reduction of the rate constant compared to *s-trans*. In order to investigate the origin of this discrepancy, additional rate measurements with control over the electronic state populations of Ca^+ were performed. Previous experimental studies with alkaline earth atomic ions [153, 154, 68, 157, 72, 63, 64] showed that the rate of reaction can exhibit a pronounced dependency on the

electronic state of the ion. In these experiments, the ^2S ground state of the ion was often found to be chemically rather inert while the ^2P and ^2D excited states were reactive. This phenomenon was often explained by the presence of energy barriers along the reaction pathway that are overcome by excitation of the ion, leading to strong acceleration of the kinetics.

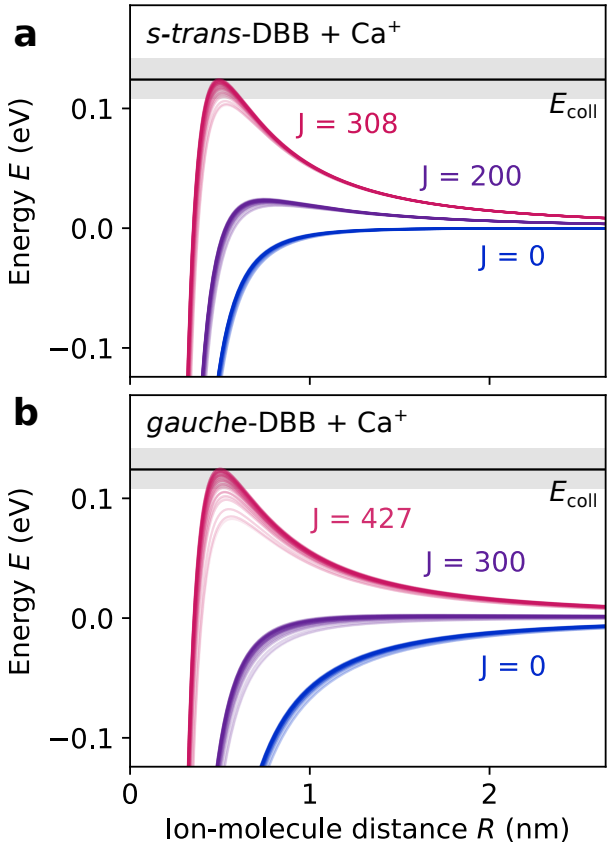

Figure 6.5: **Long-range ion-molecule interaction potentials.** Rotationally-adiabatic and centrifugally-corrected long-range interaction potentials for collisions of *s-trans*- (**a**) and *gauche*-DBB (**b**) with Ca^+. Each value of the total collisional angular momentum J comprises a set of curves corresponding to all rotational states of DBB with rotational angular momentum quantum number $j = 4$, which has the highest thermal population. The collision energy E_{coll} is drawn as the black horizontal line and the grey-shaded areas show its experimental uncertainty.

6.2.5 Determination of Ca^+ electronic state populations

Control over the populations of the electronic states of Ca^+ was achieved by adjusting the detuning of the cooling laser on the $^2S_{1/2} \rightarrow {}^2P_{1/2}$ transition at 397 nm and the repumping laser on the $^2D_{3/2} \rightarrow {}^2P_{1/2}$ transition at 866 nm (see inset of Fig. 6.9a). The fluorescence of Ca^+ generated on the $^2S_{1/2} \rightarrow {}^2P_{1/2}$ transition was measured as a function of the laser detunings and polarization, and modeled using optical Bloch equations (OBE) [68].[3] As detailed below, this allowed a calibration of the average populations in the $^2S_{1/2}$, $^2P_{1/2}$ and $^2D_{3/2}$ electronic states.

In order to calibrate the electronic state populations of Ca^+, the Ca^+ fluorescence on the $^2S_{1/2} \rightarrow {}^2P_{1/2}$ cooling transition at 397 nm was measured as a function of the cooling laser (397 nm) and repumping laser (866 nm) settings. The measured fluorescence signal detected by the camera was integrated in the region of interest and a noise background was subtracted. The resulting signal is proportional to the $^2P_{1/2}$ steady-state population and can be modeled theoretically by solving a set of 8-level OBE for the Ca^+ $^2S_{1/2}$,$^2P_{1/2}$ and $^2D_{3/2}$ states [68, 158]. To determine the parameters for the OBE modelling, i.e. laser detunings, intensities, linewidths and polarization angles, a series of calibration measurements were performed. The two diode lasers were frequency stabilized using a wavemeter, resulting in residual fluctuations on the order of 5 MHz for the 397 nm and 10 MHz for the 866 nm laser. Values for the laser intensities were obtained by measuring the beam waists at $1/e^2$ level, i.e. $w_{397} = 0.4$ mm for the 397 nm beam and $w_{866} = 0.2$ mm for the 866 nm beam, and the optical powers, i.e. $P_{397} = 1$ mW at 397 nm and $P_{866} = 0.5$ mW at 866 nm.

The polarization of the 866 nm repumping laser was adjusted to optimize the repumping efficiency. First, the polarization was cleaned with a polarizing beam-splitter

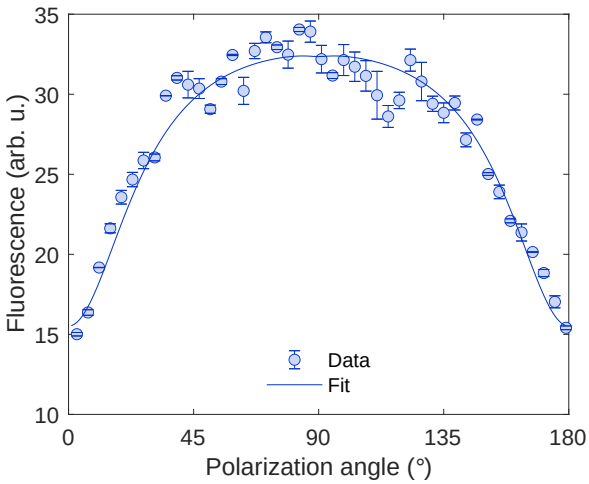

Figure 6.6: **Polarization scan of the repumper.** Ca^+ fluorescence measurement as a function of the 866 nm laser beam polarization angle (data points) and simulated curve from the OBE model. Error bars correspond to one standard deviation.

[3]The MATLAB code for solving the OBE was kindly provided by Z. Meir.

and then rotated using a half-wave plate. Then, the 866 nm beam was combined with the 397 nm light on a dichroic mirror and directed at the ion trap. The polarization of the 397 nm laser was not controlled, since the OBE simulation was found to be insensitive to it. The Ca^+ fluorescence was then measured while varying the polarization angle of the 866 nm repumping laser (Fig. 6.6). The fluorescence data were fitted using the OBE prediction for the P-state population. At a 90° polarization angle relative to the magnetic field axis (locations of minima from fit) the peak fluorescence was found. To maximize population in the $^2P_{1/2}$ state, this setting was used for all subsequent measurements.

After adjusting the polarization, the frequency of the 397 nm cooling laser was set to a detuning of $\Delta_{397} = -10$ MHz, below the "melting point" of the Coulomb crystal at the detuning $\Delta_{397} \approx 0$. Then, the Ca^+ fluorescence was measured as a function of the 866 nm repumper detuning Δ_{866} (Fig. 6.7a). Afterwards, the repumper detuning was set to $\Delta_{866} = 20$ MHz, where repumping is most efficient (Fig. 6.7a) and the detuning Δ_{397} of the cooling laser was scanned (Fig. 6.7b). These two datasets were simultaneously fitted using the OBE model, allowing the determination of the following parameters: the effective laser intensities and linewidths, a detuning offset of the 866 nm laser, and a proportionality constant allowing to convert the measured fluorescence to the P-state population. The fitted laser linewidths were consistent with the observed fluctuations on the wavemeter. To optimise the fit, a magnetic field value of 1 Gauss was chosen, which is a reasonable value for the stray magnetic field in the present apparatus. The resulting $^2S_{1/2}$, $^2P_{1/2}$ and $^2D_{3/2}$ state populations determined from this measurement are shown in Fig. 6.8. On resonance of the 866 nm repumper, the $^2D_{3/2}$ state population is minimal and the $^2S_{1/2}$, $^2P_{1/2}$ population reach a maximum. The state populations as a function of Δ_{397} resulting from this calibration are shown in Fig. 6.9a.

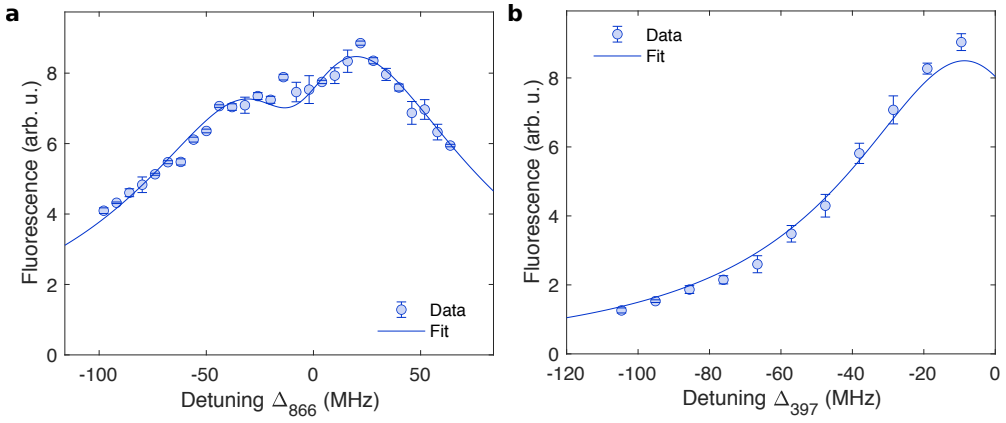

Figure 6.7: **Fluorescence dependence on laser detunings.** Ca^+ fluorescence measurement (data points) as a function of the 866 nm repumping laser detuning (**a**) and the 397 nm cooling laser detuning (**b**). The solid lines are fits to the data based on the OBE model. Error bars correspond to one standard deviation.

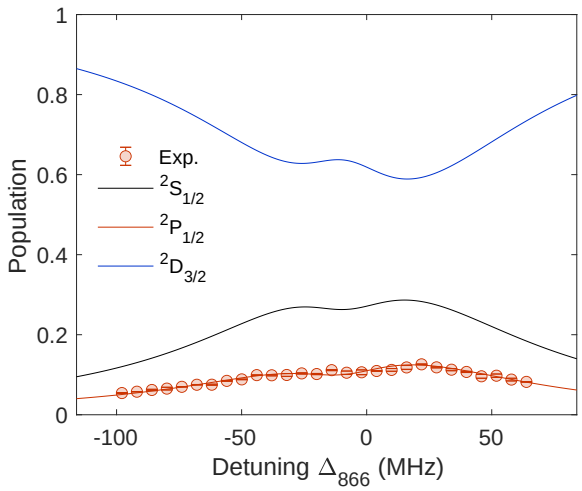

Figure 6.8: **Ca^+ state population dependence on the repumper detuning.** The state populations calculated using the OBE with fit parameters from Fig. 6.7a are shown as function of the 866 nm repumping laser detuning.

6.2.6 Calcium-state-specific rate constants

With control over the Ca^+ electronic state populations, their influence on the reaction rate constant of Ca^+ with DBB could be determined. Fig. 6.9a shows the dependence of the level populations of Ca^+ on the detuning of the cooling laser, with data points being the experimental $^2P_{1/2}$ state populations determined from fluorescence measurements and the solid lines representing the theoretical model. The excited-state $^2P_{1/2}$ and $^2D_{3/2}$ populations increase with decreasing detuning, while the ground-state $^2S_{1/2}$ population decreases.

To measure the reaction rate constants as a function of the excited-state population of Ca^+ , a set of detunings labelled i–iii in Fig. 6.9a was chosen that samples the combined $^2P_{1/2} + {}^2D_{3/2}$ population between 0.25 and 0.7. At each detuning, one rate measurement was conducted with pure *s-trans* DBB (molecular beam position I in Fig. 6.4a) and three measurements for pure *gauche* DBB (molecular beam position III). Results of the state- and conformer-resolved rate measurements are presented in Fig. 6.9b. The measured rate constants $k_{g/t,x}$ as a function of the $^2P_{1/2}+{}^2D_{3/2}$ excited state probability p_x ($x = \mathrm{i}, \mathrm{ii}, \mathrm{iii}$) were fitted by the linear model $k_{g/t,x} = (1-p_x)k_{g/t;S} + p_x k_{g/t;P+D}$, to retrieve the ground-state rate constants $k_{g/t;S}$ and the excited-state rate constants $k_{g/t;P+D}$. Due to the strong correlation between the populations and rate constants in the $^2P_{1/2}$ and $^2D_{3/2}$ states obtained in the fit, no statements about their individual reaction rates could be made and only the effective rate constant averaged over both excited states is given.

Strikingly, the observed dependence of the rate constant on the Ca^+ excited state population differs strongly between the two conformers of DBB. While the rate constant remains nearly constant for *s-trans*-DBB, a clear increase with $P + D$ population is observed for the *gauche* conformer. The fitted bimolecular rate constants of *s-trans* DBB with Ca^+ in ground and excited states, $k_{t;S} = 1.4(3) \times 10^{-9}$ cm^{3}s^{-1} and $k_{t;P+D} = 1.5(3) \times 10^{-9}$ cm^{3}s^{-1}, respectively, lie within one standard deviation from each other and agree with the capture model prediction. For the *gauche* conformer, however, the fitted bimolecular rates are $k_{g;S} = 0.3(2) \times 10^{-9}$ cm^{3}s^{-1} for the Ca^+ ground state and $k_{g;P+D} = 2.2(2) \times 10^{-9}$ cm^{3}s^{-1} for the excited states. In this case, the reaction rate is capture-limited only in the excited state of Ca^+, while it is smaller by about an order of magnitude in the ground state.

These findings can be summarised as follows. With excited Ca^+, the rates are capture-limited and thus only depend on the long-range interaction between the charge of the ion and the dipole moment of the neutral. In this regime, the enhanced rate constant for *gauche*-DBB results from the increase of the collisional cross section by the interaction of its permanent dipole moment with the ion [58, 13, 21]. With Ca^+ in its ground state, the effect of molecular conformation on the rate constant reverses and must be traced to the details of the short-range potential energy surface (PES). The capture-limited rate of the *s-trans* conformer signals the absence of a barrier in its PES along the reaction pathway. By contrast, the rate suppression for *gauche*-DBB implies the existence of a dynamic bottleneck that slows down the reaction.

The *gauche* DBB lies 0.049 eV higher in energy than the *s-trans* conformer and a torsional energy of 0.18 eV is required to interconvert them by internal rotation about the central C-C bond [33]. This means that the reaction of *gauche* DBB with Ca^+ is more strongly activated than the reaction of *s-trans* DBB. Consequently, the observed rate

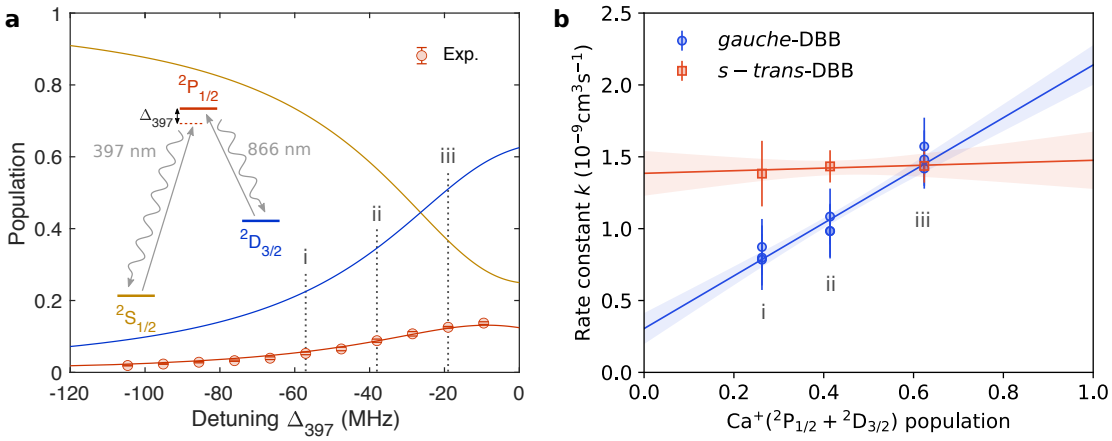

Figure 6.9: **Ca^+ state-dependent rate constants.** **a**, Dependence of the $^2S_{1/2}$, $^2P_{1/2}$ and $^2D_{3/2}$ state populations of Ca^+ on the detuning of the 397 nm cooling laser. Solid lines correspond to the theoretical model and data points represent experimental $^2P_{1/2}$ state population measured by ion fluorescence at 397 nm. The vertical lines labelled i–iii, denote the detunings at which rate measurements were performed. Inset: relevant level diagram of Ca^+. **b**, Results of the state- and conformer-resolved rate measurements at the detunings i–iii of **a**. The lines are linear least-squares fits interpolating between bimolecular rate constants for Ca^+ in the ground (S) and excited states (P+D). Shaded areas correspond to a 90% confidence region. Error bars are fit errors of the individual rate measurements.

constants with ground-state Ca^+ must be explained by distinct reaction pathways that involve an energy barrier only for the *gauche* conformer. To confirm this hypothesis and determine the conformer-specific reaction mechanisms, quantum-chemical calculations of the PES along the reaction coordinate are required. Efforts to perform these calculations are currently being pursued.

6.3 Conclusion

Reaction experiments were performed with conformer-selected DBB from a molecular beam towards trapped and laser-cooled Ca^+ ions. TOF mass spectra identified $C_4H_n^+$ and $CaBr^+$ as the products. An analysis of the reaction rate constant dependence on both the molecular conformation of DBB as well as the electronic state population of Ca^+ revealed two kinetic regimes. With Ca^+ in either of the $^2P_{1/2}$, $^2D_{3/2}$ excited states, the kinetics are capture-limited for both DBB conformers and the rate constant of *gauche*-DBB is enhanced by 0.6 due to its permanent electric dipole moment. If Ca^+ is in its $^2S_{1/2}$ ground state, the rate constant with *s-trans* DBB remains capture-limited, but reaction with *gauche* DBB is strongly suppressed to one tenth of the capture limit. This is remarkable since ion-molecule reactions with alkaline earth ions are commonly observed to only proceed from the excited state. This behaviour can be explained by the existence of a transition-state-induced energy barrier within the ground-state PES of Ca^+ with *gauche* DBB. Such a barrier is absent in the reaction with *s-trans* DBB. In contrast

to previous studies with conformer-selected molecules [13], these results demonstrate a conformational effect at the level of the short-range ion-molecule potential energy surface. Even though the reaction involves a radical cation and is highly activated, the molecular conformation of the neutral can still affect the reaction outcome. In order to thoroughly understand the origin of this effect, high-level quantum chemical calculations are required and might give insight into the underlying reaction mechanism.

7

Loading propene into the ion trap

In this chapter, two methods are described for loading propene ions into a Ca^+ Coulomb crystal. First, the VUV source described in chapter 4 was used for single-photon ionization of propene. In addition, a new method is presented which exploits a charge transfer reaction between doubly ionized Ca^{2+} ions and neutral propene, producing both Ca^+ and propene ions ($C_3H_6^+$). Both methods are compared in view of their efficiency and repeatability for preparing constant amounts of trapped propene ions. This preparation step is required for reaction experiments of propene ions with a conformer-selected molecular beam of *gauche* and *s-trans* DBB (see chapter 8).

7.1 Introduction

The ionization of molecules is a fundamental preparation step for reactive studies with trapped molecular ions [17]. Choosing a robust and efficient ionization method is of great importance to ensure the reproducibility of the subsequent reaction experiments. So far, fs laser pulse ionization was used to ionize smaller molecules such as water or nitrogen with a good ion yield (see chapter 3). However, its extremely high optical intensity results in strong fragmentation for larger organic molecules. This renders fs laser pulse ionization unsuitable for the preparation of pure samples of the parent molecular ion as is required for ion-molecule reaction studies. In chapter 4, ionization by absorption of single VUV photons was introduced as a viable non-destructive ionization method. In particular, for propene and DBB it was found to yield the parent ion without fragmentation. For example, a clean TOF-MS signal of leaked propene gas ionized by VUV is shown in Fig. 4.7.

In this chapter, charge exchange collisions [155, 159, 160, 65] are explored as an alternative to photoionization. This makes use of double ionization of Ca to Ca^{2+} in the focus of the fs laser beam. While the ionization energy of Ca amounts to only 6.1 eV, it is 11.9 eV for Ca^+ [161]. Propene has an ionization energy of 9.7 eV [107] which can be provided by Ca^{2+} as electron "acceptor". Consequently, the charge transfer reaction

$$Ca^{2+} + C_3H_6 \rightarrow Ca^+ + C_3H_6^+ \tag{7.1}$$

is exothermic by 2.2 eV and thus energetically allowed. It produces both propene ions and singly charged Ca^+ ions, the latter of which contribute to further laser cooling of

the Coulomb crystal. Due to the large ionization potential of Ca^+, this method could be applied to most other organic species, in particular those whose ionization potential is too large for them to be ionized by VUV radiation at 118 nm (photon energy 10.5 eV).

7.2 VUV ionization of propene

The experimental sequence started with the standard procedure for loading a Ca^+ Coulomb crystal of a fixed size into the ion trap. A fluorescence image of a typical crystal is shown in the bottom inset of Fig. 7.1. The corresponding high-resolution TOF-MS trace (blue, inverted trace in Fig. 7.1) consists only of the Ca^+ peak.

Next, propene gas was leaked into the reaction chamber using a leak valve (VACGEN LVM series) at a pressure of 3.0×10^{-9} mbar. At the same time, the VUV beam was switched on for 35 s to ionize propene at the location of the ion trap. After ionization, the propene ions were trapped and sympathetically cooled by the Ca^+ Coulomb crystal. For efficient transfer into the trap, the molecules need to have a kinetic energy which is lower than the well depth of the trapping potential. In the present setup, the trap depth was about 2.4 eV for ions with a mass of 40 u [61], which is much larger than the thermal kinetic energy $3k_BT/2 \approx 0.04$ eV at $T = 293$ K of the leaked gas.

Loading of $C_3H_6^+$ into the Coulomb crystal was monitored in real time by imaging the Ca^+ fluorescence on a camera. An image after loading propene onto the crystal is shown in the top inset of Fig. 7.1. Clearly, the presence of heavier ions is observed as a displacement of the Ca^+ ions to the left as well as their spatial rearrangement to a shape resembling an arrow head. The corresponding TOF-MS trace of this crystal is shown as the positive, orange trace in Fig. 7.1. A second strong peak has appeared at 5.23 μs which belongs to the loaded $C_3H_6^+$.

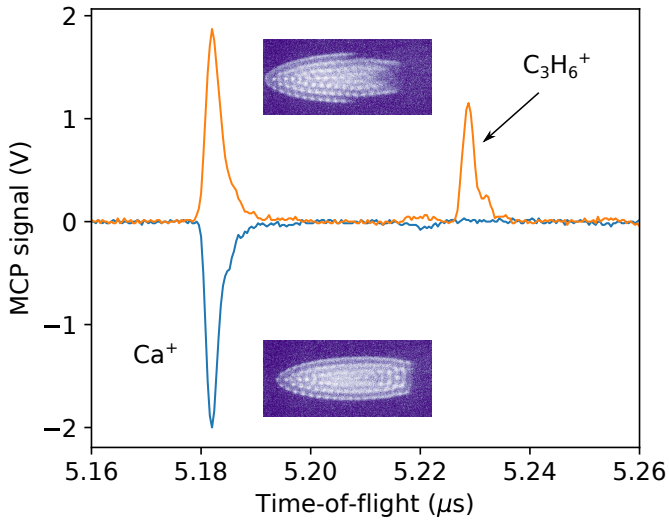

Figure 7.1: **Loading propene using VUV ionization.** TOF-MS traces of the Coulomb crystal before loading $C_3H_6^+$ (blue, inverted trace) and after loading $C_3H_6^+$ using VUV ionization (orange, positive trace). The insets show the corresponding Ca^+ fluorescence images.

Since the propene ions need to be sympathetically cooled by the Ca^+ ions, it was important to understand whether the size of the initial Ca^+ Coulomb crystal had a limiting effect on the propene loading efficiency. To investigate this, Coulomb crystals of four different sizes were prepared and the amount of loaded propene was measured for each of them. Fig. 7.2a displays representative images of the four different Coulomb crystal sizes labelled i–iv. The top row shows the initial, cleaned Ca^+ crystals and the bottom row the corresponding crystals after loading propene for 30 s. These images demonstrate very clearly that the heavier propene ions collect to the right of the Ca^+ ions and push them the left. Preferred displacement of the Ca^+ ions to the left is a consequence of the radiation pressure exerted by the cooling laser beam coming from the right. Depending on the crystal size, specific Coulomb crystal shapes resembling arrow heads appear.

An analysis of the integrated Ca^+ fluorescence counts before and after loading propene is given in Fig. 7.2b. For each crystal size, the final fluorescence counts after loading are plotted against the initial value before loading. The line corresponds to a 1:1 relationship, showing that no significant loss of Ca^+ ions occurred during the loading procedure. For

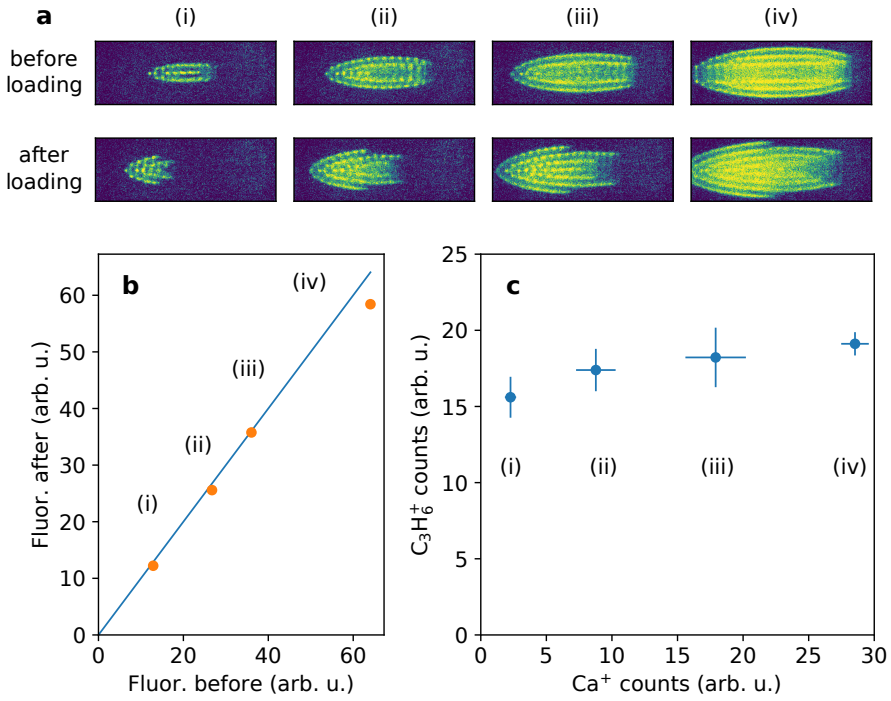

Figure 7.2: **Effect of Coulomb crystal size on the loading efficiency.** **a**, Fluorescence images of Coulomb crystals before (top row) and after loading propene (bottom row) using VUV ionization. Due to the extended loading time needed for crystal (iv), a small amount of light ions ionized from the background forms at the core of the Coulomb crystal. **b**, Ca^+ fluorescence counts before and after loading of propene ions are plotted against each other, showing no significant loss of Ca^+. **c**, TOF mass spectra of the $C_3H_6^+$ counts as a function of Ca^+ counts. Only a weak reduction in propene loading efficiency is observed for small Ca^+ Coulomb crystals.

size (iv), the reduction in fluorescence after $C_3H_6^+$ loading is likely caused by the slight shift of the Ca^+ crystal out of the imaged area.

To determine the ion counts from the TOF-MS, the peaks corresponding to Ca^+ and $C_3H_6^+$ were integrated. Fig. 7.2c displays the $C_3H_6^+$ counts as a function of the Ca^+ counts. Although the amount of Ca^+ was varied by about a factor of 10, this resulted in less than 25% change of the amount of loaded $C_3H_6^+$. Larger Ca^+ crystals show a tendency of increased loading capacity, but even for the smallest Ca^+ crystal, the amount of loaded $C_3H_6^+$ exceeds that of Ca^+ by a factor of 8. Consequently, this demonstrates that the propene loading efficiency depends only weakly on the size of the Ca^+ Coulomb crystal. For even smaller Ca^+ Coulomb crystals than size (i), reduced sympathetic cooling efficiency is expected to strongly limit the amount of trapped molecular ions.

7.3 Charge transfer between Ca^{2+} and propene

As an alternative method for loading $C_3H_6^+$, the charge transfer reaction between doubly charged Ca^{2+} ions in the Coulomb crystal and neutral propene was investigated. Like before, the experimental sequence started with loading a Coulomb crystal of Ca^+ ions into the ion trap. In order to generate Ca^{2+}, the fs laser was focused directly at the Coulomb crystal to enhance the probability of double ionization while a small amount of Ca^+ ions remained to allow sympathetic cooling. In the previous experiments, the focus of the fs laser was located next to the crystal, such that once ionized, Ca^+ ions were trapped and cooled away from the fs laser focus to prevent double ionization. A fluorescence image of the mixed Ca^+/Ca^{2+} Coulomb crystal is shown in Fig. 7.3a ($t = 0$ s). Here, the Ca^{2+} ions accumulate at the center of the trap due to their smaller mass/charge ratio and form a non-fluorescing band. The width of this band was taken as an indicator for the amount of loaded Ca^{2+} to ensure repeatability.

Once loading of Ca^{2+} was completed, the fs laser was switched off and the charge-transfer reaction was initiated by leaking propene into the reaction chamber at a partial pressure of $p = 3 \times 10^{-9}$ mbar. This corresponds to a mean density of $n_{\mathrm{prop}} = p/(k_B T) \approx 7 \times 10^7$ cm^{-3} at ambient temperature $T = 293$ K. In the fluorescence image of the Coulomb crystal after 30 s of propene leaking (Fig. 7.3a, $t = 30$ s), about half of the Ca^{2+} ions have reacted away and converted into Ca^+, which is seen as a narrowing of the non-fluorescing band. After 80 s only small amounts of Ca^{2+} remain (Fig. 7.3a, $t = 80$ s). Sympathetically cooled propene ions accumulate around the slightly lighter Ca^+ ions and change the shape of the imaged fluorescence.

Quantitatively, the formation of $C_3H_6^+$ ions was verified in high-resolution TOF mass spectra (Fig. 7.3b). The spectrum of the initial crystal at $t = 0$ (inverted, blue trace) consists only of the Ca^+ and Ca^{2+} peaks at 5.2 μs and 4.8 μs, respectively. After $t = 80$ s of propene leaking (top, purple trace), the Ca^{2+} signal has almost completely vanished and the Ca^+ peak has increased. Moreover, an additional peak at 5.3 μs time-of-flight has appeared due to $C_3H_6^+$. A minor second peak to the left of the Ca^+ peak could not be identified, but was found not to interfere with the subsequent measurements.

Having established the formation of $C_3H_6^+$ by charge transfer, the reaction kinetics were probed by measuring the ion numbers as a function of reaction time between $t = 0$ and $t = 80$ s using TOF-MS in high-resolution mode. The post-ejection acceleration delay

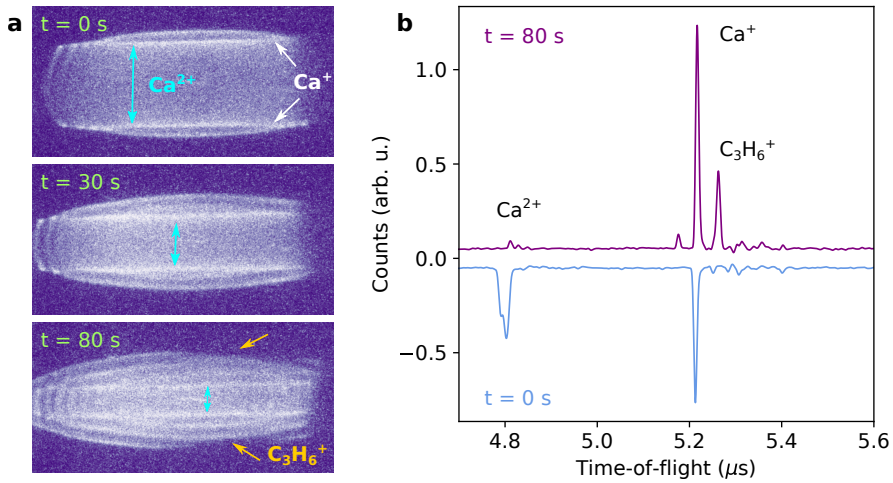

Figure 7.3: **Charge transfer between Ca^{2+} and propene.** **a**, Fluorescence images of the initial Ca^+ Coulomb crystal at three different reaction times. At $t = 0$ (top) Ca^{2+} is visible as the non-fluorescing band at the center (highlighted with blue double arrow). At reaction times $t = 30$ s (middle) and $t = 80$ s (bottom) the amount of Ca^{2+} decreases and propene ions form a shell around the lighter Ca^+ ions (indicated by orange arrows). **b**, TOF mass spectra before (bottom, $t = 0$) and after (top, $t = 80$ s) charge transfer reaction of Ca^{2+} with neutral propene.

was chosen such that the mass resolution was optimal for the Ca^+ and $C_3H_6^+$ product ions (Fig. 7.3b). This came at the expense of a low resolution at the time-of-flight of the reactant ion Ca^{2+}. With this choice of delay, other light impurity ions such as H_2O (18 u), N_2 (28 u) and O_2 (32 u) would produce peaks overlapping with that of Ca^{2+} and thus could not be distinguished from it.

Fig. 7.4a displays the measured ion numbers of Ca^{2+}, Ca^+ and $C_3H_6^+$ as a function of reaction time. An exponential decay is observed for Ca^{2+}, whereas the ion numbers of the two products increase linearly. For comparison, background measurements of the ion numbers without leaking propene are displayed in Fig. 7.4b. These data show no significant loss of Ca^{2+} due to reaction with background gas or spontaneous production of $C_3H_6^+$.

With the density n_{prop} of the leaked propene in excess, the bimolecular reaction (7.1) could be modeled by pseudo-first order kinetics. To determine the pseudo-first-order rate constant $\tilde{k}_0 = k_0 n_{\text{prop}}$, the Ca^{2+} data were fitted with an exponential decay $n_{Ca^{2+}}(t) = n_{Ca^{2+}}(0)e^{-\tilde{k}_0 t}$. The data of the product ions on the other hand were fitted with a linear function $n_i(t) = n_i(0) + a_i t$ ($i = Ca^+, C_3H_6^+$). To obtain approximate rate constants from the slopes a_i of the linear fits, the slopes were divided by the fitted initial Ca^{2+} count, i.e. $\tilde{k}_i = a_i / n_{Ca^{2+}}(0)$. This is motivated by the first order Taylor approximation of the expected exponential saturation of product formation due to depletion of the reactant Ca^{2+}, i.e.

$$n_i(t) = n_i(0) + n_{Ca^{2+}}(0)\frac{\tilde{k}_i}{\tilde{k}_0}\left(1 - e^{-\tilde{k}_0 t}\right) \approx n_i(0) + n_{Ca^{2+}}(0)\tilde{k}_i t. \tag{7.2}$$

Here, $\tilde{k}_i/\tilde{k}_0$ is the branching ratio for formation of product i. The fits are plotted as the solid lines in Fig. 7.4a and agree well with the data. From the exponential decay of Ca^{2+}, a bimolecular rate constant $k_0 = \tilde{k}_0/n_{\text{prop}} = 4.4(1) \times 10^{-10}$ cm^{3}s^{-1} was calculated. The linear fits to the product ion numbers yield bimolecular rates of $k_{Ca^+} = 0.64(6) \times 10^{-10}$ cm^{3}s^{-1} for Ca^+ and $k_{C_3H_6^+} = 0.68(3) \times 10^{-10}$ cm^{3}s^{-1} for $C_3H_6^+$. The fact that the linear growth rates of Ca^+ and $C_3H_6^+$ are equal within the measurement uncertainty is strong evidence for their simultaneous production in the proposed charge transfer reaction (7.1). However, the decay rate k_0 of Ca^{2+} is larger by a factor of about 6.5, which implies a low yield of the charge-transfer products. For comparison, the bimolecular rate constant was calculated based on the high-temperature infinite-order-sudden-approximation capture model (equation (1.31) and [52]), including charge-permanent-dipole and charge-induced-dipole couplings between propene and Ca^{2+}. This gives a much larger rate constant of $k_{\text{capture}} = 3 \times 10^{-9}$ cm^{3}s^{-1}. Despite the limits of the capture model, the discrepancy between the measured and theoretical rates might point to a dynamical bottleneck that slows down the reaction [155, 160, 65].

To further explore the mismatch between the Ca^{2+} decay rate and the product formation rates, the total Ca ion counts (Ca^++Ca^{2+}) with and without propene leaked into the chamber were compared. For a 100% efficient charge transfer reaction, the number of trapped Ca ions should be conserved. Fig. 7.4c shows the total Ca ion counts as a function of reaction time. When no propene is leaked into the chamber, the counts remain stable over time. With addition of propene, however, the counts drop significantly during the first 30 s and stabilize afterwards. This observation appears to be connected to the Ca^{2+} data (Fig. 7.4a). During the first 30 s, the decay is rather non-exponential. After 30 s, when the Ca^{2+} number has dropped to about one third, the data agree well with the fitted exponential decay. This suggests that a more complicated loss mechanism of Ca^{2+} occurs during the first 30 s. This could be caused by inelastic collisions with propene due to the large amount of loaded Ca^{2+}. Given the limited resolution of the TOF-MS at the time-of-flight of Ca^{2+} in these measurements, it is also possible that the Ca^{2+} signal contains a contribution of an unresolved impurity mass. Hence, an additional reaction channel, not leading to the charge transfer products, might explain the observed difference between the decay rate of Ca^{2+} and the growth rate of the products. Since the goal of this experiment was merely to identify whether charge transfer is a reliable method for loading $C_3H_6^+$, additional studies of the Ca^{2+} kinetics were not undertaken.

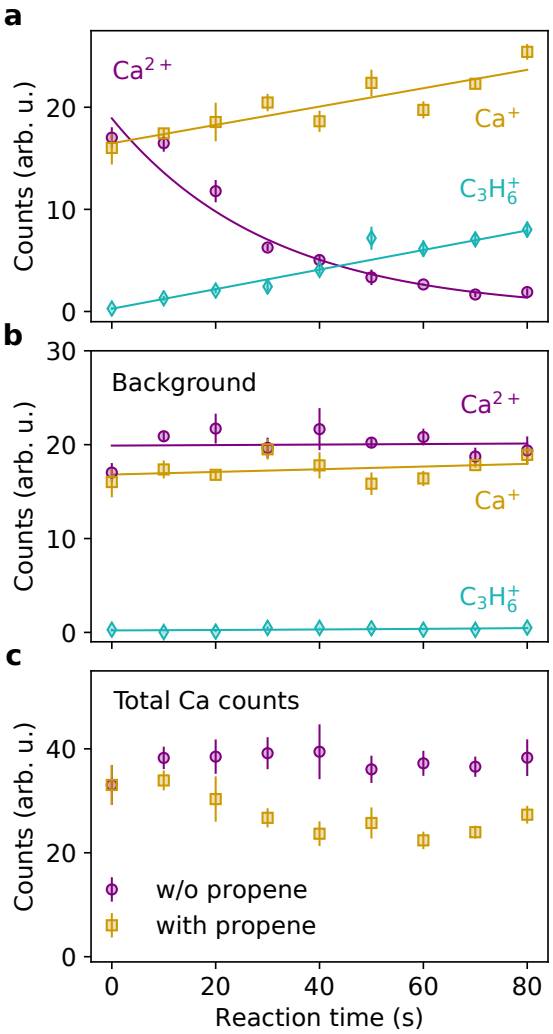

Figure 7.4: **Charge transfer kinetics**. Ion numbers of reactant and product ions extracted from high-resolution TOF-MS as a function of reaction time, with leaked propene gas (**a**) and without propene (**b**). The lines are fits based on the rate model described in the text. **c**, Comparison of the total Ca ion counts ($Ca^+ + Ca^{2+}$) with and without addition of propene gas during the rate measurement. Error bars are standard errors of four independent measurements.

7.4 Discussion and Conclusion

In order to decide which ionization method is more suitable for loading of propene in ion-molecule reaction studies, measurements of the stability of the loaded propene number were performed. Figs. 7.5a and b show measured $C_3H_6^+$ ion counts using VUV ionization and charge-transfer with Ca^{2+}, respectively. Propene was loaded using either method and the Coulomb crystal was then ejected into the TOF-MS for analysis. This was repeated 20 times for VUV ionization and 12 times for the charge-transfer reaction. Using the VUV method a loading time of 30 s produced a sufficient amount of $C_3H_6^+$. For the charge transfer method, however, propene had to be leaked into the chamber for at least 80 s to result in the same amount of trapped $C_3H_6^+$. The data show that both methods yield reproducible quantities of $C_3H_6^+$, with tolerable fluctuations about the mean (lines in Figs. 7.5a and b) of about 20%.

While VUV ionization allows a large number of propene ions to be loaded, largely independent of the Ca^+ crystal size (Fig. 7.2), charge transfer loading requires a large number of Ca^{2+} present. This limits the amount of $C_3H_6^+$ that can be loaded and the stability relies on that of the Ca^{2+} preparation. Based on these considerations, VUV ionization was found to be more efficient for loading $C_3H_6^+$ due to the reduced loading time and simpler experimental sequence.

In conclusion, two simple yet versatile methods were demonstrated to softly ionize propene leaked into the reaction chamber and subsequently load it into a trapped ion Coulomb crystal. First, direct photoionization using VUV light at 118 nm was employed. Second, a novel method was introduced in which doubly charged Ca^{2+} ions were reacted with neutral propene to form trapped $C_3H_6^+$ and Ca^+ by charge transfer. While both methods were found to be stable and reproducible, VUV ionization was chosen for further ion-molecule reaction experiments because of its speed and independence on Coulomb crystal size. Nevertheless, charge transfer loading is particularly suited for other molecular species whose ionization potential exceeds the VUV photon energy of 10.5 eV such that single photon ionization is not possible. The upper ionization energy limit for charge transfer is given by the ionization potential of Ca^+, i.e. 11.9 eV. Consequently, charge transfer represents a viable alternative to VUV photoionization if the required VUV wavelength is not readily available.

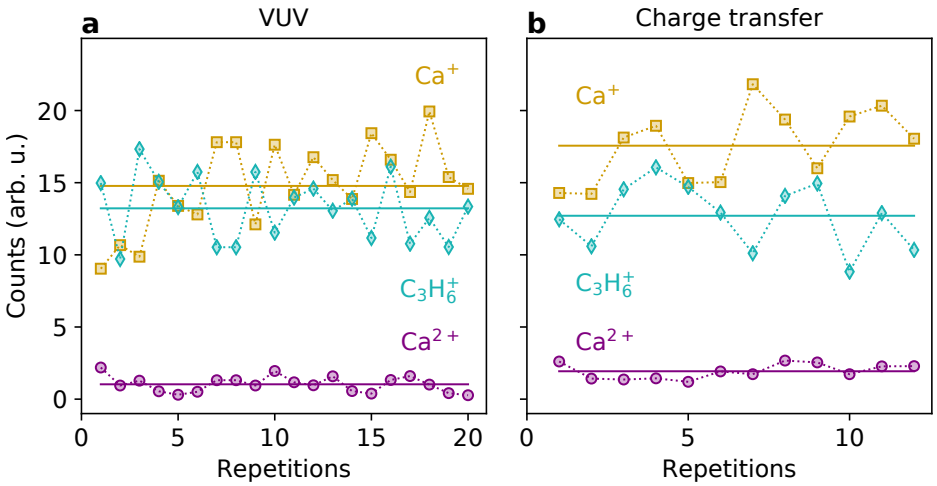

Figure 7.5: **Propene loading stability**. Number of trapped ions in multiple repetitions of the loading sequence using VUV photoionization (**a**) and charge-transfer (**b**).

8

Conformer-specific polar cycloaddition of *gauche*- and *s-trans*-DBB with trapped propene ions

Polar Diels-Alder cycloadditions are particularly fast and efficient routes for the formation of cyclic compounds. For these reactions, the question arises whether product formation proceeds via the canonical Diels-Alder mechanism in which only the *cis* conformer of the diene can react in a concerted pathway or via a stepwise process involving both *cis* and *trans* conformers. Using molecular-beam and ion-trap technology, we present a conformer-specific study of the polar cycloaddition of 2,3-dibromo-1,3-butadiene (DBB) with propene ions. We find that both conformers of DBB exhibit capture-limited rate constants towards propene ions which implies the contribution of a stepwise and barrierless reaction pathway in parallel to the canonical concerted mechanism. Our work marks the first step towards a rigorous systematic investigation of conformational effects in polar cycloadditions and other reactions relevant for synthetic chemistry under single-collision conditions in the gas phase.[1]

8.1 Introduction

It has been almost a century since O. Diels and K. Alder described the formalism of the $[4+2]$ cyclisation, now widely known as the Diels-Alder (DA) cycloaddition [24]. In this reaction, a conjugated diene and an alkene, the "dieneophile", react to form a cyclohexene compound. Since its discovery in 1928, it has become one of the key reactions in synthetic organic chemistry [25]. This reaction has proven to be very efficient in the synthesis of many natural products such as the steroid hormone cortisone [162], reserpine, a drug for treating high blood pressure [163], and the antibiotic tetracycline [164] among others.

The reaction pathway for a highly symmetric system is believed to proceed via a synchronous concerted transition state in which bond formation and bond breaking occur simultaneously [25, 26]. Since the transition state is stabilised by Hückel aromaticity [26], it is energetically more favourable than a stepwise mechanism with diradical intermediate. This explains why the DA reaction generally affords high stereo- and regioselectivity

[1] J. Wang is acknowledged for assistance with the measurements presented here.

of the cycloadduct and imposes that the reaction proceeds exclusively from the *s-cis* conformer of the diene and not from the *s-trans* conformer. However, this simple model tends to break down in cases where the reactants possess complex functional groups, such that an asynchronous or stepwise mechanism can also occur, allowing also the *s-trans* conformer to contribute to product formation [28].

The situation changes even more drastically for polar DA cycloadditions [29] where one of the reactants is charged. In the case of the $[4 + 1^+]$ polar cycloaddition, the removal of one electron from the dieneophile leads to a radical cation reaction with strong activation. Consequently, an aromatic transition state cannot be formed and instead a two-step mechanism has been suggested to be favoured [30, 31, 32]. This would allow both conformers to participate in the formation of the cycloadduct with significant rates. For this reason, information about the reaction mechanism could be obtained from studying the individual chemical reactivities of the *s-cis* and *s-trans* conformers of the diene. Under typical ambient conditions at room temperature and in solution, however, the conformers of dienes can often transform into each other by thermal rotation about the central bond of the 4π system. Hence, their isolation and separate chemical characterisation have remained elusive.

Besides synthetic chemistry, the understanding of ion-molecule reactions is also crucial to unravel the life cycle of organic compounds in the atmosphere and in space [54, 146, 55], where harsh conditions affect the reaction pathways. An abundance of organic compounds has been identified in the atmosphere of Saturn's moon Titan [165, 148], e.g. propene [166] and diacetylene [147], which shields the lower atmosphere from ultraviolet (UV) radiation of the sun and has been shown to photochemically react to form larger cyclic hydrocarbons through polar cycloaddition [167, 168].

A promising route for the investigation of ion-molecule reactions in a controlled environment has recently been established with experiments combining molecular beams [6, 7] with trapped and Coulomb-crystallized molecular ions [8, 9]. Molecular beams generated by supersonic expansions allow molecular vibrations and rotations to be cooled to very low temperatures, such that molecular conformations are preserved. Recently, the use of inhomogeneous electrostatic fields has enabled the spatial separation of different molecular conformations and rotational states based on their different electric dipole moments [10, 15]. Directing such a controlled molecular beam at a reaction target of trapped ions has enabled kinetic and mechanistic studies of individual conformers of aminophenol with Ca^+ ions [13], as well as nuclear-spin-selected water molecules with diazenylium ions (N_2H^+) [21]. These studies delivered experimental evidence that, for simple systems, reaction-rate constants can indeed strongly depend on molecular conformation or rotational states under single-collision conditions.

Here, we leverage these methods to investigate a complex organic reaction in the gas phase. We study the $[4 + 1^+]$ cycloaddition of individual molecular conformations of 2,3-dibromobuta-1,3-diene (DBB) with ionic propene ($C_3H_6^+$) to form the 1,2-dibromo-4-methyl-cyclohexene radical cation (Fig. 8.1a) as a prototypical polar cycloaddition reaction. DBB exists in an apolar *s-trans* and a polar *gauche* conformation the successful electrostatic separation of which we recently reported in Ref. [33]. In conformer-specific reaction experiments reported here we find that both the *gauche* as well as the *s-trans* conformer exhibit capture-limited reaction rate constants of comparable magnitude towards propene ions. The observation of a faster reaction rate of the *gauche* conformer can

be traced back to its stronger long-range interaction with the ion. This finding implies the absence of a potential energy barrier due to transition states for either conformer, in agreement with ab-initio calculations, and implies the existence of an efficient stepwise reaction pathway competing with the canonical concerted mechanism.

8.2 Results

8.2.1 Experimental setup

The experimental setup is shown in Fig. 8.1b. An internally cold beam of the neutral diene DBB in neon carrier gas was prepared by a pulsed supersonic expansion (see chapter 2 and ref. [21]). The collimated beam passed through an electrostatic deflector where a strong electric field gradient induced a spatially varying Stark-energy shift [6] in polar molecules. This resulted in a vertical force applied to the polar *gauche*-DBB species (dipole moment $\mu_{\text{gauche}} = 2.3$ D, cf chapter 5) which was deflected from the original beam axis in contrast to the unpolar *s-trans*-DBB conformer ($\mu_{\text{trans}} = 0$) which were not perturbed.

The conformer-selected molecular beam was then directed at a linear-quadrupole ion trap (LQT) which contained a Coulomb crystal of laser-cooled Ca^+ ions [9], the fluorescence of which was imaged onto a charge-coupled device (CCD) camera (Fig. 8.1c). The Ca^+ Coulomb crystal served as a reservoir to sympathetically cool propene$^+$ ions and other product ions formed during the reaction [17, 9].

The Coulomb crystals formed a stationary target for the DBB molecular beam. By vertically tilting the molecular beam apparatus, different parts of the DBB beam were overlapped with the ions in the trap, entailing reactions with samples of different compositions of the *gauche* and *s-trans* conformers of DBB. This allowed us to study the influence of the DBB conformation on the cycloaddition kinetics taking place in the ion trap. The reaction kinetics are measured by ejecting the trapped reactant and product ions into an integrated time-of-flight mass spectrometer (TOF-MS).

8.2.2 Conformer separation of DBB

We first characterised the molecular beam of DBB by measuring its density profile along the vertical deflection axis, yielding a deflection profile. For this purpose, the DBB molecules were ionised with a vacuum-ultraviolet (VUV) radiation source at the centre of the ion trap and subsequently ejected into the TOF-MS to determine the ion number. Fig. 8.2a shows the beam-density profiles obtained as a function of the deflection coordinate y measured with deflection off (deflector voltage 0 kV) and deflection on (deflector voltage 13 kV). The undeflected beam (grey symbols in Fig. Fig. 8.2a) containd a 1:3.3 mixture of the *gauche* and *s-trans* conformers of DBB, respectively, set by the thermal equilibrium in the room temperature reservoir from which the molecular beam emanates [33]. Switching on the deflector separated the polar *gauche* conformer from the apolar *s-trans* conformer which leads to the appearance of a shoulder in the beam profile towards larger deflection coordinates (purple symbols in Fig. 8.2a). The data are well reproduced by Monte-Carlo trajectory simulations of the molecular beam (lines in Fig. 8.2a) assuming a rotational temperature of 1 K and independently measured beam

velocity $v_{\mathrm{beam}} = 843(58)$ m/s [33]. These results confirm that electrostatic deflection generated regions with almost pure *s-trans* and pure *gauche* conformer population at low and high deflection coordinates, respectively. We used the simulations in order to determine the conformer populations as a function of deflection coordinate (see Fig. 8.2b) and identify four positions, marked I–IV in Figs. 8.2a and b, that corresponded to DBB samples with populations p_t of the *s-trans* conformer ranging from 1 to 0, respectively. Position II refers to the undeflected molecular beam (deflector voltage 0 kV) containing

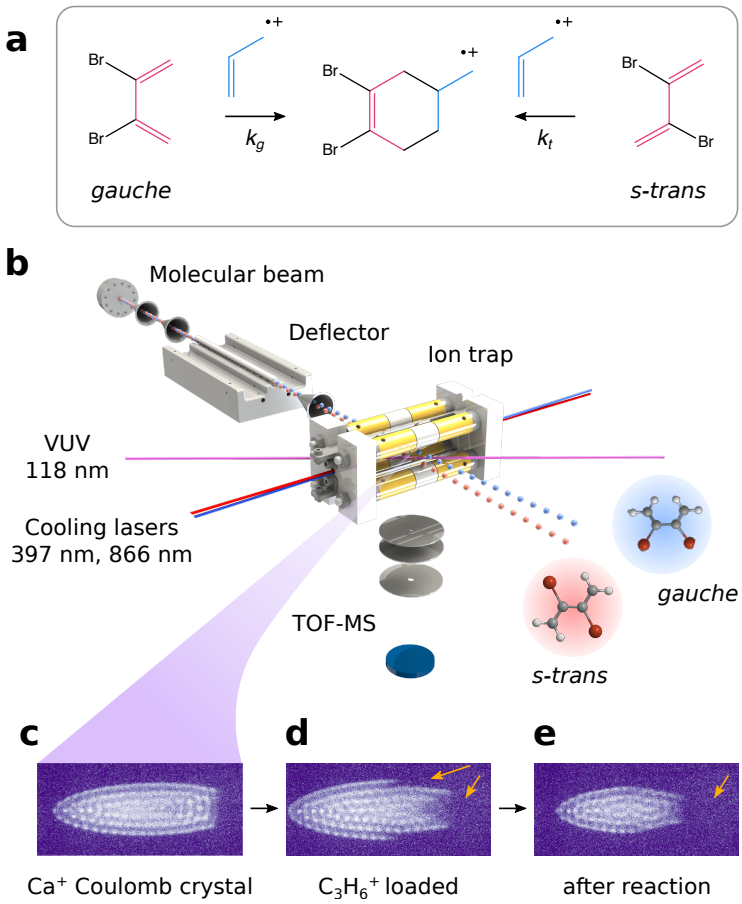

Figure 8.1: **Overview of the experiment.** **a**, Scheme of the polar cycloaddition reaction between the *gauche* and *s-trans* conformers of DBB with propene ions, each exhibiting a different reaction rate constant k_g and k_t, respectively. **b**, Schematic of the experimental setup. The two conformers of DBB are separated by electrostatic deflection in a molecular beam and directed at an ion trap holding the propene ions. Reaction kinetics are measured by ion extraction into a time-of-flight mass spectrometer (TOF-MS). **c**–**e**, Fluorescence images of laser-cooled Ca^+ Coulomb crystals at different stages of the experiment: **c** shows the initial, pure Ca^+ crystal, **d** shows an image after loading propene ions by vacuum-ultraviolet (VUV) photoionization of propene, and **e** is a typical image obtained after the reaction with DBB. Arrows indicate regions where ions heavier than Ca^+ accumulate in the trap.

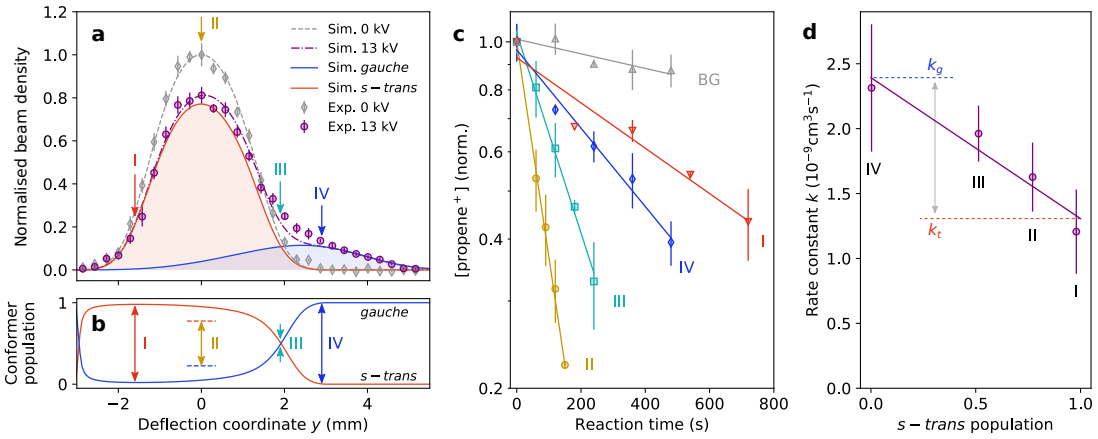

Figure 8.2: **Conformer-specific reaction rate constants. a**, Measurement of the DBB beam-density profile along the deflection coordinate for deflector voltages 0 kV and 13 kV. The experimental data (symbols) are in good agreement with Monte-Carlo trajectory simulations (lines) which show the separation of the two conformers. **b**, Populations of the conformers as a function of deflection coordinate in the molecular beam obtained from the trajectory simulations. **c**, Reaction kinetics measured in terms of the propene ion concentration (normalised to its initial value) as a function of reaction time for the four positions I–IV marked in **a, b** and a background measurement (BG). The exponential decay of the propene-ion concentration implies a bimolecular reaction with pseudo-first-order kinetics. **d**, Bimolecular rate constants extracted from the pseudo-first-order rate-constant measurements as a function of the *s-trans*-conformer population. The line is a linear fit. Error bars correspond to the standard deviation of three independent measurements.

a thermal mixture of the conformers ($p_t = 0.77$). At positions I and IV, almost pure samples of *s-trans* and *gauche*-DBB were obtained.

8.2.3 Reaction rate measurements

Exploiting the control over the molecular conformation of DBB, we perform reaction experiments at the molecular beam positions I–IV targeting the ion Coulomb crystal. The experimental sequence started by loading a Coulomb crystal of about 10^3 laser-cooled Ca^+ ions into the LQT. Then, propene ions were loaded into the trap by leaking propene gas into the vacuum chamber at a partial pressure of 3×10^{-9} mbar and photoionising propene molecules by VUV radiation at 118 nm. Due to their larger mass, the propene ions localised at the extremities of the Ca^+ crystal as evidenced by a change of shape of the Ca^+ crystal (Fig. 8.1d).

The reaction between the propene ions and the DBB molecules was initiated by switching on the pulsed molecular beam. After a variable reaction time, the molecular beam was switched off and the ions were ejected into the TOF-MS to determine the number of remaining propene ions. To discriminate between Ca^+ (mass 40 u) and $C_3H_6^+$ (mass 42 u), the TOF-MS was operated in a high-resolution mode with limited mass range [61]. A typical Ca^+ fluorescence image after reaction is depicted in Fig. 8.1e,

showing a slight reduction of the number of Ca^+ ions and a spatial rearrangement of the crystal due to trapped product ions.

Fig. 8.2c shows measurements of $C_3H_6^+$ ion counts after reaction with DBB at the four molecular beam configurations I–IV as a function of reaction time. To account for loss of propene ions due to collisions and reactions with background gas, we also recorded a background data set for each molecular-beam configuration where the beam is adjusted such that it does not hit the Coulomb crystal. One exemplary background measurement is shown as the grey data points in Fig. 8.2c. Loss of propene ions due to collisions with neon from the molecular beam was found to be negligible. All reaction measurements exhibited an exponential decay of the number of propene ions with time which implies the validity of a pseudo-first-order rate law for the bimolecular reaction, as expected for a constant DBB density replenished by the molecular beam. In particular, this means that reaction of trapped propene ions with products of the reaction does not occur.

The pseudo-first order rate constants $\tilde{k}_i$ at each beam position $i = \mathrm{I}, \ldots, \mathrm{IV}$, were obtained from a fit of an exponential decay function to the data and subtraction of the corresponding background rate constant. Bimolecular rate constants $k_i = \tilde{k}_i / n_i$ were calculated using the DBB beam densities n_i determined from the relative beam density profile measurement of Fig. 8.2a and an independently measured absolute DBB density of $n_{\mathrm{avg}} = 3.9(5) \times 10^6$ cm^{-3} at $y = 0$ and deflector voltage 13 kV (see section 2.4.4.2).

8.2.4 Conformer-specific rate constants

The bimolecular rate constant for the depletion of propene ions via the reactions Fig. 8.1a can be modelled as a linear combination $k_i = p_{\mathrm{g},i} k_{\mathrm{g}} + p_{\mathrm{t},i} k_{\mathrm{t}}$ of the rate constants $k_{\mathrm{g/t}}$ of the individual *gauche*/*s-trans*-conformers, respectively. The weighting factors $p_{\mathrm{g/t},i}$ are the respective conformer populations at molecular beam position i. Fig. 8.2d shows the measured bimolecular rate constants k_i as a function of the *s-trans* population p_{t} obtained from the Monte-Carlo trajectory simulations (Fig. 8.2b). The solid line is a least-squares fit using the above linear model for k_i and achieves good agreement with the experimental data within the error bars. The fit yields the bimolecular reaction rate constants $k_{\mathrm{g}} = 2.4(5) \times 10^{-9}$ cm^{3}s^{-1} for the *gauche*-conformer and $k_{\mathrm{t}} = 1.3(6) \times 10^{-9}$ cm^{3}s^{-1} for the *s-trans*-conformer, which implies a relative difference $r = 2(k_{\mathrm{g}} - k_{\mathrm{t}})/(k_{\mathrm{g}} + k_{\mathrm{t}}) = 0.6(1)$ by which the *gauche*-conformer reacts faster than the *s-trans*-conformer.

8.2.5 Reaction products

To gain information about the products of this reaction, we recorded mass spectra at low resolution for a wide mass range of the trapped ions after 2 minutes reaction time. This measurement was performed in configuration II where the largest beam density enabled faster data acquisition. The full mass spectrum, averaged over 50 experiments, is depicted in Fig. 8.3a. Due to a combination of the strong exothermicity of the reaction (≈ 60 kcal/mol) and the constant presence of visible and near-ultraviolet laser light used to cool Ca^+, both of which are likely to promote fragmentations, only fragments of the cycloadduct (254 u) could be observed. This is consistent with the behaviour observed in radical cation reactions of similarly sized systems as described in,e.g., Ref. [31]. The dominant peak due to Ca^+ (40 u) was used for calibration of the mass spectra. An expanded view of the product fragment spectrum is displayed in Fig. 8.3b along with a

comparison with control experiments either without propene ions in the trap (negative blue trace) or without DBB in the molecular beam (negative grey trace) under otherwise identical conditions. The mass spectrum can be grouped into several bands labelled with capital letters A–F. The bimodal structure of the peaks in the mass spectrum results from ions heavier than Ca^+ forming extensive shells around the Ca^+ Coulomb crystal, so that they feel different extraction fields at different locations in the trap when accelerated into the TOF-MS. The exact position and shape of the signals in the TOF-MS is therefore sensitively dependent on the shape and composition of the multicomponent Coulomb crystals. The assignment of the signals in the TOF-MS to specific molecular compounds was therefore based on detailed molecular dynamics (MD) simulations of the ejection of the mixed species Coulomb crystals into the TOF-MS (cf. section 2.3.5).

MD simulations of a Coulomb crystal consisting of 500 Ca^+ ions (mass 40 u) and 20 ions of each of the masses 42 u ($C_3H_6^+$), 50 u, 51 u, 52 u, 57 u, 72 u, 79 u, 92 u and 120 u was performed[2]. A comparison of the experimental data with the simulation is shown in Fig. 8.4. The simulated TOF signals are shown in different colours to highlight

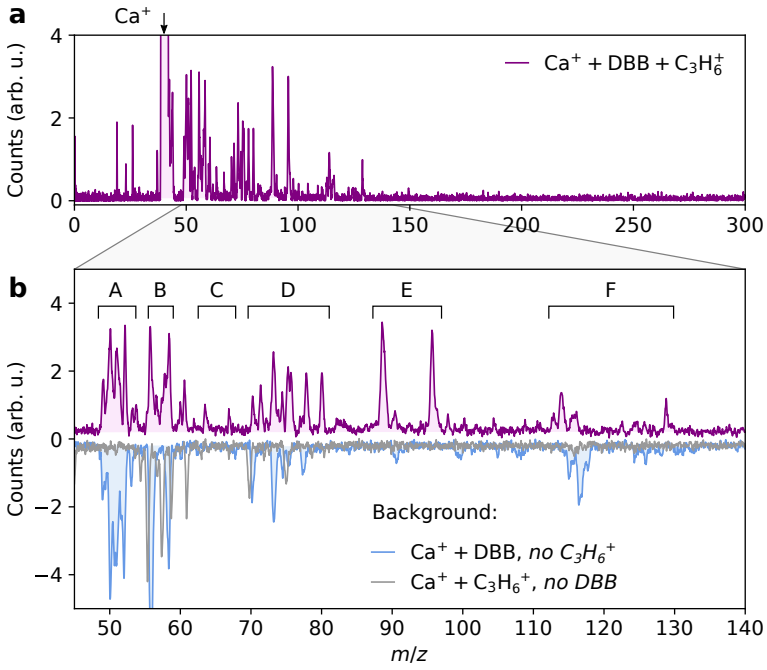

Figure 8.3: **Reaction product mass spectra.** **a**, Overview time-of-flight mass spectrum acquired over a large mass range showing a strong signal for Ca^+ at 40 u and several product fragments. No signal could be detected at the expected mass of the cycloadduct at 254 u due to fragmentation. **b**, Magnified view of the mass range showing the product fragments (top trace) and comparison with control experiments in which either propene ions or DBB were absent from the experiment (lower inverted traces). The spectrum consists of several bands A–F corresponding to different fragments of the cycloadduct, see text for details.

[2]MD simulations were performed by L. Xu.

the contribution from each mass. A global offset was added to the time-of-flight of the simulated spectrum in order to match the location of the Ca^+ peak in the experimental data. An overall good agreement between experiment and simulation is obtained. In particular, the simulated splittings of the individual mass signals are well reproduced in the measured TOF spectra. Small differences in the splittings and positions of the peaks in the simulation are attributed to different sizes and compositions of the Coulomb crystal in the experiment and simulations and to the presence of additional heavy ion species which are not accounted for in the simulations. The good agreement between data and simulation allows the assignment of the mass bands A–F in Fig. 8.3b to different molecular compounds (see table 8.1).

The first two bands A and B are attributed to $C_4H_n^+$ (50–52 u) and $CaOH^+$ (57 u), respectively, which are also present in the control experiments. This shows that $C_4H_n^+$ fragments are formed due to reactive collisions between Ca^+ and DBB. Similarly, the

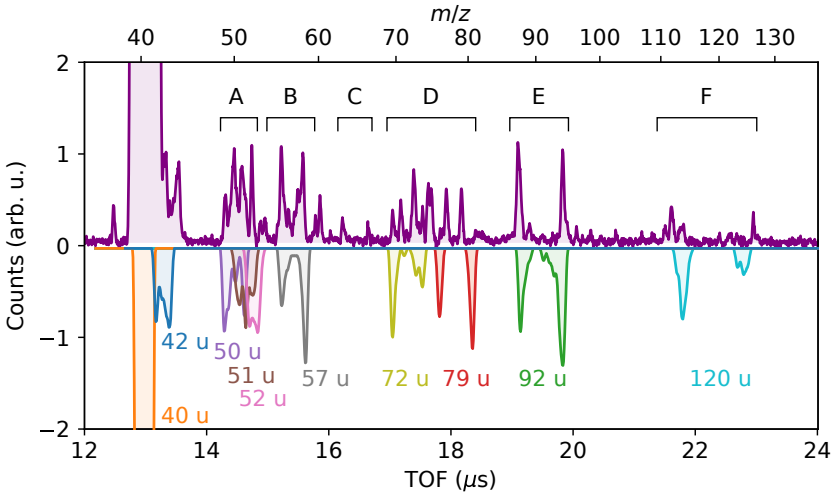

Figure 8.4: **Comparison of experimental and simulated TOF mass spectra.** The positive curve shows an experimental spectrum while the inverted trace shows a simulated spectrum for 500 ions with mass 40 u and 20 ions of each of the masses 42, 50,51,52, 57, 72, 79, 92 and 120 u, highlighted in different colours. The bands A–F correspond to those of Fig. 8.3b.

Table 8.1: Assignment of molecular compounds to the TOF bands based on the MD simulation.

Label	Assigned masses (u)	Possible compounds
A	50,51,52	$C_4H_n^+$, n=2,3,4
B	57	$CaOH^+$
C	66	$C_5H_6^+$
D	72	CaO_2^+
D	78, 79	$C_6H_n^+$, n=6,7
E	92	$C_7H_8^+$
F	119, 121	$CaBr^+$

band F is assigned to $CaBr^+$ (119 u and 121 u) which is also formed in the control experiment where $C_3H_6^+$ is absent. $CaOH^+$ is likely formed in a reaction of the Ca^+ ions with residual H_2O background gas in the vacuum chamber.

Masses of the product fragments of the reaction of DBB with the propene ions appear in the bands C,D and E. To explain the observed fragments, we propose fragmentation pathways as displayed in Fig. 8.5. The fragmentation of substituent groups from unstable products of radical cation reactions, such as -H, -CH_3 and even CH_3OH, have been observed before for a range of gas phase reactions [31, 168, 169, 170, 171]. A possible fragmentation scheme of the primary cycloadduct of the title reaction (Fig. 8.1a) is shown in Fig. 8.5. In the first step of the proposed mechanism, a protonated toluene ion is formed through Bromine loss, which is the branching point for three subsequent fragmentation pathways. The protonated toluene ion has been observed to fragment by either hydrogen loss, forming a toluene fragment (92 u), or through elimination of a methyl group, forming a benzyl fragment (78 u) [172, 173, 174]. Alternatively, a skeletal rearrangement, possibly involving the tropylium ion, followed by elimination of an ethyl group could result in the formation of a five-membered ring (66 u)[175, 176, 177].

The strongest signal of Fig. 8.3b is observed in band E and can be attributed to a $C_7H_8^+$ (92 u) fragment of the cycloadduct $C_7H_{10}Br_2^+$, after removal of the two bromines and two hydrogens. Band D has a more complicated structure and is likely explained by the presence of $C_6H_6^+$ (78 u) and $C_6H_7^+$ (79 u). We note that a Br^+ signal is absent in the control experiments, but impurities, potentially due to CaO_2^+ [64], appear towards lighter masses. Finally, band C is consistent with the fragment $C_5H_6^+$ (66 u) which is formed by rearrangement and abstraction of C_2H_2 from a $C_7H_{10}^+$ (94 u) intermediate. The gradual decrease of signal intensity with decreasing mass from bands E to C could also point to a slow stepwise fragmentation under abstraction of CH_n groups. In summary, the

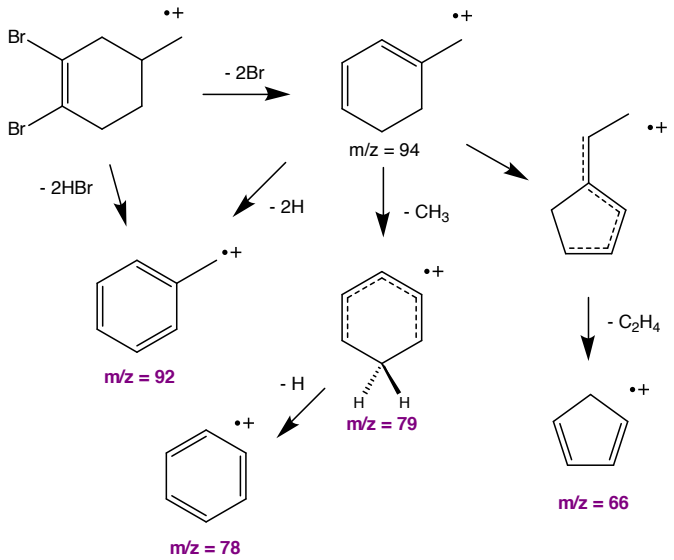

Figure 8.5: **Proposed fragmentation channels of the cycloadduct of the reaction of DBB with propene ions.** The masses highlighted in purple are observed in the TOF mass spectrum Fig. 8.3b.

observation of all of these fragments strongly suggests that the DA cycloadduct is indeed formed in the reaction of DBB and propene ions.

8.3 Discussion

Our experimental data show a strong reactivity of the propene ions with both conformers of DBB. A pronounced enhancement of the reaction rate is observed if DBB is present in the *gauche* conformation. In order to understand the origin of this difference in reactivity, quantum chemical calculations of the potential energy surface (PES) of this reaction were performed[3] using density functional theory [96] (Fig. 8.6a). Contrary to the experiment, this calculation was done for the reaction $DBB^+ + C_3H_6$ with a charge on DBB instead of propene. Since propene has a larger ionization potential than DBB (cf. Table 4.1), this corresponds to the ground state PES. It is thus likely, that the experimentally studied reaction $DBB + C_3H_6^+$, with 10.5 kcal/mol higher reactant energy, first undergoes a charge exchange and then proceeds on the $DBB^+ + C_3H_6$ PES. Whether this is indeed the case is still under investigation.

The ground-state PES in Fig. 8.6a shows multiple reaction pathways for either conformer. For *gauche*-DBB, there are two direct, barrierless pathways via the concerted $M1^+$ configuration to the *endo* and *exo* forms of the cycloaddition product. There is also a stepwise pathway that joins with the pathway for the *s-trans* conformer at the intermediate INT^+. From INT^+, the products are reached via a submerged energy barrier, either via a transition state TS^+ or via $M1^+$. In the *s-trans* pathway, isomerization from the *s-trans* to the *gauche* form of butadiene occurs from INT-tr^+ to INT^+ without a significant barrier.

On these grounds, it can be concluded that two reaction pathways compete: a concerted one for the *gauche* conformer, and a stepwise one for the *s-trans* species. While the former seems barrierless, the latter exhibits a transition state which, however, is submerged by ≈ 25 kcal/mol with respect to the energy of the reactants. Hence, it can be expected that this saddle point will not constitute a significant dynamic bottleneck for the reaction so that also the *s-trans* pathway can effectively regarded to be barrierless.

Motivated by these findings, the reaction kinetics were modelled using rotationally adiabatic quantum capture theory for barrierless ion-molecule reactions [56, 58]. Within this framework, it is assumed that due to the absence of a barrier the reaction proceeds with unit probability (Fig. 8.6a), such that its overall rate is governed by the long-range interaction between the ionic and neutral collision partners. Figs. 8.6b and c show rotationally adiabatic, centrifugally corrected long-range interaction potentials for collisions of $C_3H_6^+$ with *gauche*- and *s-trans*-DBB, respectively. They include the coupling of the ionic charge to the induced and permanent dipole moments of the neutral counterpart. The three sets of curves correspond to different values of the total collisional angular momentum quantum number J which gives rise to a centrifugal energy barrier. The individual curves for each value of J correspond to all rotational quantum states of DBB with rotational angular momentum quantum number $j = 4$, which is calculated to exhibit the strongest population in the molecular beam.

Within the formalism of Refs. [56, 58] (cf. section 1.4.3), unit reaction probability is

[3] The density functional theory calculations were performed by U. Rivero.

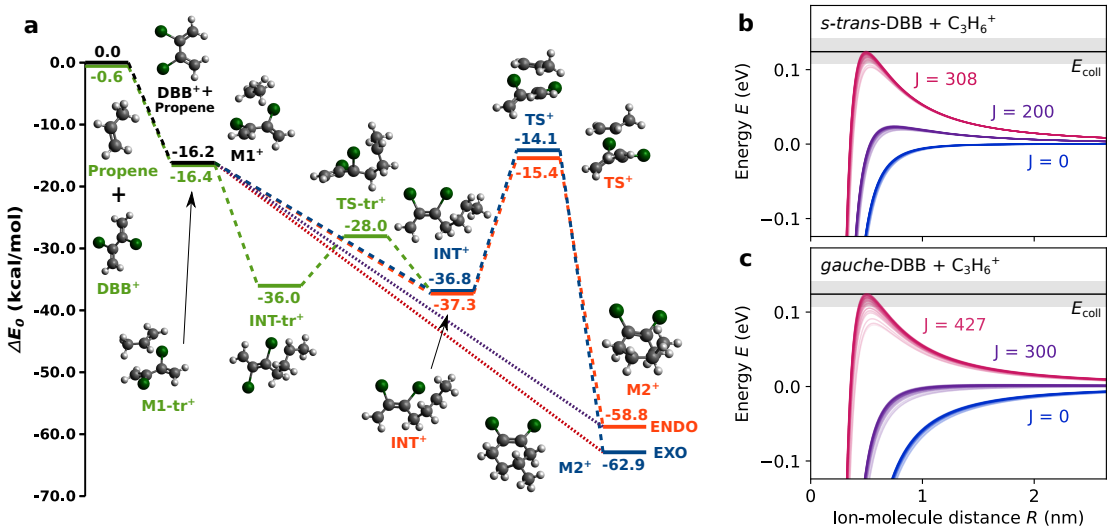

Figure 8.6: **Theoretical potential-energy profile of the reaction and long-range ion-molecule interaction potentials**. **a** Potential-energy profile of the polar cycloaddition of DBB with $C_3H_6^+$ showing a concerted reaction pathway for the *gauche* conformer and a stepwise mechanism for the *s-trans* species. Dashed (dotted) lines belong to pathways with (without) an energy barrier. **b,c** Rotationally adiabatic, centrifugally corrected long-range interaction potentials for the reaction of *s-trans*- (**b**) and *gauche*-DBB (**c**) with propene$^+$ for different values of the total collisional angular momentum quantum number J. Each value of J comprises a set of lines corresponding to all rotational states of DBB with rotational angular momentum quantum number $j = 4$, which has the highest thermal population. The collision energy E_{coll} is drawn as the black horizontal line and the grey-shaded areas show its experimental uncertainty.

assigned to any collision with $J < J_{\mathrm{max}}$, where J_{max} is the maximum angular momentum quantum number for which the centrifugally corrected interaction energy does not exceed the experimental collision energy $E_{\mathrm{coll}} = 124(17)$ meV (black solid line in Figs. 8.6b,c). The plots show that the centrifugal barrier grows faster with J for *s-trans*-DBB than for *gauche*-DBB such that the maximum collisional angular momenta for a reactive encounter are $J_{\mathrm{max,t}} \approx 308$ and $J_{\mathrm{max,g}} \approx 427$, respectively, implying a larger cross-section $\sigma \propto J_{\mathrm{max}}^2$ [58] for *gauche*-DBB. For the lowest values of J, one notices a steeper slope of the ion-molecule potential for *gauche*-DBB. This points to a stronger attractive interaction between the ion and the permanent dipole of *gauche*-DBB as opposed to the apolar *s-trans* conformer and explains the observed difference in conformer-specific reaction rates. Also, the rotational quantum state of DBB is found to affect the polar *gauche* conformer more strongly than the unpolar *s-trans* conformer. As a result, AC theory predicts bimolecular rate constants of $k_{\mathrm{AC,g}} = 2.44 \times 10^{-9}$ cm^{3}s^{-1} for *gauche*-DBB and $k_{\mathrm{AC,t}} = 1.26 \times 10^{-9}$ cm^{3}s^{-1} for *s-trans*-DBB, in very good agreement with the measured values. The calculated relative difference of reaction rates between the *gauche* and *s-trans* conformers is $r_{\mathrm{AC}} = 0.64$ and agrees well with the experimental value $r = 0.6(1)$.

8.4 Conclusion

In conclusion, we have presented experiments that probe the chemical reactivity of individual molecular conformers of 2,3-dibromobutadiene in a prototypical polar cycloaddition reaction with propene ions. The current study represents the first application of using conformationally controlled molecular beams and ion-trap methods to the study of complex organic reactions under single-collision conditions in the gas phase. Our measurements show that both the *gauche* as well as the *s-trans* conformers of DBB exhibit capture-limited rate constants, in contrast to the canonical Diels-Alder mechanism in which only the *gauche* conformer is expected to react in a concerted reaction pathway. The almost twofold larger rate constant for the *gauche* as compared to the *s-trans* conformer could be explained by the attractive long-range ion-dipole interaction of the former with the propene ions, in very good agreement with a theoretical modelling by an adiabatic capture model.

The fact that both conformers of DBB exhibit capture-limited reaction rates towards propene$^+$ means that energy barriers along the reaction coordinate, that would indicate the presence of a pericyclic transition state, are absent or negligible. This is consistent with the established knowledge that polar cycloadditions proceed much faster than their neutral counterparts [31, 28] and thus provide efficient routes in synthetic chemistry [30]. The observed strong reactivity for both molecular conformations of the diene in conjunction with quantum-chemical calculations strongly suggests the existence of an efficient stepwise pathway for the cycloaddition.

Our experimental setup represents a unique platform to probe chemical kinetics and dynamics with individual molecular conformers and isomers in fundamental organic model systems. In combination with precise spectroscopic tools, this capability opens up a wide range of opportunities for the investigation and validation of reaction mechanisms.

9

Conclusion and Outlook

In this thesis, the reaction kinetics of rotational-state-selected and conformer-selected neutral molecules with sympathetically cooled molecular ions were explored successfully. By sending an internally cold molecular beam through an electrostatic deflector, spatial separation of these molecules according to their effective dipole moment was achieved. This enabled the preparation of molecular beams with selected molecular conformers or rotational states. To study their individual chemical reactivity, this controlled molecular beam was directed at a stationary reaction target of Coulomb-crystallized ions in an ion trap. The resulting reaction kinetics and reaction products were analyzed using a high-resolution time-of-flight mass spectrometer coupled to the ion trap.

In a first experiment, the proton-transfer reaction of the spatially separated *para*- and *ortho*-water in their absolute rovibrational ground states with trapped and sympathetically cooled ionic diazenylium ions (N_2H^+) was investigated. A 23(9)% larger reaction rate constant for the *para* nuclear-spin isomer was measured. This was found to be in quantitative agreement with a modelling of the reaction kinetics using rotationally-adiabatic capture theory. Hence, the larger chemical reactivity of *para*-water could be attributed to the smaller degree of rotational averaging of the ion-dipole long-range interaction compared to the *ortho*-species. This is a consequence of the generalized Pauli principle, which imposes that the ground state of *ortho*-water is rotationally excited, while that of *para*-water is the absolute rotational ground state.

To investigate more complex organic ion-molecule reactions in the gas-phase, a VUV light source was implemented for soft photoionization of larger molecules without fragmentation. VUV ionization was used to verify the electrostatic deflection of the *gauche*- and *s-trans*-conformers of DBB in a molecular beam, as predicted by quantum-chemical calculations, and paved the way for conformer-selected reaction studies.

Subsequently, the conformer-selected molecular beam of DBB was employed for reaction experiments with trapped and laser-cooled Ca^+ ions. In this experiment, next to the molecular conformation of DBB, also the electronic state populations of Ca^+ could be controlled by virtue of the cooling and repumping laser settings. Rate measurements of DBB with the laser-driven Ca^+ ions revealed different kinetics for the two conformers. Ca^+ was found to react with *gauche*-DBB predominantly from its excited electronic states, whereas the reaction from the ground state was found to be inhibited. For *s-trans*-DBB, a capture-limited rate constant was measured regardless of the electronic

state of Ca^+. These results demonstrate a strong conformational effect at the level of the short-range ion-molecule potential energy surface, even though the reaction involves a highly activated radical cation.

Finally, by loading propene ions into the ion trap, a prototypical $[4 + 1^+]$ polar cycloaddition reaction with conformer selected DBB could be investigated. This experiment represents the first application of conformationally controlled molecular beams and ion-trap methods to the study of complex organic reactions under single-collision conditions in the gas phase. The measurements showed that both conformers exhibit capture-limited reaction rates. An almost twofold larger rate constant for the polar *gauche* conformer resulted from its stronger long-range interaction with the ion. The observed strong reactivity for both molecular conformations of the diene in conjunction with quantum-chemical calculations strongly suggests competing concerted and stepwise pathways for the polar cycloaddition.

Looking forward, there are a lot of opportunities for refinement of the experimental apparatus as well as new reactions to explore. Detection of product and reactant ions via TOF-MS is a key ingredient to reaction kinetics experiments with Coulomb crystals. Consequently, implementing a high-resolution TOF-MS that acts over a wide bandwidth is crucial for the success of this approach. In the experiments presented here, high mass-resolution was only available in a narrow mass window [61]. Following recent technical advances [71], applying higher voltages on the LQT end caps during the ion extraction will enable the required high-resolution to detect product ions in a wide mass range. This will lead to a significant improvement of signal-to-noise and facilitate product identification, such that the entire kinetics involving possible intermediates can be traced throughout the reaction [62].

Another improvement of the experimental setup, that is currently being undertaken, is the implementation of a dual-valve system for the molecular beam apparatus. This enables the rapid interchange between two molecular beams with distinct species such that the conformers of both reactants in an ion-molecule reaction can be controlled. By electrostatic deflection, individual molecular conformers from the first beam can selectively be ionized and loaded into the ion trap. Subsequently, they can be reacted with another selected neutral conformer of the second beam. With this technique, a significantly broader class of organic ion-molecule reactions can be investigated under controlled conditions. Alternatively, rovibrational-state-selective ionization [178, 179, 15] or conformer-selective ionization [13] can be used for control over the internal state of the ionic reaction partner.

An interesting molecule for future experiments is methyl vinyl ketone (MVK, IUPAC: But-3-en-2-one) which exists in two stable conformations: a syn-periplanar (*sp*, cis double bonds) and an anti-periplanar (*ap*, trans double bonds) conformer [180] (see Fig. 9.2). MVK is known for its utilization in the synthesis of steroids [23]. It also appears as one of the Criegee intermediates in the ozonolysis of isoprene, the second most abundant volatile organic compound in earth's atmosphere, and is believed to be a major source of highly reactive hydroxyl radicals (OH) [181, 180, 182, 183]. The two conformers of MVK exhibit different dipole moments making them suitable for electrostatic separation. The dipole moments are $\mu_e = 3.91$ D for *ap*-MVK and $\mu_e = 3.26$ D for *sp*-MVK [180]. Despite the fairly similar dipole moments, the two conformers can be separated by electrostatic deflection, as simulated deflection profiles presented in Fig. 9.1a show.

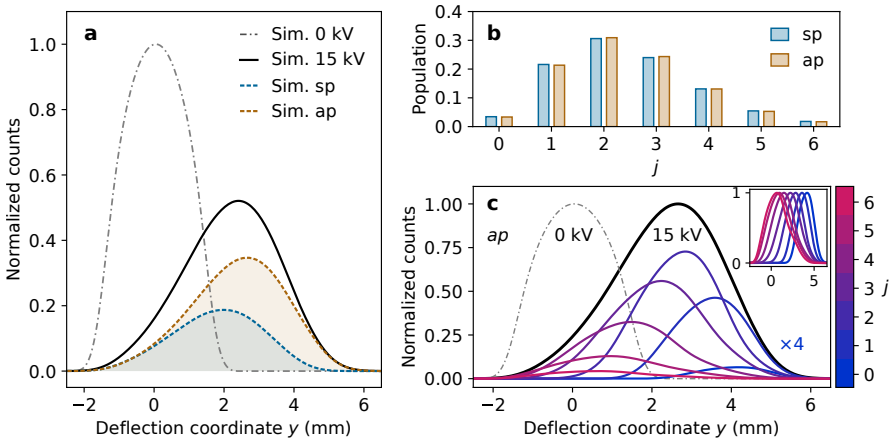

Figure 9.1: **Simulation of eletrostatic deflection for MVK. a**, Deflection profile simulation for MVK at a rotational temperature of 1.5 K for two deflector voltages of 0 and 15 kV. **b**, rotational state populations for *sp*- and *ap*-MVK. **c**, individual contributions of the rotational states j to the deflection profile of *ap*-MVK.

The simulation assumed a beam velocity of 1800 m/s, corresponding to a supersonic expansion in He. At room temperature (298 K), the thermal populations are 31% for the *sp*-conformer and 69% for the *ap*-conformer. The simulation shows that *ap*-MVK is more strongly deflected than *sp*-MVK, resulting in regions of pure beams of *ap*-MVK. Assuming similar conditions as for DBB (cf. chapter 5), the simulations were done at a rotational temperature of 1.5 K, at which only rotational states up to $j = 5$ are significantly populated (Fig. 9.1b). The individual contributions of the rotational states to the deflection profile are displayed in Fig. 9.1c, showing that only states with low values of j are significantly deflected. A similiar behaviour was observed for *sp*-MVK. These simulations demonstrate that beams with well known ratios of the two conformers can be obtained making this molecule a good candidate for future studies of conformer-selective reactions.

One possible application is the study of a heterogeneous Diels-Alder cycloaddition, in which a ring is formed that contains a non-C member. Here, MVK could be be reacted with either MVK or propene ions (Fig. 9.2). In both cases VUV could be employed to ionize the dienophile species for loading into the ion trap.

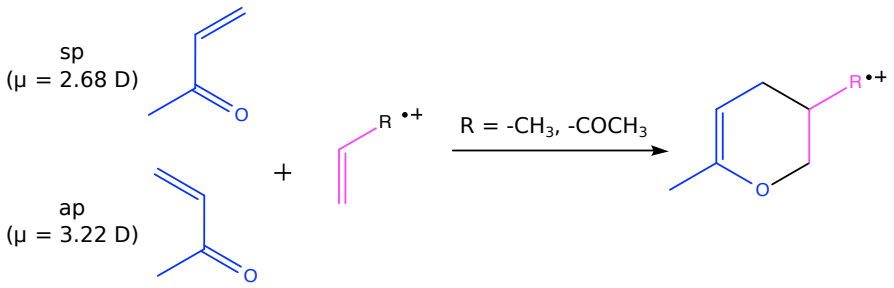

Figure 9.2: Possible reactions of MVK with MVK or propene ions.

Another important aspect of the Diels-Alder cycloaddition that could be easily studied in the curent setup is the stereospecificity of the dienophile [22]. An interesting example would be the reaction of cyclopentadiene with a symmetrically disubstituted dienophile (see Fig. 9.3). Here, -X would preferably be an electron-withdrawing substituent like e.g. -CN or -CO.

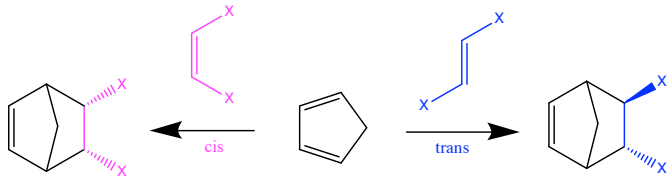

Figure 9.3: Stereospecific reactions of cyclopentadiene with *cis* and *trans* disubstitued dienophile.

With the present setup, a corresponding ion-molecule reaction could be studied where either the diene or the dienophile is ionized prior to reaction. Electrostatic deflection could be used to select either of the two conformers of the dienophile. Instead of cyclobutadiene, also conformer-selected *gauche*-DBB could be used.

Finally, one could explore the sterespecificities of cheletropic cycloadditions such as the reaction of butadiene with SO_2 (see Fig. 9.4). In this type of cycloaddition, the diene forms two new bonds to the same atom of another reactant molecule, here SO_2. This example is similar to the ion-molecule reaction DBB + Ca^+ investigated in this work, which was observed to exhibit strong conformation-dependent kinetics.

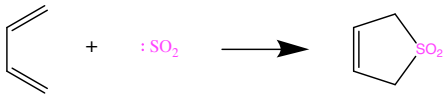

Figure 9.4: Cheletropic cycloaddition of butadiene with SO_2.

A

Appendices

A.1 Water

Molecular parameters of water: Table A.1 shows molecular parameters of water the used in the adiabatic-capture calculations.

Table A.1: Molecular parameters of water [184].

Rotational constants	A	27.88071 cm^{-1}
	B	14.52181 cm^{-1}
	C	9.27773 cm^{-1}
Reduced mass	μ	11.11533 u
Dipole moment	μ_e	1.85 D
Polarisability volume	α	1.45Å^3

Higher excited rotational states of water: The REMPI spectrum in Fig. 2.9 shows a weaker transition at 80664 cm^{-1} which could indicate the population of the higher excited rotational state $|1_{10}\rangle$ in the molecular beam. To assess a possible contribution of higher rotational states to the deflection profiles, Fig. A.1 shows simulations of a deflected beam at a rotational temperature of 30 K at which the $|1_{10}\rangle$ and $|1_{11}\rangle$ states are significantly populated. The Stark shifts and effective dipole moments of these states are shown in Figures 2.6 b and d, respectively. In particular, these states exhibit low-field seeking Stark components which manifest themselves as shoulders in the deflection profile at negative deflection coordinates. As can be seen in Figures A.1, the experimental deflection profile exhibits no such features. It can therefore be concluded that higher excited rotational states do not play a significant role in the present experiments. In particular, the measured reaction rate constants of chapter 3 predominantly reflect the contributions from the ground states of *para*- and *ortho*-water.

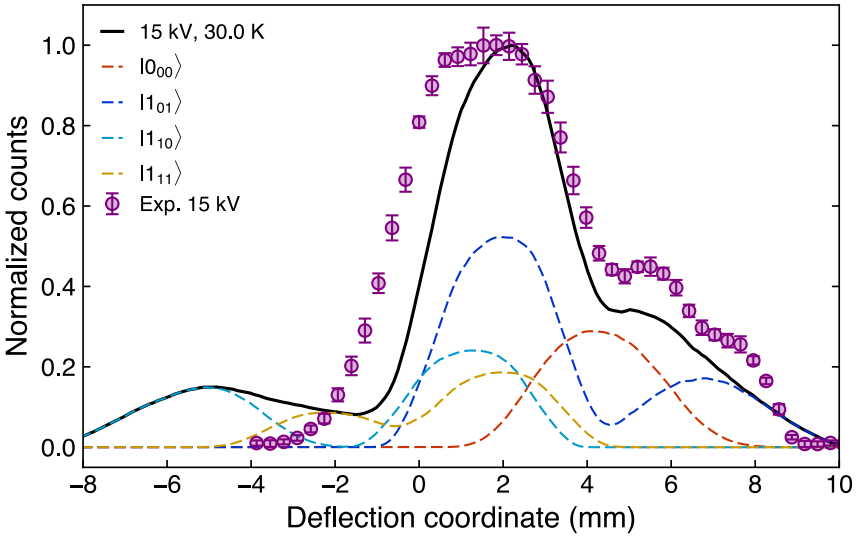

Figure A.1: Comparison of the deflection profile at 15 kV measured by fs laser ionization (purple circles) with a trajectory simulation at rotational temperature of 30 K (black solid line). At this temperature, the partly low-field seeking states 1_{10} and 1_{11} are significantly populated. The simulation predicts a shoulder appearing at negative deflection coordinates. This is not observed in the experiment indicating that these higher rotational states are not significantly populated. Error bars correspond to one standard error.

A.2 VUV ionization

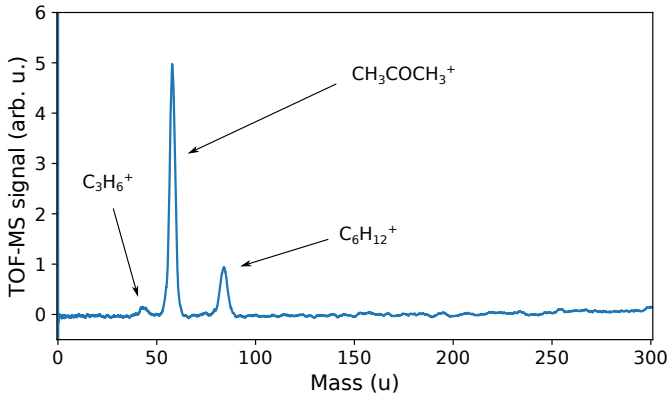

Figure A.2: **TOF-MS of Acetone and cyclohexane measured by VUV ionization.** Leaked acetone signal and residual propene and cyclohexane signal from the molecular beam.

A.3 NMR spectra of DBB

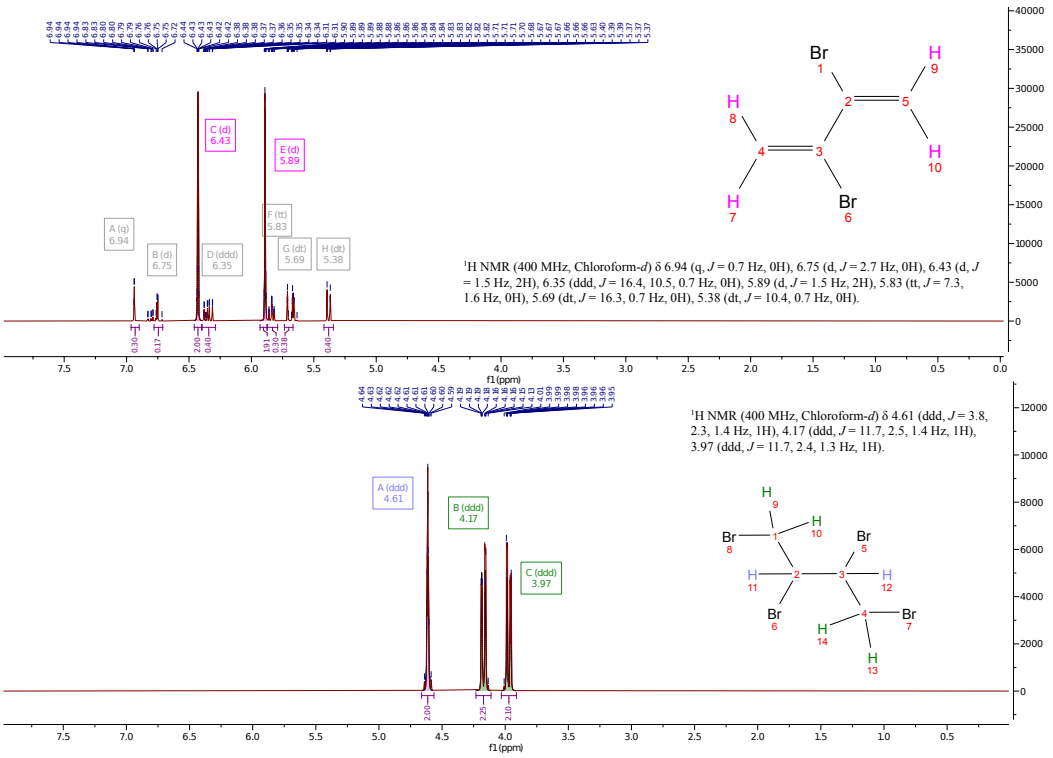

^{1}H NMR (400 MHz, Chloroform-*d*) δ 6.94 (q, *J* = 0.7 Hz, 0H), 6.75 (d, *J* = 2.7 Hz, 0H), 6.43 (d, *J* = 1.5 Hz, 2H), 6.35 (ddd, *J* = 16.4, 10.5, 0.7 Hz, 0H), 5.89 (d, *J* = 1.5 Hz, 2H), 5.83 (tt, *J* = 7.3, 1.6 Hz, 0H), 5.69 (dt, *J* = 16.3, 0.7 Hz, 0H), 5.38 (dt, *J* = 10.4, 0.7 Hz, 0H).

^{1}H NMR (400 MHz, Chloroform-*d*) δ 4.61 (ddd, *J* = 3.8, 2.3, 1.4 Hz, 1H), 4.17 (ddd, *J* = 11.7, 2.5, 1.4 Hz, 1H), 3.97 (ddd, *J* = 11.7, 2.4, 1.3 Hz, 1H).

Figure A.3: **Analysis.** ^{1}H NMR analysis of the reactant 1,2,3,4-tetrabromobutane (bottom) and the product 2,3-dibromobuta-1,3-diene (top).

Bibliography

[1] M. T. Bell, A. D. Gingell, J. Oldham, T. P. Softley, and S. Willitsch, Faraday Discuss. **142**, 73 (2009).

[2] M. Schnell and G. Meijer, Angew. Chem. Int. Ed. **48**, 6010 (2009).

[3] J. Meyer and R. Wester, *Ion–molecule reaction dynamics*, Annu. Rev. Phys. Chem. **68**, 333 (2017).

[4] J. Toscano, H. J. Lewandowski, and B. R. Heazlewood, *Cold and controlled chemical reaction dynamics*, Phys. Chem. Chem. Phys. **22**, 9180 (2020).

[5] S. Y. T. van de Meerakker, H. L. Bethlem, and G. Meijer, Nat. Phys. **4**, 595 (2008).

[6] Y.-P. Chang, D. A. Horke, S. Trippel, and J. Küpper, *Spatially-controlled complex molecules and their applications*, Int. Rev. Phys. Chem. **34**, 557 (2015).

[7] E. Carrascosa, J. Meyer, and R. Wester, *Imaging the dynamics of ion-molecule reactions*, Chem. Soc. Rev **46**, 7498 (2017).

[8] B. Heazlewood and T. P. Softley, *Low-temperature kinetics and dynamics with coulomb crystals*, Annu. Rev. Phys. Chem. **66**, 475 (2015).

[9] S. Willitsch, *Chemistry with controlled ions*, Adv. Chem. Phys. **162**, 307 (2017).

[10] F. Filsinger, J. Küpper, G. Meijer, J. L. Hansen, J. Maurer, J. H. Nielsen, L. Holmegaard, and H. Stapelfeldt, *Pure samples of individual conformers: the separation of stereo-isomers of complex molecules using electric fields*, Angew. Chem. Int. Ed. **48**, 6900 (2009).

[11] S. Y. T. van de Meerakker, H. L. Bethlem, N. Vanhaecke, and G. Meijer, Chem. Rev. **112**, 4828 (2012).

[12] F. Filsinger, U. Erlekam, G. von Helden, J. Küpper, and G. Meijer, Phys. Rev. Lett. **100**, 133003 (2008).

[13] Y.-P. Chang, K. Dlugolecki, J. Küpper, D. Rösch, D. Wild, and S. Willitsch, *Specific chemical reactivities of spatially separated 3-aminophenol conformers with cold Ca^+ ions*, Science **342**, 98 (2013).

[14] T. Kierspel, D. A. Horke, Y.-P. Chang, and J. Küpper, *Spatially separated polar samples of the* cis *and* trans *conformers of 3-fluorophenol*, Chem. Phys. Let. **591**, 130 (2014).

[15] D. A. Horke, Y.-P. Chang, K. Długołęcki, and J. Küpper, *Separating para and ortho water*, Angew. Chem. Int. Ed. **53**, 11965 (2014).

[16] M. Drewsen, I. Jensen, J. Lindballe, N. Nissen, R. Martinussen, A. Mortensen, P. Staanum, and D. Voigt, Int. J. Mass Spectrom. **229**, 83 (2003).

[17] S. Willitsch, *Coulomb-crystallised molecular ions in traps: methods, applications, prospects*, Int. Rev. Phys. Chem. **31**, 175 (2012).

[18] P. R. Bunker and P. Jensen, *Molecular Symmetry and Spectroscopy, 2nd ed.* (NRC Research Press, Ottawa, 1998).

[19] H. Kanamori, Z. T. Dehghani, A. Mizoguchi, and Y. Endo, Phys. Rev. Lett. **119**, 173401 (2017).

[20] M. Quack, *Detailed symmetry selection rules for reactive collisions*, **34**, 477 (1977).

[21] A. Kilaj, H. Gao, D. Rösch, U. Rivero, J. Küpper, and S. Willitsch, *Observation of different reactivities of para and ortho-water towards trapped diazenylium ions*, Nat. Commun. **9**, 2096 (2018).

[22] E. M. Carreira, K. A. Woerpel, O. Reiser, and L. Kvaerno, *Classics in Stereoselective Synthesis* (Wiley VCH Verlag GmbH, 2008).

[23] N. E. S. K. Peter C. Vollhardt, *Organische Chemie* (Wiley VCH Verlag GmbH, 2011).

[24] O. Diels and K. Alder, *Synthesen in der hydroaromatischen Reihe*, Justus Liebigs Ann. Chem. **460**, 98 (1928).

[25] J. Sauer and R. Sustmann, *Mechanistic aspects of diels-alder reactions: A critical survey*, Angew. Chem. Int. Ed. Engl. **19**, 779 (1980).

[26] K. N. Houk, J. González, and Y. Li, *Pericyclic reaction transition states: Passions and punctilios, 1935-1995*, Acc. Chem. Res. **28**, 81 (1995).

[27] R. B. Woodward and R. Hoffmann, *The conservation of orbital symmetry*, Angewandte Chemie International Edition in English **8**, 781 (1969).

[28] L. R. Domingo and J. A. Sáez, *Understanding the mechanism of polar diels-alder reactions*, Org. Biomol. Chem. **7**, 3576 (2009).

[29] R. R. Schmidt, *Polar cycloadditions*, Angew. Chem. Int. Ed. Engl. **12**, 212 (1973).

[30] U. Haberl, O. Wiest, and E. Steckhan, *Ab initio studies of the radical cation diels-alder reaction*, J. Am. Chem. Soc. **121**, 6730 (1999).

[31] M. N. Eberlin, *Gas-phase polar cycloadditions*, Int. J. Mass Spectrom. **235**, 263 (2004).

[32] P. J. Donoghue and O. Wiest, *Structure and reactivity of radical ions: New twists on old concepts*, Chem. Eur. J. **12**, 7018 (2006).

[33] A. Kilaj, H. Gao, D. Tahchieva, R. Ramakrishnan, D. Bachmann, D. Gillingham, O. A. von Lilienfeld, J. Küpper, and S. Willitsch, *Quantum-chemistry-aided identification, synthesis and experimental validation of model systems for conformationally controlled reaction studies: Separation of the conformers of 2,3-dibromobuta-1,3-diene in the gas phase*, Phys. Chem. Chem. Phys. **22**, 13431 (2020).

[34] R. E. March and J. F. Todd, *Quadrupole Ion Trap Mass Spectrometry* (John Wiley & Sons, Hoboken, 2005), 2nd ed.

[35] D. Leibfried, R. Blatt, C. Monroe, and D. Wineland, Rev. Mod. Phys. **75**, 281 (2003).

[36] R. Blatt and D. Wineland, Nature **453**, 1008 (2008).

[37] C. Monroe, D. M. Meekhof, B. E. King, S. R. Jefferts, W. M. Itano, D. J. Wineland, and P. Gould, Phys. Rev. Lett. **75**, 4011 (1995).

[38] H. J. Metcalf and P. van der Straten, *Laser Cooling and Trapping* (Springer, New York, 1999).

[39] C. J. Pethick and H. Smith, *Bose-Einstein Condensation in Dilute Gases* (Cambridge University Press, 2001).

[40] J. Eschner, G. Morigi, F. Schmidt-Kaler, and R. Blatt, J. Opt. Soc. Am. B **20**, 1003 (2003).

[41] F. Schmidt-Kaler, H. Häffner, S. Gulde, M. Riebe, G. P. T. Lancaster, T. Deuschle, C. Becher, W. Hänsel, J. Eschner, C. F. Roos, et al., Appl. Phys. B **77**, 789 (2003).

[42] E. L. Pollock and J. P. Hansen, Phys. Rev. A **8**, 3110 (1973).

[43] R. T. Farouki and S. Hamaguchi, Phys. Rev. E **47**, 4330 (1993).

[44] J. P. Schiffer, Phys. Rev. Lett. **88**, 205003 (2002).

[45] B. Roth and S. Schiller, in *Cold Molecules*, edited by R. V. Krems, W. C. Stwalley, and B. Friedrich (CRC Press, Boca Raton, 2009), p. 651.

[46] F. Filsinger, J. Küpper, G. Meijer, L. Holmegaard, J. H. Nielsen, I. Nevo, J. L. Hansen, and H. Stapelfeldt, *Quantum-state selection, alignment, and orientation of large molecules using static electric and laser fields*, J. Chem. Phys **131**, 064309 (2009).

[47] W. Demtröder, *Laser Spectroscopy 2* (Springer Berlin Heidelberg, 2015).

[48] T. E. Wall, *Preparation of cold molecules for high-precision measurements*, J. Phys. B: At., Mol. Opt. Phys. **49**, 243001 (2016).

[49] Y.-P. Chang, F. Filsinger, B. G. Sartakov, and J. Küpper, *Cmistark: Python package for the stark-effect calculation and symmetry classification of linear, symmetric and asymmetric top wavefunctions in dc electric fields*, Comp. Phys. Comm. **185**, 339 (2014).

[50] C. M. Western, *PGOPHER: A program for simulating rotational, vibrational and electronic spectra*, J. Quant. Spectrosc. Radiat. Transfer **186**, 221 (2017).

[51] D. McQuarrie, *Physical chemistry : a molecular approach* (University Science Books, Sausalito, Calif, 1997).

[52] D. Clary, Annu. Rev. Phys. Chem. **41**, 61 (1990).

[53] D. Smith, Chem. Rev. **92**, 1473 (1992).

[54] D. Smith and P. Spanel, *Ions in the terrestrial atmosphere and in interstellar clouds*, Mass. Spectrom. Rev. **14**, 255 (1995).

[55] M. Larsson, W. D. Geppert, and G. Nyman, *Ion chemistry in space*, Rep. Prog. Phys **75**, 066901 (2012).

[56] D. Clary, *Rate constants for the reactions of ions with dipolar polyatomic molecules*, J. Chem. Soc., Faraday Trans. 2 **83**, 139 (1987).

[57] J. Troe, J. Chem. Phys. **87**, 2773 (1987).

[58] T. Stoecklin, D. C. Clary, and A. Palma, *Rate constant calculations for ion-symmetric top and ion-asymmetric top reactions*, J. Chem. Soc. Faraday Trans. **88**, 901 (1992).

[59] J. Sansonetti, *Handbook of basic atomic spectroscopic data, nist standard reference database 108* (2003).

[60] D. Rösch, Ph.D. thesis, University of Basel (2016).

[61] D. Rösch, H. Gao, A. Kilaj, and S. Willitsch, *Design and characterization of a linear quadrupole ion trap for high-resolution coulomb-crystal time-of-flight mass spectrometry*, EPJ Tech. Instrum. **3**, 5 (2016).

[62] P. Puri, M. Mills, C. Schneider, I. Simbotin, J. A. Montgomery, R. Côté, A. G. Suits, and E. R. Hudson, *Synthesis of mixed hypermetallic oxide baoca+ from laser-cooled reagents in an atom-ion hybrid trap*, Science **357**, 1370 (2017).

[63] J. Greenberg, P. C. Schmid, M. Miller, J. F. Stanton, and H. J. Lewandowski, *Quantum-state-controlled reactions between molecular radicals and ions*, Phys. Rev. A **98**, 032702 (2018).

[64] P. C. Schmid, M. I. Miller, J. Greenberg, T. L. Nguyen, J. F. Stanton, and H. J. Lewandowski, *Quantum-state-specific reaction rate measurements for the photo-induced reaction* $ca^+ + o_2$ *to* $cao^+ + o$, Mol. Phys. **117**, 3036 (2019).

[65] L. S. Petralia, A. Tsikritea, J. Loreau, T. P. Softley, and B. R. Heazlewood, *Strong inverse kinetic isotope effect observed in ammonia charge exchange reactions*, Nat. Commun. **11** (2020).

[66] D. Irimia, D. Dobrikov, R. Kortekaas, H. Voet, D. A. van den Ende, W. A. Groen, and M. H. M. Janssen, *A short pulse (7 µs fwhm) and high repetition rate (dc–5khz) cantilever piezovalve for pulsed atomic and molecular beams*, Rev. Sci. Instrum. **80**, 113303 (2009).

[67] S. M. Hankin, D. M. Villeneuve, P. B. Corkum, and D. M. Rayner, *Intense-field laser ionization rates in atoms and molecules*, Phys. Rev. A **64**, 013405 (2001).

[68] A. D. Gingell, M. T. Bell, J. M. Oldham, T. P. Softley, and J. M. Harvey, J. Chem. Phys. **133**, 194302 (2010).

[69] F. G. Major, V. N. Gheorghe, and G. Werth, *Charged Particle Traps* (Springer, Berlin and Heidelberg, 2005).

[70] D. Manura and D. Dahl, *SIMION 8.0/8.1 User manual*, Scientific Instrument Services, Inc., Ringoes, NJ, rev. 5 ed. (2011).

[71] P. C. Schmid, J. Greenberg, M. I. Miller, K. Loeffler, and H. J. Lewandowski, *An ion trap time-of-flight mass spectrometer with high mass resolution for cold trapped ion experiments*, Rev. Sci. Instrum **88**, 123107 (2017).

[72] D. Rösch, S. Willitsch, Y.-P. Chang, and J. Küpper, *Chemical reactions of conformationally selected 3-aminophenol molecules in a beam with coulomb-crystallized Ca^+ ions*, J. Chem. Phys. **140**, 124202 (2014).

[73] *COMSOL Multiphysics version 3.5a and 4.3a, www.comsol.com.*

[74] C.-H. Yang, G. Sarma, J. J. ter Meulen, D. H. Parker, and C. M. Western, Phys. Chem. Chem. Phys. **12**, 13983 (2010).

[75] C. M. Western, J. Quant. Spectrosc. Radiat. Transf. **186**, 221 (2016).

[76] D. Betowski, J. D. Pazyant, G. I. Mackay, and D. K. Bohme, Chem. Phys. Lett. **31**, 321 (1975).

[77] J. Wiese, J.-F. Olivieri, A. Trabattoni, S. Trippel, and J. Küpper, *Strong-field photoelectron momentum imaging of OCS at finely resolved incident intensities*, New J. Phys **21**, 083011 (2019).

[78] Z.-D. Sun, K. Takagi, and F. Matsushima, Science **310**, 1938 (2005).

[79] Z.-D. Sun, M. Ge, and Y. Zheng, Nat. Commun. **6**, 6877 (2015).

[80] V. I. Tikhonov and A. A. Volkov, Science **296**, 2363 (2002).

[81] C. Manca Tanner, M. Quack, and D. Schmidiger, J. Phys. Chem. A **117**, 10105 (2013).

[82] R. Georges, X. Michaut, A. Moudens, M. Goubet, O. Pirali, P. Soulard, P. Asselin, T. Huet, P. Roy, M. Fournier, et al., J. Phys. Chem. A **121**, 7455 (2017).

[83] R. D. Guettler, G. C. Jones Jr., L. A. Posey, and R. N. Zare, Science **266**, 259 (1994).

[84] F. F. Crim, *Chemical dynamics of vibrationally excited molecules: Controlling reactions in gases and on surfaces*, Proc. Natl. Acad. Sci. **105**, 12647 (2008).

[85] K. Liu, Ann. Rev. Phys. Chem. **67**, 91 (2016).

[86] I. W. M. Smith, *Reactions at very low temperatures: gas kinetics at a new frontier*, Angew. Chem. Int. Ed. **45**, 2842 (2006).

[87] D. Hauser, S. Lee, F. Carelli, S. Spieler, O. Lakhmanskaya, E. S. Endres, S. S. Kumar, F. Gianturco, and R. Wester, *Rotational state-changing cold collisions of hydroxyl ions with helium*, Nat. Phys. **11**, 467 (2015).

[88] Y. Shagam, A. Klein, W. Skomorowski, R. Yun, V. Averbukh, C. P. Koch, and E. Narevicius, *Molecular hydrogen interacts more strongly when rotationally excited at low temperatures leading to faster reactions*, Nat. Chem. **7**, 921 (2015).

[89] W. Perreault, N. Mukherjee, and R. N. Zare, Science **358**, 356 (2017).

[90] D. Gerlich, R. Plašil, I. Zymak, M. Hejduk, P. Jusko, D. Mulin, and J. Glosík, J. Chem. Phys. A **117**, 10068 (2013).

[91] T. Kravchuk, M. Reznikov, P. Tichonov, N. Avidor, Y. Meir, A. Bekkerman, and G. Alexandrowicz, Science **331**, 319 (2011).

[92] B. E. Turner, Astrophys. J. **193**, L83 (1974).

[93] P. Caselli, P. J. Benson, P. C. Myers, and M. Tafalla, Astrophys. J. **572**, 238 (2002).

[94] E. A. Bergin, J. Alves, T. Huard, and C. J. Lada, Astrophys. J. Lett. **570**, L101 (2002).

[95] N. Teschmit, K. Dlugolecki, D. Gusa, I. Rubinsky, D. A. Horke, and J. Küpper, *Characterizing and optimizing a laser-desorption molecular beam source*, J. Chem. Phys. **147**, 144204 (2017).

[96] U. Rivero, Ph.D. thesis, University of Basel (2020).

[97] M. J. Frisch, G. W. Trucks, H. B. Schlegel, G. E. Scuseria, M. A. Robb, J. R. Cheeseman, G. Scalmani, V. Barone, B. Mennucci, G. A. Petersson, et al., *Gaussian 09 Revision E.01*, Gaussian Inc., Wallingford CT, 2009.

[98] S. Ospelkaus, K.-K. Ni, D. Wang, M. H. G. de Miranda, B. Neyenhuis, G. Quéméner, P. S. Julienne, J. L. Bohn, D. S. Jin, and J. Ye, Science **327**, 853 (2010).

[99] D. J. Butcher, *Vacuum Ultraviolet Radiation for Single-Photoionization Mass Spectrometry: A Review*, Microchem. J. **62**, 354 (1999).

[100] R. H. Lipson, S. S. Dimov, P. Wang, Y. J. Shi, D. M. Mao, X. K. Hu, and J. Vanstone, *Vacuum ultraviolet and extreme ultraviolet lasers: Principles, instrumentation, and applications*, Instrumentation Science & Technology **28**, 85 (2000).

[101] L. Hanley and R. Zimmermann, *Light and Molecular Ions: The Emergence of Vacuum UV Single-Photon Ionization in MS*, Anal. Chem. **81**, 4174 (2009).

[102] S. Willitsch and F. Merkt, Int. J. Mass Spectrom. **245**, 14 (2005).

[103] M. N. R. Ashfold and J. D. Howe, Annu. Rev. Phys. Chem. **45**, 57 (1994).

[104] S. E. Van Bramer and M. V. Johnston, *10.5-ev photoionization mass spectrometry of aliphatic compounds*, J. Am. Soc. Mass. Spectrom. **1**, 419 (1990).

[105] R. Steenvoorden, P. Kistemaker, A. D. Vries, L. Michalak, and N. Nibbering, *Laser single photon ionization mass spectrometry of linear, branched and cyclic hexanes*, Int. J. Mass Spectrom. **107**, 475 (1991).

[106] N. P. Lockyer and J. C. Vickerman, *Single photon ionisation mass spectrometry using laser-generated vacuum ultraviolet photons*, Laser Chem. **17**, 139 (1997).

[107] M. J. S. Dewar and S. D. Worley, *Photoelectron spectra of molecules. i. ionization potentials of some organic molecules and their interpretation*, J. Chem. Phys. **50**, 654 (1969).

[108] C. R. Vidal, in *Tunable Lasers*, edited by L. F. Mollenauer and J. C. White (Springer, Berlin, Heidelberg, 1987), vol. 59, chap. 3, p. 57.

[109] J. F. Ward and G. H. C. New, Phys. Rev. **185**, 57 (1969).

[110] R. Mahon, T. McIlrath, V. Myerscough, and D. Koopman, *Third-harmonic generation in argon, krypton, and xenon: Bandwidth limitations in the vicinity of lyman-α*, IEEE J. Quantum Electron. **15**, 444 (1979).

[111] G. C. Bjorklund, *Effects of focusing on third-order nonlinear processes in isotropic media*, IEEE J. Quantum Electr. **11**, 287 (1975).

[112] A. Kung, J. Young, and S. Harris, *Generation of 1182-Å radiation in phase–matched mixtures of inert gases*, Appl. Phys. Lett. **22**, 301 (1973).

[113] Y. J. Shi, S. Consta, A. K. Das, B. Mallik, D. Lacey, and R. H. Lipson, *A 118 nm vacuum ultraviolet laser/time-of-flight mass spectroscopic study of methanol and ethanol clusters in the vapor phase*, J. Chem. Phys **116**, 6990 (2002).

[114] J. M. Gray, J. A. Bossert, Y. Shyur, and H. J. Lewandowski, *Measurements of trap dynamics of cold oh molecules using resonance-enhanced multiphoton ionization*, Phys. Rev. A **96**, 023416 (2017).

[115] H. C. Hsu and C.-K. Ni, *Vacuum ultraviolet single-photon postionization of amino acids*, Applied Sciences **8**, 699 (2018).

[116] W. Hunter, in *Vacuum Ultraviolet Spectroscopy I*, edited by J. Samson and D. Ederer (Academic Press, 1998), vol. 31 of *Experimental Methods in the Physical Sciences*, pp. 305–346.

[117] P. Laporte, J. L. Subtil, M. Courbon, M. Bon, and L. Vincent, *Vacuum-ultraviolet refractive index of lif and mgf2 in the temperature range 80–300 k*, J. Opt. Soc. Am. **73**, 1062 (1983).

[118] R. B. Cairns and J. A. R. Samson, *Metal photocathodes as secondary standards for absolute intensity measurements in the vacuum ultraviolet∗*, J. Opt. Soc. Am. **56**, 1568 (1966).

[119] G. W. Faris and M. J. Dyer, *Two-photon excitation of neon at 133 nm*, Opt. Lett. **18**, 382 (1993).

[120] G. W. Faris, S. A. Meyer, M. J. Dyer, and M. J. Banks, *Two-photon-resonant difference-frequency mixing with an arf excimer laser: vacuum-ultraviolet generation and multiphoton spectroscopy*, J. Opt. Soc. Am. B **17**, 1856 (2000).

[121] S. Willitsch, Ph.D. thesis, Eidgenössische Technische Hochschule, Zürich (2004), dISS ETH Nr. 15713.

[122] S. E. V. Bramer and M. V. Johnston, *Tunable, coherent vacuum ultraviolet radiation for photoionization mass spectrometry*, Appl. Spectrosc. **46**, 255 (1992).

[123] J. M. Serafimov, D. Gillingham, S. Kuster, and D. Hilvert, *The putative diels-alderase macrophomate synthase is an efficient aldolase*, J. Am. Chem. Soc **130**, 7798 (2008).

[124] L. R. Domingo, J. Chil. Chem. Soc. **2615**, 59 (2014).

[125] M. A. F. de Souza, E. Ventura, S. A. do Monte, J. M. Riveros, and R. L. Longo, J. Comput. Chem. **37**, 701 (2016).

[126] U. Rivero, O. T. Unke, M. Meuwly, and S. Willitsch, *Reactive atomistic simulations of diels-alder reactions: The importance of molecular rotations*, J. Chem. Phys. **151**, 104301 (2019).

[127] D. A. Singleton and A. A. Thomas, *High-precision simultaneous determination of multiple small kinetic isotope effects at natural abundance*, J. Am. Chem. Soc **117**, 9357 (1995).

[128] U. Rivero, M. Meuwly, and S. Willitsch, *A computational study of the diels-alder reactions between 2, 3-dibromo-1, 3-butadiene and maleic anhydride*, Chem. Phys. Let. **683**, 598 (2017).

[129] T. Sperger, I. A. Sanhueza, and F. Schoenebeck, *Computation and experiment: A powerful combination to understand and predict reactivities*, Acc. Chem. Res **49**, 1311 (2016).

[130] W. Notz, F. Tanaka, S.-i. Watanabe, N. S. Chowdari, J. M. Turner, R. Thayumanavan, and C. F. Barbas, *The direct organocatalytic asymmetric mannich reaction: unmodified aldehydes as nucleophiles*, J. Org. Chem. **68**, 9624 (2003).

[131] S. Er, C. Suh, M. P. Marshak, and A. Aspuru-Guzik, *Computational design of molecules for an all-quinone redox flow battery*, Chem. Sci. **6**, 885 (2015).

[132] A. C. Doney, B. J. Rooks, T. Lu, and S. E. Wheeler, *Design of organocatalysts for asymmetric propargylations through computational screening*, ACS Catal. **6**, 7948 (2016).

[133] O. A. von Lilienfeld, Int. J. Quantum Chem. **113**, 1676 (2013).

[134] M. J. S. Dewar, S. Olivella, and J. J. P. Stewart, *Mechanism of the diels-alder reaction: reactions of butadiene with ethylene and cyanoethylenes*, J. Am. Chem. Soc. **108**, 5771 (1986).

[135] O. A. von Lilienfeld, *Towards the Computational Design of Compounds from First Principles*, vol. IX of *Mathematical Physics Studies* (Springer, 2014).

[136] S. Kozuch and J. M. L. Martin, *Dsd-pbep86: In search of the best double-hybrid dft with spin-component scaled mp2 and dispersion corrections*, Phys. Chem. Chem. Phys. **13**, 20104 (2011).

[137] F. Weigend and R. Ahlrichs, *Balanced basis sets of split valence, triple zeta valence and quadruple zeta valence quality for h to rn: design and assessment of accuracy*, Phys. Chem. Chem. Phys. **7**, 3297 (2005).

[138] D. N. Tahchieva, D. Bakowies, R. Ramakrishnan, and O. A. von Lilienfeld, *Torsional potentials of glyoxal, oxalyl halides, and their thiocarbonyl derivatives: Challenges for popular density functional approximations*, J. Chem. Theor. Comput. **14**, 4806 (2018).

[139] C. A. Stewart Jr., B. Hundred Del., and assignor to E. I. du Pont de Nemours and Co, *Preparation of 2, 3-dichlorobutadiene-1,3* (1962), uS patent no. 3061653A.

[140] H.-J. Werner, G. Knizia, and F. R. Manby, *Explicitly correlated coupled cluster methods with pair-specific geminals*, Mol. Phys. **109**, 407 (2011).

[141] K. A. Peterson, T. B. Adler, and H.-J. Werner, *Systematically convergent basis sets for explicitly correlated wavefunctions: The atoms h, he, b-ne, and al-ar*, J. Chem. Phys. **128**, 084102 (2008).

[142] W. Győrffy, G. Knizia, and H.-J. Werner, *Analytical energy gradients for explicitly correlated wave functions. i. explicitly correlated second-order møller-plesset perturbation theory*, J. Comp. Phys. **147**, 214101 (2017).

[143] W. Győrffy and H.-J. Werner, *Analytical energy gradients for explicitly correlated wave functions. ii. explicitly correlated coupled cluster singles and doubles with perturbative triples corrections: Ccsd (t)-f12*, J. Comp. Phys. **148**, 114104 (2018).

[144] S. Trippel, M. Johny, T. Kierspel, J. Onvlee, H. Bieker, H. Ye, T. Mullins, L. Gumprecht, K. Długołęcki, and J. Küpper, *Knife edge skimming for improved separation of molecular species by the deflector*, Rev. Sci. Instrum. **89**, 096110 (2018).

[145] S. Zigo, A.-T. Le, P. Timilsina, and C. A. Trallero-Herrero, *Ionization study of isomeric molecules in strong-field laser pulses*, Sci. Rep. **7**, 42149 EP (2017).

[146] P. Ehrenfreund and M. A. Sephton, *Carbon molecules in space: from astrochemistry to astrobiology*, Faraday Discuss. **133**, 277 (2006).

[147] V. G. Kunde, A. C. Aikin, R. A. Hanel, D. E. Jennings, W. C. Maguire, and R. E. Samuelson, *C_4H_2, HC_3N and C_2N_2 in Titan's atmosphere*, Nature **292**, 686 (1981).

[148] V. Vuitton, R. Yelle, and M. McEwan, *Ion chemistry and n-containing molecules in titan's upper atmosphere*, Icarus **191**, 722 (2007).

[149] F. Postberg, N. Khawaja, B. Abel, G. Choblet, C. R. Glein, M. S. Gudipati, B. L. Henderson, H.-W. Hsu, S. Kempf, F. Klenner, et al., *Macromolecular organic compounds from the depths of enceladus*, Nature **558**, 564 (2018).

[150] D. K. Böhme and H. Schwarz, *Gas-phase catalysis by atomic and cluster metal ions: The ultimate single-site catalysts*, Angew. Chem. Int. Ed. **44**, 2336 (2005).

[151] J. Roithová and D. Schröder, *Selective activation of alkanes by gas-phase metal ions*, Chem. Rev. **110**, 1170 (2010).

[152] G. Gioumousis and D. P. Stevenson, J. Chem. Phys. **29**, 294 (1958).

[153] K. Mølhave and M. Drewsen, *Formation of translationally cold* mgh^+ *and* mgd^+ *molecules in an ion trap*, Phys. Rev. A **62**, 011401 (2000).

[154] P. F. Staanum, K. Højbjerre, R. Wester, and M. Drewsen, Phys. Rev. Lett. **100**, 243003 (2008).

[155] F. H. J. Hall, M. Aymar, N. Bouloufa-Maafa, O. Dulieu, and S. Willitsch, *Light-assisted ion-neutral reactive processes in the cold regime: Radiative molecule formation versus charge exchange*, Phys. Rev. Lett. **107** (2011).

[156] W. Fang, L. Gong, Q. Zhang, X. Shan, F. Liu, Z. Wang, and L. Sheng, *Dissociative photoionization of 1,3-butadiene: Experimental and theoretical insights*, The Journal of Chemical Physics **134**, 174306 (2011).

[157] F. H. J. Hall, M. Aymar, M. Raoult, O. Dulieu, and S. Willitsch, Mol. Phys. **111**, 1683 (2013).

[158] F. H. J. Hall, P. Eberle, G. Hegi, M. Raoult, M. Aymar, O. Dulieu, and S. Willitsch, Mol. Phys. **111**, 2020 (2013).

[159] L. R. Churchill, M. V. DePalatis, and M. S. Chapman, *Charge exchange and chemical reactions with trapped Th^{3+}*, Phys. Rev. A **83** (2011).

[160] A. D. Dörfler, P. Eberle, D. Koner, M. Tomza, M. Meuwly, and S. Willitsch, *Long-range versus short-range effects in cold molecular ion-neutral collisions*, Nat. Commun. **10** (2019).

[161] A. Kramida and Y. Ralchenko, *Nist atomic spectra database, nist standard reference database 78* (1999).

[162] R. B. Woodward, F. Sondheimer, D. Taub, K. Heusler, and W. M. McLamore, *The total synthesis of steroids*, J. Am. Chem. Soc. **74**, 4223 (1952).

[163] P. A. Wender, J. M. Schaus, and A. W. White, *General methodology for cis-hydroisoquinoline synthesis: synthesis of reserpine*, J. Am. Chem. Soc. **102**, 6157 (1980).

[164] M. G. Charest, D. R. Siegel, and A. G. Myers, *Synthesis of (-)-tetracycline*, J. Am. Chem. Soc. **127**, 8292 (2005).

[165] R. Hanel, B. Conrath, F. M. Flasar, V. Kunde, W. Maguire, J. Pearl, J. Pirraglia, R. Samuelson, L. Herath, M. Allison, et al., *Infrared observations of the saturnian system from voyager 1*, Science **212**, 192 (1981).

[166] C. A. Nixon, D. E. Jennings, B. Bézard, S. Vinatier, N. A. Teanby, K. Sung, T. M. Ansty, P. G. J. Irwin, N. Gorius, V. Cottini, et al., *Detection of propene in titan's stratosphere*, Astrophys. J.l **776**, L14 (2013).

[167] C. A. Arrington, C. Ramos, A. D. Robinson, and T. S. Zwier, *Aromatic ring-forming reactions of metastable diacetylene with 1,3-butadiene*, J. Phys. Chem. A **102**, 3315 (1998).

[168] D. J. Goebbert, X. Liu, and P. G. Wenthold, *Reactions of diacetylene radical cation with ethylene*, J. Am. Soc. Mass Spectrom. **15**, 114 (2004), pMID: 14698561.

[169] A. Colorado, D. J. Barket, J. M. Hurst, and P. B. Shepson, *A fast-response method for determination of atmospheric isoprene using quadrupole ion trap mass spectrometry*, Anal. Chem. **70**, 5129 (1998).

[170] M. Hofmann and H. F. Schaefer, *Pathways for the reaction of the butadiene radical cation $c_4h_6^+$, with ethylene*, J. Phys. Chem. A **103**, 8895 (1999).

[171] G. Bouchoux, J.-Y. Salpin, and F. Turecek, *Cycloaddition reactions between 1,3-butadiene radical cations and ethene in the gas phase*, Rapid Commun. Mass Spectrom **8**, 325 (1994).

[172] D. Kuck, J. Schneider, and H.-F. Grützmacher, *A study of gaseous benzenium and toluenium ions generated from 1,4- dihydro- and 1-methyl-1,4-dihydro-benzoic acids*, J. Chem. Soc., Perkin Trans. 2 pp. 689–696 (1985).

[173] D. Schröder, H. Schwarz, P. Milko, and J. Roithová, *Dissociation routes of protonated toluene probed by infrared spectroscopy in the gas phase†*, J. Phys. Chem. A **110**, 8346 (2006).

[174] Z.-C. Wang, D. L. Thomsen, E. L. Motell, M. S. Robinson, R. Garrey, V. M. Bierbaum, and C. H. DePuy, *The gas-phase methylation of benzene and toluene*, Int. J. Mass Spectrom. **429**, 6 (2018).

[175] C. Lifshitz, *Tropylium ion formation from toluene: Solution of an old problem in organic mass spectrometry*, Acc. Chem. Res. **27**, 138 (1994).

[176] A. S. Siegel, *Rearrangement ions. III. tropylium ion in the mass spectrum of toluene-2,6-13c2*, J. Am. Chem. Soc. **92**, 5277 (1970).

[177] P. N. Rylander, S. Meyerson, and H. M. Grubb, *Organic ions in the gas phase. II. the tropylium ion*, J. Am. Chem. Soc. **79**, 842 (1957).

[178] X. Tong, A. H. Winney, and S. Willitsch, *Sympathetic cooling of state-selected molecular ions*, Phys. Rev. Lett. **105**, 143001 (2010).

[179] X. Tong, T. Nagy, J. Yosa Reyes, M. Germann, M. Meuwly, and S. Willitsch, *State-selected ion-molecule reactions with Coulomb-crystallized molecular ions in traps*, Chem. Phys. Lett. **547**, 1 (2012).

[180] O. Zakharenko, R. A. Motiyenko, J. R. A. Moreno, and T. R. Huet, *Conformational landscape and torsion–rotation–vibration effects in the two conformers of methyl vinyl ketone, a major oxidation product of isoprene*, J. Phys. Chem. A **121**, 6420 (2017).

[181] T. Gierczak, J. B. Burkholder, R. K. Talukdar, A. Mellouki, S. Barone, and A. Ravishankara, *Atmospheric fate of methyl vinyl ketone and methacrolein*, J. Photochem. Photobiol., A **110**, 1 (1997).

[182] V. P. Barber, S. Pandit, A. M. Green, N. Trongsiriwat, P. J. Walsh, S. J. Klippenstein, and M. I. Lester, *Four-carbon criegee intermediate from isoprene ozonolysis: Methyl vinyl ketone oxide synthesis, infrared spectrum, and OH production*, J. Am. Chem. Soc. **140**, 10866 (2018).

[183] I. A. Elayan, M. H. Almatarneh, and J. W. Hollett, *The bimolecular catalytic transformation of methyl vinyl ketone oxide: A DFT study*, Chem. Phys. **530**, 110649 (2020).

[184] F. DeLucia, P. Helminger, and W. Kirchhoff, J. Phys. Chem. Ref. Data **3**, 211 (1974).

Acknowledgements

This work would not have been possible without the support and guidance of many great people that I had the chance to meet in my journey of becoming a scientist. Therefore, I would like to use this opportunity to kindly thank everybody who supported me in this journey.
First of all, I would like to thank Prof. Dr. Stefan Willitsch for putting his trust in my abilities and giving me the opportunity to be part of his research group. His constant support and guidance provided a stimulating environment for research.
I would like to thank Prof. Dr. Roland Wester for being the second referee and taking the time to review my thesis.
I am also grateful to Prof. Dr. Jochen Küpper for his support and many interesting discussions.
I want to thank Dr. Daniel Rösch for passing on this exciting experiment to me and teaching me the basics of the apparatus.
I acknowledge Dr. Hong Gao for his support with the measurements in chapter 3 and for designing the first version of the VUV cell. I would like to thank Dr. Jia Wang for support with the measurements in chapters 8 and 6. Many thanks to Mr. Lei Xu for support during the measurements in chapter 6 and for simulating TOF traces using SIMION. I want thank Dr. Uxia Rivero for providing the ab-initio calculations in the chapters 3 and 6, Dr. Diana Tahchieva for the theoretical screening in chapter 5 and Patrik Stranak for providing quantum chemical calculations for the measurements in chapter 8.
I would like to thank Dr. Anatoly Johnson for sharing his broad knowledge about lasers and Georg Holderied for always lending a helping hand with electronics. I also would like to thank the whole Willitsch group for interesting discussions and some great memories. I am grateful to Gregor Hegi for always finding time to support me with experimental difficulties. My office family Uxia Rivero, Patrik Stranak and Ludgar Ploenes made this time a pleasant journey.
I am very grateful to my family for their patience and understanding and constant mental support. I am especially thankful to my life companion Thomas Karg for his enduring patience, for always believing in me and for proof-reading my thesis. Mostly, I want to thank him for his never ending support and for always being there no matter what.